Interface-Mediated Mechanical Properties of Materials
-
Atomistic Simulation Studies

By

Ao Li

A dissertation submitted in partial fulfillment of
the requirements for the degree of

Doctor of Philosophy
(Materials Science)

at the
UNIVERSITY OF WISCONSIN-MADISON

2016

Date of final oral examination: 06/08/2016

The dissertation is approved by the following members of the Final Oral Committee:

Izabela S. Professor, Materials Science and Engineering
Dane M. Professor, Materials Science and Engineering
Melih E. Assistant Professor, Mechanical Engineering
Donald S. Professor, Materials Science and Engineering
Susan B. Professor, Materials Science and Engineering

Materials with critical dimension in the nanometer regime have demonstrated superior mechanical properties, including high strength, high hardness, and surface mechanical properties such as low friction and good wear resistance. These superior mechanical properties stem from the density, structure, chemistry, and energetics of interfaces in nanometer scale materials and from the way these interfaces interact with deformation-induced defects. In this thesis, we discuss three types of interfaces, the sliding contact interface between two pieces materials, grain boundaries (GBs) inside materials, and interfaces of nanolayered composite materials.

Chemistry at the silica/silica interfaces can control surface mechanical properties (friction, adhesion, and wear), which are also termed as tribological properties. Tribological properties of silica are of significant importance for a number of technological applications, including wafer bonding in nanoengineering of semiconductor devices and wafer planarization for manufacturing of the microelectromechanical systems (MEMS). Friction and adhesion of silica are also of fundamental interest for geophysics and earthquake mechanics, since quartz is a common component of rocks and shallow tectonic earthquakes are known to result from frictional instabilities in crustal faults. We simulate tribological response of a silica/silica interface with a varying number of interfacial siloxane (Si–O–Si) bridges using molecular dynamic (MD) simulations. Static friction was found to increase linearly with the applied normal pressure, which can be explained in the framework of Prandlt–Tomlinson's model. Friction force was found to increase with increasing concentration of siloxane bridges, but with a decreasing gradient. The latter trend is found to be due to interactions between neighboring siloxane bridges. In addition, we identified atomic-level wear mechanisms of silica. These mechanisms include both transfer of individual atoms accompanied by breaking interfacial siloxane bridges and transfer of atomic cluster initialized by rupturing of surface Si–O bonds. Our simulations showed that small clusters are continually formed and dissolved at the sliding interface, which plays an important role in wear at silica/silica interface.

GBs are another type of interfaces which influence the mechanical properties of materials. Increasing GB density through grain refinement to the nanometer regime has been previously shown to have important effects on friction and wear properties of metals. Using MD we investigated the dependence of friction and wear on grain size in nanocrystalline (nc) copper (Cu). We found that effects of grain size are coupled to the effects of contact size, resulting in a transition from grain-size sensitive regime to grain size-insensitive regime in friction. This transition occurs because for small tips, friction-induced easy shear planes can be entirely accommodated in a single grain, rendering grain boundaries less relevant to sliding resistance. Trends in friction do not follow trends in hardness, which is sensitive to grain diameter in the entire grain size regime considered in this study. We have also discovered that coupling of the effects of grain diameter and contact size leads to an optimum grain size that minimizes formation of wear chips on the surface.

In addition to the density of GBs in Cu, the structures and energetics of GBs, which can be altered by silver (Ag) dopants, also controls mechanical properties of nc copper. In order to study the Ag dopants effects on plasticity of nc Cu, hybrid Monte Carlo/MD simulations are conducted to prepare energetically stable structures of nc Cu with various Ag concentrations. When Ag concentration increases from small to high concentration regime, Ag precipitates grow along grain boundaries and gradually form wetting layers by joining each other. MD simulations of uniaxial tension are also conducted to investigate the effects of Ag dopants on mechanical properties and deformation mechanisms of nc copper. I first found that grain boundary sliding becomes harder with an increase in Ag concentration in both small and large Ag concentration regimes. Surprisingly, I also found that the dislocation density in the interior of grains decreases monotonically with an increase in Ag concentration, which indicates that grain interiors of nc Cu are softened by introduction of Ag

dopants. In addition, there is a critical Ag concentration that maximizes flow stress of nc Cu.The flow stress first increases and then decreases due to a transition of the dominating deformation mechanism, from grain boundary hardening to grain interior softening with Ag concentration increase.

After investigating the contact interfaces and GBs, we studied how the interfaces of Ag/Cu eutectic with layered structures influence the mechanical properties. Through the combination of transmission electron microstructural (TEM) analysis, which was conducted by Prof. Ian Robertson and Dr. Ben Eftink, and MD simulations, bulk Ag/Cu eutectic with incoherent twin interfaces was first compressed through dynamic compressive loading, and was then relaxed in the absence of external load/pressure. It was observed that the total strain of the sample after compression decreased during relaxation. The magnitude of the decrease in strain is attributed to the strain recovered during plastic strain recovery. Plastic strain recovery was caused by dislocation reverse motion and annihilation driven by residual stress. The proposed plastic strain recovery mechanism was confirmed by atomistic visualization and a decrease in dislocation densities during relaxation. Moreover, the misorientation between (111) planes of Ag and Cu phases increased during compression and decreased during relaxation, which was a result of plasticity anisotropy in Ag and Cu phases.

The detailed mechanisms of strain transfer across Ag/Cu interfaces during the deformation were also investigated. A combination of in situ and ex situ TEM straining experiments and MD simulations was used for the study. It was found that minimizing the magnitude of the Burgers vector of the residual dislocation was the dominant factor for determining the outcome of dislocation and deformation twin interactions with both incoherent twin and cube-on-cube interfaces. This factor also determined the conditions under which deformation twins in Ag on intersecting the interface generated deformation twins in Cu. The latter deformation in Cu was not anticipated from the loading condition.

Acknowledgement

I would like to first express my sincere thanks to my advisor, Professor Izabela Szlufarska, who gave me the golden opportunity to pursue doctoral studies at the University of Wisconsin-Madison, and who guided me and supported me with great carefulness for the past four years. She always helps me overcome the hardest obstacles in my research no matter how busy she is. It is not possible for me to accomplish my doctoral studies without her guidance. What I have learned from Professor Izabela Szlufarska is not limited to research. She often spends a lot time and effort in teaching me how to communicate effectively with others including describing scientific question and present research. She is an enthusiastic scientist who sparks my interest in science, but also a very supportive advisor who gives me a lot of freedom in research topics and provides various resources.

I am also grateful to my parents, who selflessly do what they can to help me pursue my dream. I remember that after my first year's study in Madison, I bought a flight ticket back to China to see my parents. My father, however, asked me to focus on my research at school and cancel the flight. Instead, my mom, who is in her fifties, applied for VISA and flied over pacific ocean to the United States twice, just to relieve my homesickness. I am deeply moved by my parents, and I know that my dream is not only my dream, but also the dream of my family.

I thank Professor Dane Morgan for his many great suggestions on my research and on my manner of thinking. One of these suggestions, which I will bear in mind forever, is that I not only need to zoom in to solve narrow perspective problems, but also to zoom out to fully explore the broader perspective findings. I thank Professor Melih Eriten for his tribology course, which is the most helpful course for my tribology research. I thank Professor Donald Stone who has deepened my understanding of dislocation theories through his course MSE 750. I also thank Professor Susan Babcock, Professor Melih Eriten, Professor Dane Morgan, and Professor Donald Stone for taking time out of their busy schedules to serve as committee members in my thesis proposal and dissertation. I benefited a lot from their helpful suggestions and discussions.

I thank Professor Ian Robertson and Dr. Ben Eftink who I collaborated closely with for the Ag/Cu multilayer research. They taught me details in experiments and gave me useful perspective from experiments, which helped me achieve a well-round understanding of the research problem we studied.

I thank Dr. Kai Huang, Dr. Katharina Vortler, and Dr. Yun Liu, who taught me useful simulation techniques and helped me get started with my research. Finally, I would like to thank all members and alumni of Computational Materials Group for their help in my studies and the joyful time which we spent together.

Contents

Chapter 1 Introduction and Motivation

1.1 Interface-Mediated Surface and Bulk Mechanical Properties

Friction and wear are surface mechanical properties that are important for many applications in the manufacturing industr， such as wafer planarization for the microelectromechanical system (MEMS)[1,2,3] and metal-forming operations. Controlled wear process can be also used to remove part of the material and to obtain desired surface geometry. In addition to the benefits of wear, wear is unfavorable in many situations. The reason is that wear can shorten the life time of components of machines, which can be costly to replace or to repair. It was estimated that wear caused annual loss to industries in the United States directly and indirectly for 1-2% of GDP.[4] As a result, many studies have been conducted with the aim to minimize wear through modifying the properties of interfaces.[5,6]

Wear is strongly influenced by chemistry, geometry, and mechanical properties of the interfaces, and operating conditions.[7] According to the Archard's law,[8] the wear volume equals $\frac{kWx}{H}$, where k is the wear coefficient, W is the applied load, x is the sliding distance, and H is the hardness of the surface. As a result, when a hard surface and a soft surface in contact move relative to each other, the softer surface is generally worn more severely. While the Archard's law works for many macroscopic cases,[7] it fails to describe to describe the wear of interfaces at nanometer scale contact.[9] Instead, an atom-by-atom attrition model is proposed which is based on the thermal-activation process with an activation barrier.[9] The activation barrier corresponds to the specific atomic-level wear mechanisms at the interface.

Friction can also be either favorable or unfavorable. Friction is useful when we walk, use tires on a road, brakes in our cars, and use conveyor belts to move objects. However, friction can lead to energy loss and surface damage, which are not desirable. Many surface engineering methods have been used to minimize the friction through modifying interface conditions including surface mechanical properties, interface chemistry, and surface geometries. Besides, friction are of fundamental interest for geophysics and earthquake mechanics, since shallow tectonic earthquakes are known to result from frictional instabilities in crustal faults.[10,11] Based on the Amontons' law which was proposed hundreds of years ago, friction force equals to the product of the normal load and the friction coefficient. In addition to the normal load, friction is also a function of time and sliding velocity. Friction can increase as a function of time during which the contact surfaces are hold together. This phenomenon is referred to as frictional ageing.[12,13] On the other hand, friction can decrease with an increase in sliding velocity, which is termed as velocity weakening.[10] Frictional ageing and velocity weakening both originate from interface-mediated mechanisms and can be described by a phenomenological rate-and-state friction law.[14,15] Though the rate-and-state friction law has been widely supported by many experiments, the specific physical origins at the interfaces are still in debate. For instance, in order to explain the logarithmical frictional ageing, both plastic creep which increases the contact quantity and interfacial chemical bonding which increases contact quality have been proposed. These two hypotheses are likely to happen simultaneously in macroscopic contacts and it is often challenging to isolate one from the other in macroscopic experiments. Recently, single-asperity frictional experiments using atomic force microscope (AFM) are able to eliminate the influences of surface roughness and contact quantity, and demonstrate how friction changes with contact quality such as concentration of interfacial bonds of one asperity. [11]

In addition to the surface mechanical properties of friction and wear, preparing materials with outstanding bulk mechanical properties by controlling interfacial structures and densities is also a

popular research area. One way to enhance the bulk mechanical properties is to increase the densities of intrinsic interfaces, such as grain boundaries (GBs) in polycrystalline and interfaces in layered structures.[16,17] It has been documented that by decreasing the average grain sizes and transform polycrystalline to nanocrystalline (nc), the strength and hardness of materials first increase and then decrease, which provides an optimum grain size that maximizes strength and hardness. When the grain size is larger than the optimum grain size, the deformation mechanism is dominated by dislocation-mediated plasticity, and when the grain size is smaller than the optimum grain size, the deformation mechanism is dominated by GB sliding.

Similar to nc materials, the strengthening mechanisms of multilayered structures can also be controlled by the density of interfaces or layer thickness.[18] When the layer thickness is greater than 100nm, the volume in each layer is large enough to allow for dislocation pile-ups. In this thickness regime, the relation between yield strength and layer thickness obeys the Hall-Petch relation, which means that $\sigma \propto h^{-\frac{1}{2}}$. σ is the yield strength and h is the layer thickness. As the layer thickness decreases to a few nanometers to tens of nanometers, the confined layer slip of treading dislocations becomes the dominating deformation mechanism. In this layer thickness regime, strength-thickness relation deviates from the Hall-Petch relation and obeys to a logarithmic strength dependence on layer thickness as $\sigma \propto \frac{\ln(h/b)}{h}$. Here, b is the burgers vector of a threading dislocation. The threading dislocations are glide dislocations that are confined in one layer of a layered structure, with the two ends of a threading dislocation being connected with interfaces. When a threading dislocation moves in a layer, the restrictions imposed by the interfaces impede the motion of the threading dislocation, which leads to the strengthening. If the layer thickness further decreases below approximately five nanometers, dislocation-interface interactions such as the cutting through of a dislocation through an interface become important. The dominating strengthening mechanism of multilayered structures can

also be controlled by the angle between the loading orientation and the normal direction of the interfaces.[19] Three different deformation mechanisms have been observed to be operated by changing this angle, which are confined layer slip, GB migration, and dislocations' cutting through twin interfaces.

Another promising way to strengthen materials is through introducing dopants to the intrinsic interfaces of nc structures. For immiscible binary alloy such as Cu/Ag, Ag dopants tend to segregate in GBs of nc Cu. The first reason of the strengthening is that dopants segregated in GBs are able to lower the GB energy of and make GB sliding harder, which will increase the strength of nc material.[20] The second reason is that dopants segregated in GBs can stabilize the nc structures by migrating grain coarsening, which preserves the superior mechanical properties of nc materials.[21]

Molecular dynamics (MD) simulations can provide many insights in the studies of interface-mediated mechanical properties due to their advantages in the following aspects. MD simulations first enable us to observe the mechanisms directly. In friction and wear experiments, it is difficult to monitor the mechanisms and structure evolution at the contact interface simply because they are buried during deformation. In contrast, MD simulations are able to reveal the friction and wear mechanisms at such buried surfaces. We are also able to see the interior of a material and observe dislocation reaction, grain boundary sliding, and phase transformation directly. These direct observations are helpful in identifying various mechanisms. In addition, interface conditions can be well controlled in MD simulations, which can help us determine the dominating mechanism by removing other interfering factors. For instance, using MD we are able to remove influence of surface roughness by generating a perfectly smooth surface. In experiments, it is difficult to prepare several nanometer-scale tips with completely the same geometry, which can be easily done in MD simulations to avoid tip-geometry influences. Lastly, as we can obtain complete information of atoms' position and velocities, many useful properties can be calculated through statistical mechanics and

rigorous mathematical expressions. These properties include both macroscopic properties such as pressure and temperature, and atomic local properties such as atomic potential energy and atomic local stress which are difficult to obtain from experiments.

1.2 Overview of the Thesis

The remainder of the thesis is composed of 7 chapters. Chapter 2 discusses the basic algorithms of MD simulations, property calculations from a MD system, concepts of thermostat and barostat, and several types of force fields used in the following chapters. Other useful algorithms are also introduced including a hybrid Monte Carlo (MC)/MD algorithm, common neighbor analysis (CNA) algorithm, dislocation extraction algorithm (DXA), and atomic local shear strain algorithm.

Chapters 3-7 discuss interface-mediated mechanical properties of three types of systems, including silica/silica interfaces (in Chapter 3), nc Cu or Cu/Ag alloys (in Chapter 4 and 5), and multilayered Cu/Ag alloys (in Chapter 6 and 7). In Chapter 3, silica/silica interfaces with various concentrations of interfacial siloxane bonds are prepared and how the interfacial bonding influences friction and wear at silica/silica is investigated. In Chapter 4, substrates of nc Cu with different average grain diameters are scratched by SiC tips with various tip radiuses. The coupling of the intrinsic size effect and extrinsic size effect on friction and wear of nc Cu have been discussed. In Chapter 5, the morphology, structure and energetics of Cu/Ag alloys are demonstrated for a wide range of Ag concentrations. The influence of Ag concentration on the mechanical properties and deformation mechanisms is also discussed. Chapter 6 studies how the interface types between Ag and Cu phases and the loading orientations influence the deformation mechanisms, and the occurrence of plastic strain recovery. Chapter 7 discusses the interactions between dislocations and the Ag/Cu interfaces, and how different interactions lead to different post-deformation microstructures. Chapter 8 concludes the thesis and discusses potentially interesting studies following the thesis.

References

1 Lasky, J.B. : Wafer bonding for silicon-on-insulator technologies. Appl. Phys. Lett. 48, 78-80 (1985).

2 Ventosa, C., Rieutord, F., Libralesso, L., Morales, C., Fournel, F., Moriceau, H.: Hydrophilic low-temperature direct wafer bonding. J. Appl. Phys. 104,123524 (2008).

3 E. Taran, E., Donose, B.C., Vakarelski, I.U., Higashitani, K.: pH dependence of friction forces between silica surfaces in solutions. J. Colloid Interface Sci. 297, 199-203 (2006).

4 Z. Gahr, Karl-Heinz Microstructure and Wear of Materials. Tribology Series, 10. Elsevier. ISBN 0-444-42754-6. (1987).

5 Y.-R. Jeng, P.-C. Tsai, S.-H. Chiang,: Effects of grain size and orientation on mechanical and tribological characterizations of nanocrystalline nickel films. Wear 303, 262-861 (2013).

6 Z. N. Farhat, Y. Ding, D. O. Northwood, A. T. Alpas, : Effect of grain size on friction and wear of nanocrystalline aluminum. Mat Sci Eng a-Struct 206,302-313 (1996).

7 B. Bhushan, Principles and Appliations of Tribology. (A John Wiley & Sons Ltd., New York, ed. 2, 2013).

8 Archard, J.F.: Contact and rubbing of flat surfaces. J. Appl. Phys. 24, 981-988 (1953).

9 Bhaskaran, H., Gotsmann, B., Sebastian, A., Drechsler, U., Lantz, M.A., Despont, M., Jaroenapibal, P., Carpick, R.W., Chen, Y., Sridharan, K.: Ultralow nanoscale wear through atom-by-atom attrition in silicon-containing diamond-like carbon. Nat. Nanotechnol. 5, 181-185 (2010).

10 Scholz, C.: Earthquakes and friction laws. Nature 391, 37-42 (1998).

11 Li, Q., Tullis, T.E., Goldsby, D., Carpick, R.W.: Frictional ageing from interfacial bonding and the origins of rate and state friction. Nature 480, 233-236 (2011).

12 Bocquet, L., Charlaix, E., Ciliberto, S., Crassous, J.: Moisture-induced ageing in granular media and the kinetics of capillary condensation. Nature 396, 735-737 (1998).

13 Dieterich, J.H.: Time-dependent friction in rocks. J. Geophys. Res. 77, 3690-3697 (1972).

14 Ruina, A.: Slip instability and state variable friction laws. J. Geophys. Res. 88, 10359-10370 (1983).

15 Dieterich, J.: Modeling of rock friction: 1. Experimental results and constitutive equations. J. Geophys. Res. 84, 2161-2168 (1979).

16 J. Schiotz, K. W. Jacobsen, : A Maximum in the Strength of Nanocrystalline Copper Science 301, 1357-1359 (2003).

17 J. Schiotz, F. D. Di Tolla, K. W. Jacobsen, : Softening of nanocrystalline metals at very small grain sizes. Nature 391, 561-563 (1998).

18 J. A. El-Awady, and N. M. Ghoniem, Plastic flow in confined volumes. The Minerals, Metals & Materials Society, (2008).

19 Z. You, X. Li, L. Gui, Q. Lu, T. Zhu, H. Gao, and L. Lu, Plastic anisotropy and associated deformation mechanisms in nanotwinned metals. Acta Materialia 61, 217-227 (2013).

20 N. Q. Vo, J. Schafer, R. S. Averback, K. Albe, Y. Ashkenazy, and P. Bellon, Reaching theoretical strengths in nanocrystalline Cu by grain boundary doping. Scripta Materialia 65, 660-663 (2011).

21 H. A. Murdoch, C. A. Schuh, Estimation of grain boundary segregation enthalpy and its role in stable nanocrystalline alloy design. Journal of Materials Research 28, 2154-2163 (2013).

Chapter2 Simulation Techniques

2.1 Introduction to Molecular Dynamics (MD)

2.1.1 Basic Algorithm of MD

MD is a computational simulation technique for studying the dynamical evolution of a many-body system. The MD simulation is classical which means that the mass centers of constituent particles follows the laws of classical mechanics. Atoms' positions will be updated at discrete times by numerically solving the Newton's equation of motion:

$$m_i \frac{d^2\vec{r_i}}{dt^2} = \sum_{j\neq i} \overrightarrow{F_{ij}} + \overrightarrow{F_{ext,i}} \qquad (2.1.1)$$

for each atom. m_i is the mass of the atom i, $\vec{r_i}$ is the atom's position, $\overrightarrow{F_{ij}}$ is the interatomic force on atom i exerted by atom j, and $\overrightarrow{F_{ext,i}}$ is the external force on atom i. At time t, the total force on atom i is $\sum_{j\neq i} \overrightarrow{F_{ij}} + \overrightarrow{F_{ext,i}}$ and the acceleration of motion is $\frac{d^2\vec{r_i}}{dt^2}$. After a timestep Δt, a new position and velocity for atom i will be calculated from Eq. 2.1.1. Various algorithms can be used to run MD simulations. The Velocity-Verlet algorithm is one of the most widely used algorithms which implements the following equations to update atoms' coordinates and velocities:

$$\vec{r_i}(t+\Delta t) = \vec{r_i}(t) + \vec{v_i}(t)\Delta t + \frac{\vec{F_i}(t)}{2m_i}(\Delta t)^2 \qquad (2.1.2)$$

$$\vec{v_i}(t+\Delta t) = \vec{v_i}(t) + \frac{\vec{F_i}(t)+\vec{F_i}(t+\Delta t)}{2m_i}\Delta t \qquad (2.1.3)$$

MD simulations are called deterministic simulations because trajectories of atoms can be obtained by integrating the Newton's equation of motion. Once the positions and velocities of each atom in the

system are known at one time, the positions, velocities and accelerations of these atoms can be predicted at any time in the future or the past.

2.1.2 Property Calculation

MD simulations can be used to calculate properties such as temperature and pressure, which are functions of the positions, velocities and forces of atoms in a system. The temperature of a system is calculated by the equation:

$$T = \frac{\sum_i^N m_i v_i^2}{DNk_B}, \tag{2.1.4}$$

where N is the total number of atoms in the system, m_i is the mass of atom i, v_i is the velocity of atom i, D is the dimensionality of the system, and k_B is the Boltzmann constant. This definition of temperature is derived from the equipartition theorem, which states that the kinetic energy is equally divided among all kinetic degrees of freedom. Several equivalent ways can be used to measure the pressure of a MD system. The most common method for pressure calculation is based upon virial equation.[1] The pressure of a system is given by the equation:

$$P = \frac{\sum_i^N m_i v_i^2}{DV} + \frac{\sum_{i=1}^{N-1} \sum_{j=i+1}^{N} \overrightarrow{r_{ij}} \cdot \overrightarrow{F_{ij}}}{DV}, \tag{2.1.5}$$

where $\overrightarrow{r_{ij}}$ is the distance between atoms i and j, and V is the volume of the system. For a two-dimension system, V is the area.

The properties mentioned above are calculated only based on one state at one time point. These properties have to be averaged in MD simulations to estimate the true thermodynamics properties. Two most common averaging techniques are ensemble average and time average. Ensemble average can be calculate as:

$$< A >_{ensemble} = \int \int A(q,p) P(q,p) \mathrm{d}q \mathrm{d}p, \tag{2.1.6}$$

where q represents generalized coordinates (here, atomic positions) and p represents the conjugate momenta (here, momenta of atoms). For a system with N atoms, one state point $X=(q,p)$ has $6N$ degrees of freedom. $P(q,p)$ is the probability of state $X=(q,p)$, and $A(q,p)$ is the property value of state $X=(q,p)$. The probability function can be determined from statistical mechanics. For instance, in the case of constant temperature – constant volume ensemble it is

$$P(q,p) = \frac{e^{-E(q,p)/k_B T}}{\int\int e^{-E(q,p)/k_B T} \mathrm{d}q\mathrm{d}p}, \qquad (2.1.7)$$

where $E(q,p)$ is the energy of the system at state $X=(q,p)$.

In MD simulations one explores the different microstates $X(q,p)$ by evolving the system in time and calculating properties at different time steps, that is

$$< A >_{time} = \lim_{t\to\infty} \frac{\int_{t_0}^{t_0+t} A(t)\mathrm{d}t}{t}, \qquad (2.1.8)$$

where t represents time. The so-called ergodic assumption underlying this method is that as the system evolves in time, it visits the different microstates with correct probabilities $P(q,p)$. For instance, one can show theoretically that a system evolving according to equations (2.1.2) and (2.1.3), with Δt infinitesimately small, explores different microstates with probabilities corresponding to the constant energy-constant volume (microcanonical) ensemble. In order to simulate other ensembles (e.g., constant temperature constant pressure), it is necessary to modify equations (2.1.2) and (2.1.3) and the corresponding integration scheme. Multiple reliable methods have been developed and tested for such simulations.

2.1.3 Thermostat and Barostat

Several types of algorithms can be used to perform simulations at constant temperature, including rescaling of velocities, stochastic methods, and deterministic methods. Rescaling of velocities, which is based on equation 2.1.4, is the simplest and the fastest approach, but it is also the

least realistic. Even though average properties calculated from atomic coordinates are still correct since positions are not modified by this algorithm, properties related to the atomic velocities are incorrect. In most cases, rescaling of velocities is used to prepare/equilibrate a system, but not in the production part of the simulation where properties need to be calculated. Stochastic methods generate microstates randomly according to probabilities corresponding to the correct ensemble (NVT or NPT). Examples of stochastic methods are the Andersen thermostat[2] and the Langevin thermostat[3]. For instance, in the Andersen thermostat method, velocities of atoms are reassigned from a given temperature distribution if these atoms collide with imaginary bath particles. Static properties can be calculated correctly from an MD simulation with a stochastic thermostat. However, dynamic properties, such as diffusion coefficient are incorrect because momentum transport is destroyed in such methods. Thermostats based on deterministic methods give static and dynamic properties correctly. These thermostats are called deterministic because no random velocities are generated in the process and the system evolves according to a modified Newton's equation of motion. The most common thermostat based on deterministic method is the Nose-Hoover thermostat[4], which introduces extra an additional degree of freedom to represent the thermostat. The temperature of the original system can be controlled by exchanging energy with this degree of freedom, though the energy of the extended system (consisting of the simulated physical system and the thermostat) is still conserved. To simulate systems at constant pressure, one can use a similar approach to the deterministic approach described above. In the Nose-Hoover method one couples the physical system to a a barostat by introducing an additional degree of freedom to control the pressure.

2.2 Force Fields

In order to solve the Newton's equation of motion, the force $\vec{F_i}$ on atom i is calculated from interatomic potentials or the force fields. The force fields are often equations based on physics and

the parameters in such equations are fitted to experimental data or to first principle calculations. It is at the heart of MD simulations that the chosen force field describes the physics and mechanisms in question. For instance, when we simulate a process which involves formation and breaking of covalent Si-O bonds, non-bonded force fields such as Lennard-Jones (LJ) can not be used, and force fields considering chemical reaction kinetics such as ReaxFF are more applicable. In the remainder of this section, the force fields used in my studies will be briefly described.

2.2.1 Lennard-Jones Force Field

The LJ force field[6] is one of the simplest force fields and its 12-6 form is:

$$U^{LJ}(r) = 4\varepsilon[(\frac{\sigma}{r})^{12} - (\frac{\sigma}{r})^{6}], \qquad (2.2.1)$$

where U^{LJ} is the potential energy, r is the distance between two atoms, σ characterizes the width of the energy well, and ε is the depth of energy well. The term $4\varepsilon(\frac{\sigma}{r})^{12}$ represents the repulsive interaction which describes Pauli repulsion at short distances due to overlap of electron orbitals. The term $-4\varepsilon(\frac{\sigma}{r})^{6}$ is the attractive long-range term, which describes long-range attraction forces such as van der Waals force and dispersion force. LJ force field is accurate for noble gas atoms and is a relatively good approximation for liquid simulations. In my studies, LJ force field is used to describe interactions between SiC tip and Cu substrate during frictional sliding. LJ force field is applicable in this case because it can avoid strong bonding reactions between tip and substrate, which are not the subject of my studies.

2.2.2 Embedded Atom Method Force Field

The embedded atom method (EAM) force fields[7] are particularly appropriate for metallic systems, for which the potential energy of an atom *i* is given by the equation:

$$E_i = F_\alpha(\sum_{j\neq i}\rho_\beta(r_{ij})) + \frac{1}{2}\sum_{j\neq i}\Phi_{\alpha\beta}(r_{ij}), \qquad (2.2.2)$$

where F_α represents the embedding energy required to place atom *i* of type α into the electron cloud, r_{ij} represents the distance between atoms *i* and *j*, ρ_β represents the contribution from atom *j* of type β to the electron charge density of atom *i*, and $\Phi_{\alpha\beta}$ is a pair-wise potential function. EAM is a multibody force field since the electron cloud density is a summation over contributions from many atoms. In our studies, EAM force field is used for simulating Cu and Cu/Ag alloys. These simulations are described in Chapters 4-7.

2.2.3 Reactive Force Field

Reactive force field (ReaxFF)[8] is a bond order based force field which is able to simulate reactive chemical systems in large scale MD simulations. ReaxFF force field can not only describes the static equilibrium energy, but also energy barriers of chemical reactions. The energy of a system described by the ReaxFF force field is a summation of various partial energy contributions. The partial energy that distinguishes the ReaxFF from empirical nonreactive force fields is the bond energy, which is a function of bond order. The bond order is calculated from interatomic distances using the formula:

$$BQ'_{ij} = \exp\left[p_{bo,1}\cdot(\frac{r_{ij}}{r_0})^{p_{bo,2}}\right] + \exp\left[p_{bo,3}\cdot(\frac{r_{ij}{}^{\pi}}{r_0})^{p_{bo,4}}\right] + \exp\left[p_{bo,5}\cdot(\frac{r_{ij}{}^{\pi\pi}}{r_0})^{p_{bo,6}}\right], \quad (2.2.3)$$

where the three exponential terms correspond to the sigma bond, the first π bond, and the second π bond. r_0 is bond radii, r_{ij} is interatomic distance, and $p_{bo,1}$-$p_{bo,6}$ are parameters. ReaxFF force field also has a bond order correction term which describes the influence of coordination number of the atom on the bond order. The bond energy can thus be a function of the corrected bond order:

$$E_{bond} = -D_e\cdot BO_{ij}\cdot\exp\left[p_{be,1}(1-BO_{ij}{}^{p_{be,1}})\right], \qquad (2.2.4)$$

where BO_{ij} is the corrected bond order, and D_e and $p_{be,1}$ are parameters. ReaxFF will consider a bond as being weaker if the bonded atoms are over-coordinated, while the attractive regime of the

bonds will increase if atoms are under coordinated. ReaxFF force field is used in our studies to simulate adhesive friction and wear at silica/silica interfaces in Chapter 3, which involve formation and breaking of chemical bonds.

2.3 Other Algorithms

A number of other algorithms in addition to the basic MD algorithm have been used in my studies. The remainder of the section will discuss four of these algorithms, which are the major tools in my simulations.

2.3.1 Alloying Algorithm

A hybrid Monte Carlo (MC)/MD algorithm[9] can be utilized to introduce alloying elements to the metallic system, and to relax the structures energetically. The key idea of this method is to perform iteratively transmutational MC steps, which sample semi-grand-canonical ensemble, and MD simulations for n steps. In the MC run, trial swaps are carried out by randomly selecting an atom and by replacing it with the other species. The trial moves are accepted or rejected according to the Metropolis algorithm, which calculates acceptance probability A_s based on energy change in atom swaps according to the following formula:

$$A_s = \min\{1, \exp[-\frac{(\Delta U + \Delta\mu N \Delta c)}{k_B T}]\}, \qquad (2.3.1)$$

where k_B is Boltzmann constant, T is the temperature, ΔU is the change in potential energy, $\Delta\mu$ is the chemical potential difference between the two elements, and N is the total particle number of the system. MD structural relaxation, which is often coupled with thermostat and barostat, follows the MC steps. The NPT ensemble is often used in the MD part of the algorithm because the two elements often have different atomic radii, which may lead to unrealistic pressure change due to alloying. The

hybrid MD/MC algorithm is used in Chapter 5 as an effective alloying method to prepare energetically stable alloy structure.

2.3.2 Common Neighbor Analysis

Defects in crystalline materials play an important role in determining materials properties. A number of post analysis algorithms have been developed to identify defects and defect-free regions based on generated atoms' positions. Common Neighbor Analysis (CNA)[10] is one of the most commonly used defect-identification algorithm.

CNA of an atom is calculated from the topology of the bonds between this atom and its neighbor atoms. Whether two atoms are neighbors is determined by the distance between these two atoms. When the distance is smaller than the cutoff r_{cut}, the two atoms are considered as neighbors. The r_{cut} is often set to be the average of first and second neighbor shell distances for face-centered cubic (FCC) and body-centered cubic (BCC) structures by the formula:

$$r_{cut}^{fcc} = \frac{1}{2}\left(\sqrt{1/2} + 1\right)a_{fcc}\,, \qquad (2.3.2)$$

$$r_{cut}^{bcc} = \frac{1}{2}\left(\sqrt{2} + 1\right)a_{bcc}\,, \qquad (2.3.3)$$

where a_{fcc} and a_{bcc} are lattice constants of FCC and BCC crystal structures. In order to determine the local structure of an atom, three integer numbers are computed for each of its *N* neighbors. The three numbers are n_{cn}which is the number of common neighbor atoms shared by both the center atom and its neighbors, n_b which is the number of bonds between these common neighbor atoms, and n_{lcb} which is the number of the longest chain of bonds connecting these common neighbors. For one center atom, by comparing the three numbers of the neighbors with the numbers of reference

FCC,BCC, hexagonal-close-packed structures (HCP), and cubic diamond structures, the structure type of the center atom can thus be identified. The CNA method is used in Chapters 4-7.

2.3.3 Intragranular Dislocation Density

Dislocation Extraction Algorithm (DXA) is able to identify dislocation defects based on atomic positions of a system and determine Burgers vectors of these dislocations. There are four major steps for DXA to extract continuous dislocation lines from atoms' positions. The first step is to use CNA (discussed in section 2.3.2) to identify crystalline atoms and defect atoms. The second step is to construct an interface mesh which separates regions of crystalline atoms and regions of defect atoms. The third step is to construct Burgers circuits on the interface mesh constructed in the second step, and to identify Burgers vectors from the contructed Burgers circuits (if dislocations are present). The fourth step is to use a line connecting the centers of the identified Burgers circuits. The line generated in the fourth step is the dislocation line.

DXA can be used to identify all dislocations and calculate the total dislocation length in a polycrystalline or layered systems. However, DXA may report spurious dislocations in highly distorted regions such as GBs and other interfaces, which a human would not consider proper dislocations. These spurious dislocations identified by DXA lead to an unreasonably high dislocation density. In our studies of Chapter 5 and Chapter 6, only intragranular dislocations are considered for dislocation length calculation because these dislocations are responsible for intragranular dislocation entanglements and strain hardening. Intragranular dislocation density is calculated in four steps. In the first step, atoms at GBs and interfaces are identified by CNA algorithm. The defect atoms are considered as GB atoms. In the second step, these identified GB atoms are deleted. In the third step, the structures without GB atoms are analyzed by DXA, which calculates the total length of intragranular dislocations $l_{interior}$. In the last step, intragranular dislocation density ρ is calculated by

$\rho = \frac{l_{interior}}{V_{interior}}$, in which $V_{interior}$ is the total volume of grain interior. $V_{interior}$ is calculated by $(N - N_{GB}) \times v_{crystal}$, in which N is the total number of atoms in the system, N_{GB} is the number of deleted GB atoms, and $v_{crystal}$ is the volume of an atom in pure crystal.

2.3.3 Atomic Local Shear Strain

To investigate deformation mechanisms and quantify plastic deformation, atomic local shear strain is introduced which is helpful to illustrate local deformation. Two atomic configurations are required to calculate atomic local shear strain, a current configuration and a reference configuration. Here the configuration during or after tension is set as the current one and the initial configuration before tension is set as the reference one. For each atom *i* in the system, its position relative to its neighbors changes after deformation. This position change relative to an atom's neighbors can be represented as

$$\{d_{ji}^0\} \rightarrow \{d_{ji}\}, \forall j \in N_i^0, \qquad (2.3.4)$$

where d_{ji}^0 and d_{ji} are vectors between atom j and i in the reference configuration and current configuration. j atom is one of the nearest neighbors of atom i, and N_i^0 is the total number of the nearest neighbors of atom i. A local transformation matrix

$$J_i = (\sum_{\forall j \in N_i^0} d_{ji}^{0T} d_{ji}^0)^{-1} (\sum_{\forall j \in N_i^0} d_{ji}^{0T} d_{ji}), \qquad (2.3.5)$$

can be calculated from d_{ji}^0 and d_{ji}, which is able to minimize

$$\sum_{\forall j \in N_i^0} |d_{ji}^0 J_i - d_{ji}|^2. \qquad (2.3.6)$$

A local strain tensor can be calculated from J_i by the formula:

$$\eta_i = \frac{1}{2}(J_i J_i^T - I). \qquad (2.3.7)$$

This local strain tensor best approximates the atomic-scale local deformation around atom i. Von Mises shear strain invariant is then calculated from the local strain tensor and assigned to each atom, which is the so-called atomic local shear strain:

$$\eta_i^{Mises} = \sqrt{\eta_{yz}^2 + \eta_{xz}^2 + \eta_{xy}^2 + \frac{(\eta_{yy}-\eta_{zz})^2+(\eta_{xx}-\eta_{zz})^2+(\eta_{xx}-\eta_{yy})^2}{6}}. \quad (2.3.8)$$

Analysis of the statistical distribution and geometrical distribution of atomic local shear strain helps demonstrate deformation mechanisms in Chapter 4 and Chapter 5.

References

1 A.P., Thompson, S.J, Plimpton, W. Mattson: General formulation of pressure and stress tensor for arbitrary many-body interaction potentials under periodic boundary conditions. J. Chem. Phys. 131, 154107 (2016).

2 H.C., Anderson: Molecular dynamics simulations at constant pressure and/or temperature. J. Chem. Phys. 72, 2384 (1980).

3 B., Dunweg, W., Paul,: Brownian Dynamics Simulations Without Gaussian Random Numbers. International Journal of Modern Physics C 2, 817-827 (1991).

4 N., Shuichi : A unified formulation of the constant temperature molecular-dynamics methods. Journal of Chemical Physics 81, 511 (1984).

5 H. J. C. Berendsen, J. P. M. Postma, W. F. van Gunsteren, A. DiNola, J. R. Haak: Molecular dynamics with coupling to an external bath. 81, 3684 (1984).

6 J. E. Jones,: On the Determination of Molecular Fields. Proceedings of the Royal Society of London. Series A 106, 463 (1924).

7 P.L. Williams, Y. Mishin, J.C. Hamilton,: An embedded-atom potential for the Cu-Ag system, Modelling Simul. Mater. Sci. Eng. 14, 817 (2006).

8 A. C. T. van Duin, S. Dasgupta, F. Lorant, W. A. Goddard III: ReaxFF: A Reactive Force Field for Hydrocarbons. J. Phys. Chem. A 105, 9396–9409 (2001).

9 B. Sadigh, P. Erhart, A. Stukowski, A. Caro, E. Martinez, L. Zepeda-Ruiz,: Scalable parallel Monte Carlo algorithm for atomistic simulations of precipitation in alloys. PHYSICAL REVIEW B 85, 184203 (2012).

10 J. D. Honeycutt, H. C. Andersen,: Molecular dynamics study of melting and freezing of small Lennard-Jones clusters. J. Phys. Chem. 91, 4950–4963 (1987).

11 A. Stukowski, K. Albe,: Extracting dislocations and non-dislocation crystal defects from atomistic simulation data. Modelling Simul. Mater. Sci. Eng. 18, 085001 (2010).

12 F. Shimizu, S. Ogata, J. Li,: Theory of Shear Banding in Metallic Glasses and Molecular Dynamics Calculations. Materials Transactions 48, 2923-2927 (2007).

Chapter 3 Effects of Interfacial Bonding on Friction and Wear at Silica/Silica Interfaces

3.1 Introduction

Tribological properties (friction, adhesion, and wear) of silica are of significant importance for a number of technological applications, including wafer bonding in nanoengineering of semiconductor devices[1,2] and wafer planarization for manufacturing of the microelectromechanical systems (MEMS).[3] Friction and adhesion of silica are also of fundamental interest for geophysics and earthquake mechanics, since quartz is a common component of rocks and shallow tectonic earthquakes are known to result from frictional instabilities in crustal faults.[4,5] Consequently, it is not surprising that friction of silica has been studied extensively in different contexts.[6,7,8,9,10] One aspect of the silica studies, which is particularly relevant to this paper is related to the effects of surface chemistry on friction[11,12,13]

Silica surfaces, unlike the bulk silica, have largely lost the complete tetrahedral configuration, which gives the surface silicon atoms the tendency to bond with chemical groups.[14] Due to this tendency, hydroxyl groups (-OH) can bind to silicon atoms on silica surfaces via Si-O covalent bonds. When the concentration of the hydroxyl groups is sufficiently high, the silica surface will show a hydrophilic property and water molecules can be absorbed by forming hydrogen bonds with the surface hydroxyls.[15] When the surface chemical groups are mainly surface siloxanes (Si-O-Si), which can be achieved by dehydroxylation of the surface hydroxyls, the surface will become hydrophobic.[16] Various kinds of interactions may exist between silica surfaces, such as hydrogen bond network,[11] capillary force of a condensed water meniscus,[17,18] colloidal interactions,[16,19] and covalent bonding via interfacial siloxane bridges[16], which have been reviewed in detail in Ref. [16]. These interaction

mechanisms play an important role in friction and wear of silica/silica interfaces. For example, friction increases with increasing velocity when surfaces are terminated with Si-O-Si groups and it decreases with velocity when surfaces are terminated with hydroxyl groups. The latter effect has been explained by the fact that hydroxyl groups are capable of forming H-bond networks at the interface, and a slower sliding velocity leads to formation of a stronger (more extensive) H-bond network.[11] In addition, surface damage will occur quickly during shearing of two hydrophilic silica surfaces past each other.[16] This is because silica surfaces are capable of forming strong Si-O-Si bonds across the interface through dehydroxylation reaction between two hydroxyls from each surface. These strong covalent Si-O-Si bridges can break during frictional sliding or pull atoms out of silica surfaces, which causes localized surface damage.

Atomic level wear of silica has been previously studied in experiments that combined atomic force microscopy (AFM) and transmission electron microscopy (TEM).[20] Specifically the authors investigated wear between a silica surface and a silicon containing diamond like carbon (DLC) tip[20]. It was found that the classical wear law of Archard[21] fails to describe wear at the nanometer scale. The authors proposed an atom-by-atom attrition model, which was able to successfully describe the experimentally measured rate of wear of a blunted tip. The authors fitted the model to the experimental data to obtain activation energies of the elemental wear processes, but the specific atomic-level wear mechanisms were not identified. In addition, since the experiments were carried out on the interface between SiO_2 and silicon containing DLC, the wear mechanisms in these experiments may be different from those encountered at SiO_2/SiO_2 interfaces. Understanding of such mechanism is important for development of predictive models of wear with correct activation energies. Simulations based on the molecular dynamics (MD) technique provide an excellent tool for identifying wear mechanisms directly. In the present work, we use MD to determine specific wear

mechanisms that occur during shearing of two contacting silica surfaces to provide their atomic level description.

Another interesting phenomenon related to friction and adhesion of silica reported in the last few years is that chemical reactions in silica/silica contacts can lead to contact ageing.[22,23] Ageing refers to an increase of static friction as a function of time during which the surfaces are held in contact before sliding. Another manifestation of the same phenomenon is the so-called velocity weakening, which means that friction decreases with an increasing sliding velocity. Existence of velocity weakening is known to be a necessary condition for nucleation of earthquakes.[4,5] Frictional ageing has been described by a phenomenological rate and state friction laws[24,25], which state that friction depends logarithmically on time. While this law has been validated and widely accepted, [26,27,28,29] the physical origin of frictional ageing has remained a subject of debate. Two main hypotheses are plastic creep (which increases the contact area and therefore friction as a function of time) and chemical bonding (which increases adhesion as a function of time without necessarily increasing the contact area). Both of these phenomena are likely to be active in macroscopic experiments on rocks and in crustal faults, but they have been difficult to isolate from each other in laboratory experiments.

Recently, single-asperity friction experiments between amorphous silica surfaces, carried out by Li *et al.*[5] using AFM, demonstrated that frictional strength of nanometer-scale silica interface can increase logarithmically with the stationary holding time even in the absence of plastic deformation.[5] Specific mechanisms responsible for this chemical ageing have been subsequently proposed by Liu and Szlufarska based on the results of atomistic simulations.[30] The authors excluded the hypotheses that the chemical ageing observed in the AFM experiments of Li *et al.*[5] was due to meniscus formation or due to formation of a hydrogen bond network, as the time scales for these processes were significantly shorter than the ageing time measured in experiments. It was proposed that chemical ageing of silica is due to formation of strong siloxane bonds across the sliding interface.

The authors of Ref [30] employed a combination of density functional theory calculations, MD simulations based on empirical potentials, and kinetic Monte Carlo method, to show that the concentration of siloxane bridges increases logarithmically with time on the time scales comparable to the ageing time reported from AFM experiments. The authors also found that the energy barriers to formation of interfacial siloxane bridges on the neighboring sites are not independent of each other and that this interaction is mediated by the elastic deformation of the surrounding bulk. Friction studies were not reported in Ref. [30] and it was hypothesized that the static friction forces scales linearly with the number of covalent bonds formed across the interface. This assumption has been shown to be valid before for friction between a hydrogen passivated DLC AFM tip and hydrogen passivated diamond sample.[31,32] It is also expected that this assumption will be valid for the silica interface in the regime where the density of siloxane bridges across the interface is relatively low. For higher concentration of the siloxane bridges, it is possible that the interaction between these bridges will lead to deviations from the linear relationships between the static friction force and the number of bridges, but this dependence has not been investigated up to this point. Here, we use MD simulations to determine how static friction force in sliding interface depends on the number of siloxane bridges formed across silica/silica interface.

3.2 Methods

We carry out MD simulations of sliding between two silica surfaces as a function of the number of siloxane bridges formed across the sliding interface. Simulations are performed with the ReaxFF reactive force field,[33] as implemented in LAMMPS.[34] We consider hydrophobic silica surfaces because hydrophobic surfaces are shown in experiments to have a higher friction and a more apparent ageing behavior than those of hydrophilic silica surfaces.[16]

Figure 3.2.1 shows how one sliding interface is formed between two amorphous silica samples. Each sample (6.13nm × 5.31nm × 3.37nm) consists of 2,592 silicon atoms and 5,184 oxygen atoms. It is prepared by melting the system at 5,000K for 10 ns, quenching it down to 5K in 20ns, and then equilibrating for 30ns at 5K. Periodic boundary conditions are employed in the *x* and *y* directions (both parallel to the interface), resulting in one infinite silica/silica interface. Amorphization of the sample has been confirmed by calculating the pair distribution function. The two silica samples are referred to as bottom and top, respectively. All atoms in the bottom sample are divided into three groups, the bottom frozen layer, the bottom thermostat layer, and the bottom free surface layer, based on their *z* coordinates, where *z* direction is perpendicular to the interface. Atoms in the bottom frozen layer (0Å < *z* < 4Å) are not allowed to relax during the sliding simulations. Above the 4Å-thick bottom frozen layer is an 8Å-thick bottom thermostat layer. A velocity-rescaling algorithm is applied to atoms in this layer to explicitly rescale the temperature back to 5K every 25fs. Above the bottom thermostat layer is the bottom free surface layer (all atoms with *z* coordinates bigger than 12Å), which is simulated with a constant energy ensemble. The top surface is modeled using a symmetric approach. Interface is formed by bringing the two surfaces together. The dimensions of the resulting silica/silica interface are 6.13nm × 5.31nm.

In order to prepare interfaces with different numbers of siloxane (Si-O-Si) bridges across the interface, we follow three steps. First, we perform indentation simulations continuously with the velocity of 50m/s until the normal pressure reaches 8GPa. The interface is then equilibrated at 5K for 50ps. The interface pressure is calculated by dividing the normal force acting on the interface by the nominal interfacial area. The total normal force is calculated as the sum of normal forces acting on atoms in top frozen layer. The reason for increasing the normal pressure is that it accelerates reactivity of the surfaces.

In the second step we facilitate chemical reactions between silica surfaces. In AFM experiments chemical bonding of silica/silica interfaces was reported to occur on the time scale of 0.1-100 seconds [5] [30]. This time scale is too long for interfacial reactions to be modelled directly in MD simulations. The reason why bridge formation reaction is relatively slow is that surface silicon atoms are typically bonded to four oxygen atoms, where the oxygen atoms form a (possibly distorted) tetrahedron. Because all Si bonds are saturated in this arrangement, formation of an interfacial Si-O bridge involves first breaking of one of the surface Si-O bonds on each surface and only then formation of a Si-O-Si bridge is possible. The first step is the one that cannot be directly observed in MD simulations. Therefore we accelerate the overall bonding process by introducing reactive sites on the surface, which means that we remove from the surface those oxygen atoms that have dangling bonds, i.e., they are bonded only to one Si atom. As a result, the Si atom to which the O atom used to be bonded now has fewer bonds than four and therefore this Si will have a stronger tendency to from an interfacial bond. Two such under-coordinated silicon atoms from the opposite surfaces can easily form a Si-O-Si bridge, provided that one oxygen atom is present in the middle between these two Si atoms and that the distances between Si and O atoms are smaller than the Si-O bond length. After removing the dangling O atoms, we search for the reactive sites on the opposite surfaces and if the distance between two reactive Si atoms is lower than 3.6 Å (which is twice the length of the Si-O bond), we add back an oxygen atom in the middle of the distance between the two Si atoms. The interface is then relaxed one more time with ReaxFF, [33] so that the actual reactions and surface relaxation are controlled by the physics of the force field. By creating different numbers of reactive sites, we can generate different number of interfacial Si-O-Si bridges after relaxations. One should note that the reactive sites are introduced to surfaces that had been first prepared and relaxed using the ReaxFF force field and therefore are expected to represent the chemistry of a realistic silica surface. In addition, although we introduce the reactive sites “by hand”, these sites correspond to

positions on the surface where reactions would be most likely if MD simulations were possible on longer time scales. The above scheme allows obtaining realistic silica interfaces with a controlled number of interfacial bonds. This approach is reasonable given that our focus is not on the process of bond formation, but on the effect of the number of interfacial bonds (once they have been formed) on friction.

In the third and final step, we pull the surfaces apart continuously with a velocity of 25m/s. During this phase, we store intermediate configurations corresponding to different normal pressures between -5.4GPa and -1.3GPa. For a given interface, the number of interfacial bridges was found to be constant in this pressure range. In separate simulations, we equilibrate these intermediate configurations of silica interfaces at 5K for 50ps. We chose to perform simulations at the temperature of 5K because higher temperature would introduce unexpected fluctuations in the number of interfacial bridges, both when the interface is held still and when the surfaces are pulled apart. The above procedure results in a number of amorphous silica interfaces with different numbers of interfacial siloxane bridges and with different applied normal pressures. Figure 3.2.1 shows an example of an interface created through this scheme. An interfacial siloxane (Si-O-Si) bridge is defined using a Si-O cutoff distance of 1.8Å, which was determined based on the position of the first minimum in the Si-O pair distribution function.

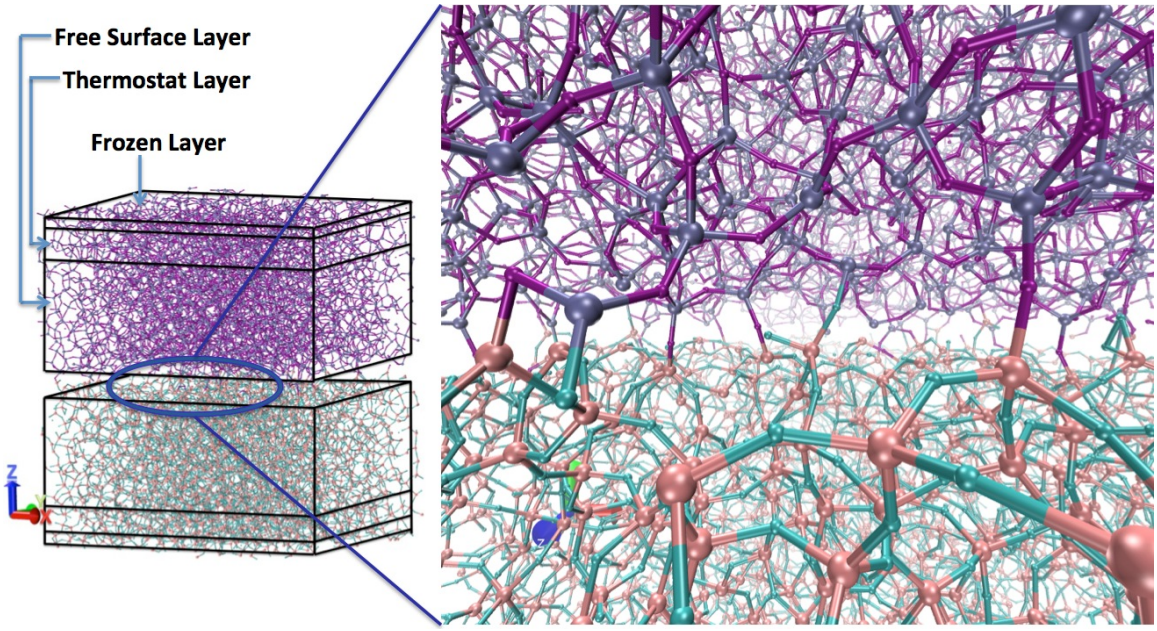

Figure 3.2.1 *A schematic picture of the simulation system with two amorphous samples (left) and atomistic view of the silica/silica interface between these two samples with Si-O-Si bridges (right). Pink and cyan spheres are silicon and oxygen atoms of the bottom silica sample. Metallic blue and purple spheres are Si and O atoms in the top silica sample.*

Sliding simulations are performed by moving laterally the atoms in the frozen layer of the top silica sample. Our goal was to find a sliding velocity that captures the stick-slip phenomenon, which occurs in AFM experiments on silica.[5 16] After a series of velocity tests, we chose 75m/s as the sliding velocity at which a clear stick-slip phenomenon can be observed. During sliding simulations, the temperature is kept at 5K because we want to isolate the effect of the chemistry of the interface (concentration of the interfacial bridges) on friction from the effects of temperature. At higher temperatures, bond breaking could take place due to thermal activations. Friction force is calculated by summing lateral forces on all atoms in each frozen layer and then by averaging it over the two frozen layers. We average the friction forces over multiple sliding directions and over different

equilibration times of prepared interfaces. The numbers over which the results are averaged are provided in the results section.

3.3 Results

3.3.1 Dependence of Static Friction F_s on the Number of Interfacial Bridges

The static friction force F_s can be determined by plotting the lateral friction force F_L as a function of the sliding distance. An example of such a plot is shown in Fig. 3.3.1. Sliding distance is defined as the lateral displacement of the center of mass of the top frozen layer, which is displaced laterally at a constant velocity. Initially, the silica surfaces stick to each other and the friction force increases. The maximum force corresponds to the static friction force F_s. Our simulations reveal that at this point all the interfacial bridges break almost simultaneously and then the interface slips. Correspondingly, the resistance to sliding F_L decreases (see Fig. 3.3.1).

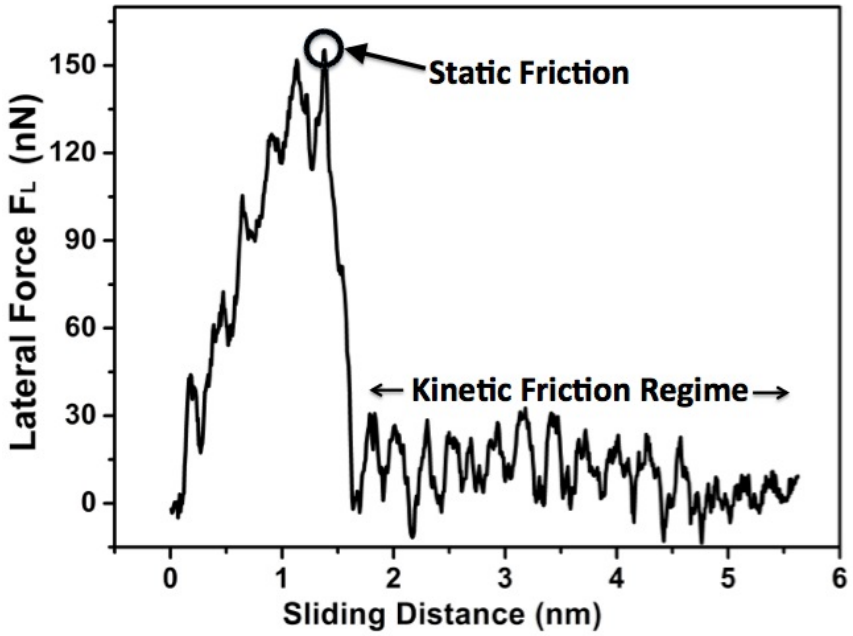

Figure 3.3.1 *A typical lateral relationship between the friction force F_L and the sliding distance measured in MD simulations. Here, the initial number of siloxane bridges across the interface before sliding is 19, which corresponds to a concentration of 0.58 nm^{-2}. The initial normal pressure before sliding is -4.76GPa (adhesive). The maximum of F_L, marked with an open circle corresponds to the static friction force F_s.*

In order to understand the effects of the concentration of siloxane bridges on static friction of amorphous silica, we prepare amorphous silica interface with 3, 6, 11, 14, 19, 23, 27, and 30 siloxane bridges, which corresponds to bridge concentrations of 0.092, 0.184, 0.338, 0.43, 0.58, 0.71, 0.83, 0.92 bridges per nm^2, respectively. Normal pressure P_N is controlled by changing the distance between frozen layers of the top and the bottom silica samples, as described in Section II. By plotting F_L vs. sliding distance for each bridge concentration and for each value of normal pressure, we determine the static friction F_s as a function of P_N. The results are shown in Fig.3.3.2. The first feature of Fig.3.3.2 is that for each interface with a given number of siloxane bridges, F_s increases linearly with P_N. The reported values of F_s for interfaces with 3, 6, 11, and 14 bridges are averaged over 6 sliding simulations where we varied the sliding direction and the interface equilibration time. The values of F_s for interfaces with 19, 23, 27, and 30 bridges are averaged over 8 independent sliding simulations. The error bar corresponds to the 70% confidence interval of the fitted values using student-t distribution. The dashed lines represent a fit of F_s vs P_N for each interface. The parameters of the linear fit for F_s versus P_N relationship are given in Table 3.3.1. The negative values of P_N in Fig. 3.3.2 mean that the adhesive forces dominate the interaction due to stretching of interfacial bridges. We choose the negative P_N regime because higher values of P_N can lead to a gradual disappearance of a distinct static friction regime in our simulations.

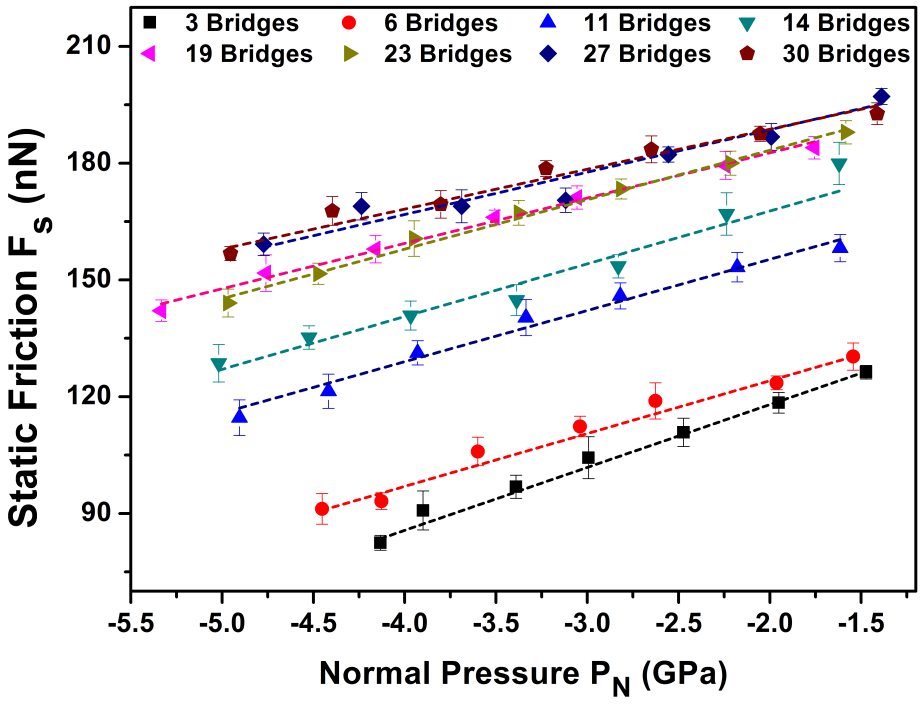

Figure 3.3.2 *The dependence of the static friction F_s on the applied normal pressure P_N. The interfacial area is equal to 32.55nm^2. Symbols correspond to interfaces with different number of interfacial siloxane bridges. Dashed lines represent linear fits.*

Table 3.3.1 *Parameters of a linear fit $y = a + bx$ to the relationship between the static friction force F_s and the normal pressure P_N. σ_a, and σ_b are the standard deviations of a, and b, respectively. R^2 represents the goodness of the fit.*

Number of Bridges	a	σ_a	b	σ_b	R^2
3	150.309	1.318	16.160	0.453	0.995

6	151.271	1.608	13.578	0.521	0.976
11	181.608	2.275	13.154	0.678	0.980
14	194.799	2.784	13.553	0.755	0.939
19	205.965	1.810	11.644	0.494	0.990
23	208.769	1.825	12.716	0.534	0.994
27	210.381	1.372	10.893	0.458	0.947
30	209.239	1.312	10.261	0.372	0.975

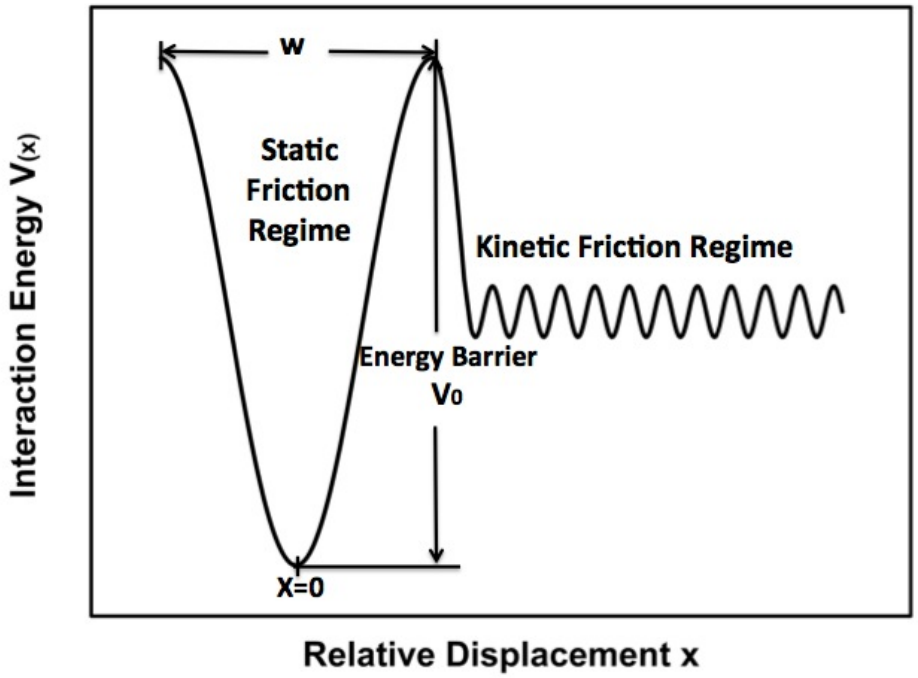

Figure 3.3.3 *Schematic energy landscape V(x) representing the interaction energy between the top and the bottom silica sample. x is the lateral displacement of the lower surface of the top silica sample.*

The linear relationship between F_s and P_N can be understood in light of a one-dimensional Prandlt-Tomlinson model[35]. We define $V(x)$ as the interaction energy between the top and the bottom silica samples, where x is the displacement of the lower surface of the top silica sample along the direction of sliding. The elastic energy stored in the top silica sample can be written as $E_{el}(x) = \frac{1}{2}k(X-x)^2$, where k is the effective spring constant and X is the lateral displacement of the frozen layer of the top silica sample along the direction of sliding (see Section II). If we neglect inertia, the total energy of the top silica sample $E_{tot}(x)$ is equal to the sum of the energy due to interactions with the bottom silica sample $V(x)$ and the elastic energy E_{el} stored in the top silica sample, as shown in the following equation

$$\mathrm{E_{tot}}(x) = \mathrm{V}(x) + \frac{1}{2}k(X - x)^2 \qquad (1)$$

Figure 3.3.3 is a schematic representation of the energy landscape $\mathrm{V}(x)$ of the top silica sample. The $\mathrm{V}(x)$ landscape corresponds to the data shown in Fig. 3.3.1, where there is a clear transition from static to kinetic friction. $\mathrm{V}(x)$ reaches a minimum value when $x \approx 0$, which corresponds to the initial state of the interface before frictional sliding. In this state, the interface is stable and the interfacial bridges are not strained or broken due to frictional sliding. When x increases, the interfacial bridges that connect the surfaces of the top and the bottom silica samples are increasingly strained, which in turn leads to an increase of $\mathrm{V}(x)$. Eventually, the interfacial bonds break, which corresponds to the maximum energy barrier $\mathrm{V_0}$. In our simulations, we observe all bonds breaking during the slick-slip transition. After the stick-slip transition, the system enters the regime of kinetic friction. In the kinetic friction regime, bond-forming and bond-breaking reaction also happen during frictional sliding, which leads to the corrugated $\mathrm{V(x)}$ in this regime. As a result, the $\mathrm{V}(x)$ minima in the kinetic regime are not as low as the energy of the initial state $\mathrm{V}(0)$ and the maxima of $\mathrm{V}(x)$ in the kinetic regime are not as high as the energy $\mathrm{V_0}$ corresponding to the initial breaking of bonds.

In this paper we are primarily interested in the static regime of friction. We define w as the peak-to-peak width of the potential energy well in the static friction regime (see Fig. 3.3.3). We approximate $\mathrm{V}(x)$ in the interval $-\frac{w}{2} < x < \frac{w}{2}$ using the following relation[36]

$$\mathrm{V}(x) = -\frac{V_0}{2}\cos\left(\frac{2\pi}{w}x\right). \qquad (2)$$

In this static friction regime, we can assume the lateral force $\mathrm{F_L}$ to be linear with $(X - x)$, which represents the lateral deformation of the top silica sample due to shearing. $\mathrm{F_L}$ can therefore be written as

$$F_L = k(X - x). \quad (3)$$

In a quasi-static motion, $E_{tot}(x)$ of the top silica sample remains in a local minimum. The two conditions for determining a local minimum are

$$E_{tot}\,'(x) = V'(x) - k(X - x) = 0 \quad (4)$$

$$E_{tot}\,''(x) > 0. \quad (5)$$

$E_{tot}\,'(x)$ and $E_{tot}\,''(x)$ are the first and the second derivatives of $E_{tot}(x)$ with respect to x, respectively. [35] Combing equations (2), (3) and (4), we obtain

$$F_L = \frac{\pi V_0}{w} \sin\left(\frac{2\pi x}{w}\right) \quad (6)$$

in the interval $-\frac{w}{2} < x < \frac{w}{2}$. The static friction F_s can be measured by determining the maximum absolute value of the lateral force $|F_L|_{max}$ in the entire sliding process.[36] Based on Eq. (6), the static friction force is equal to $|F_L|_{max}$ when $x = w/4$, that is

$$F_s = |F_L|_{max} = \frac{\pi V_0}{w}. \quad (7)$$

Equation (7) satisfies both conditions given by Eq. (4) and Eq. (5). Now, according to the Eyring model,[37] the energy barrier V_0 for breaking of interfacial siloxane bridges can be reduced by the mechanical work done on the system

$$V_0 = \Delta U_{act} + \sigma_n \Delta V_{act} \quad (8)$$

where ΔU_{act} is the stress-free energy barrier for breaking of all existing interfacial bonds, σ_n is the applied normal stress, and ΔV_{act} is the activation volume. ΔV_{act} is assumed to be constant in our system, which is justified based on published density functional theory calculations for siloxane bridge formation at silica/silica interface (see Supplemental Information in Ref [30]) and by experimental measurements of sliding friction at other interfaces[38 39] . As shown by Eq. (8), σ_n

increases the energy barrier. One should keep in mind that our simulations are carried out in the adhesive regime, which means that σ_n is negative. By plugging in Eq. (8) into Eq. (7), we obtain

$$F_s = \frac{\pi \Delta U_{act}}{w} + \frac{\pi \sigma_n \Delta V_{act}}{w} = \frac{\pi \Delta U_{act}}{w} + \frac{\pi \Delta V_{act}}{w} P_N \qquad (9)$$

P_N is the applied normal pressure, which equals to the normal stress σ_n. As shown by Eq. (9), the static friction F_s depends linearly on the applied normal pressure P_N, which is consistent with the linear relationship observed in our simulations and shown in Fig. 3.3.2.

An important question that remains to be answered is the dependence of the static friction force on bridges concentration at silica interfaces. As shown in Fig. 3.3.2, the increase in both, the applied normal pressure and the number of interfacial bridges, leads to an increase in the static friction force. In order to isolate the effects of the number of siloxane bridges from the effect of the applied normal pressure, in Fig. 3.3.4 we plot the static friction force F_s as a function of the number of bridges *n* at a constant normal pressure. Each data point corresponds to the static friction force predicted by the linear fits in Fig. 3.3.2 for a given value of the normal pressure. Figure 3.3.4 shows that F_s increases with *n* with a decreasing slope. Although for low values of *n*, this relationship can be approximated as a linear function, significant deviations from the linear behavior are observed for intermediate and large values of *n*. The error bar in Fig. 3.3.4 corresponds to the 70% confidence interval of each data point using error propagation.

To understand why the derivative of F_s with respect to *n* decreases in the regime of large bridge concentration, it is useful to consider how the value of *n* affects the energy barrier V_0 for breaking interfacial bridges during sliding. As reported in Ref. [30], increasing *n* leads to an increase of the reaction energy for formation of a new siloxane bridge across the interface. We define $\Delta E_{form,i}$ to be the energy to form a siloxane bridge *i* across the interface. If we assume that the bridge breaking process is the opposite process to bridge formation, then the reaction energy of breaking a bridge *i*

is· $\Delta\mathrm{Ebreak,i} = -\Delta\mathrm{Eform,i}$. Based on the Bronsted-Evans-Polanyi (BEP) relation,[37] we assume a linear relationship between reaction energy and reaction energy barriers.

$$\mathrm{V}_{0,\mathrm{break,i}} = \alpha \cdot \Delta\mathrm{Ebreak,i} + g = -\alpha \cdot \Delta\mathrm{Eform,i} + g \qquad (10)$$

In the above expression, $\mathrm{V}_{0,\mathrm{break,i}}$ is the energy barrier for breaking the bridge i, and α and g are constant parameters in the BEP relation. The factor α is between 0 and 1, and it characterizes the position of the transition state along the reaction coordinate. We also assume that all n interfacial bridges break simultaneously (which is justified by observations from our MD simulations) and that all bridges have the same energy barrier for bond breaking. The latter supposition simplifies the mathematical derivation without changing the resulting qualitative trends. We then obtain

$$\mathrm{V}_0 = \sum_{i=1}^{n} \mathrm{V}_{0,\mathrm{break,i}} = n \cdot \mathrm{V}_{0,\mathrm{break,i}} \qquad (11)$$

Plugging in Eq. (10) and Eq. (11) into Eq. (7), we get

$$F_s = \frac{\pi V_0}{w} = \frac{\pi \cdot n \cdot \mathrm{V}_{0,\mathrm{break,i}}}{w} = \frac{-\alpha\pi \cdot \Delta\mathrm{Eform,i} + g\pi}{w} \cdot n \qquad (12)$$

From both, Eq. (12) and from Ref. [30], $\Delta\mathrm{Eform,i}$ increases with n and therefore $\frac{-\alpha\pi \cdot \Delta\mathrm{Eform,i} + g\pi}{w}$ decreases with n. This is consistent with the trend observed in Fig. 3.3.4 and shows that the force needed to break a siloxane bridge becomes smaller when the bridge concentration is larger.

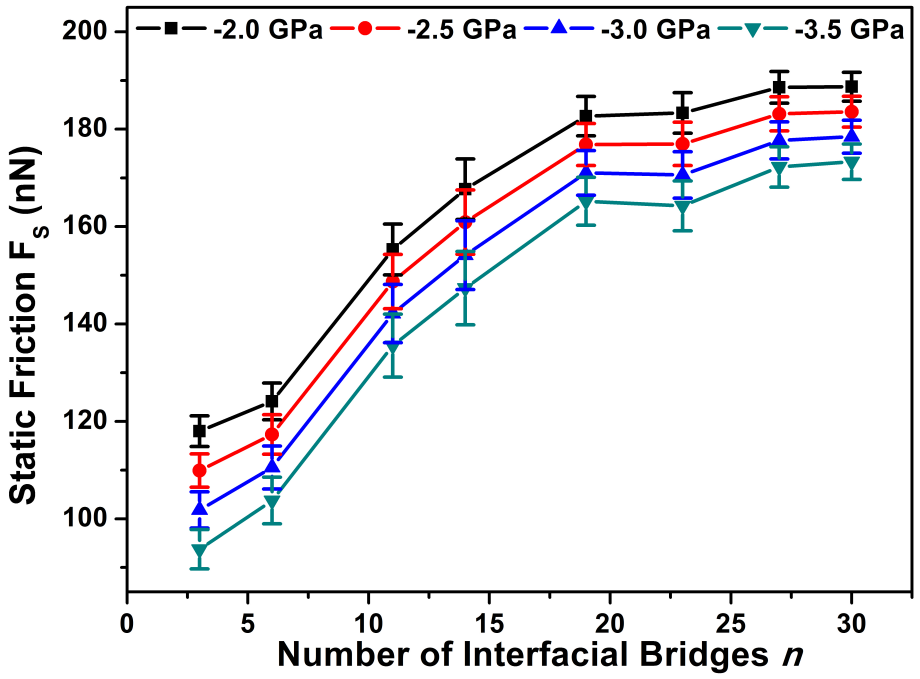

Figure 3.3.4 *The dependence of the static friction F_s on the number of interfacial bridges n. The interfacial area is equal to 32.55nm^2. Symbols (and colors online) correspond to different applied normal pressures. The lines connecting data points are added to guide the eye.*

3.1. Atomic-level wear mechanisms

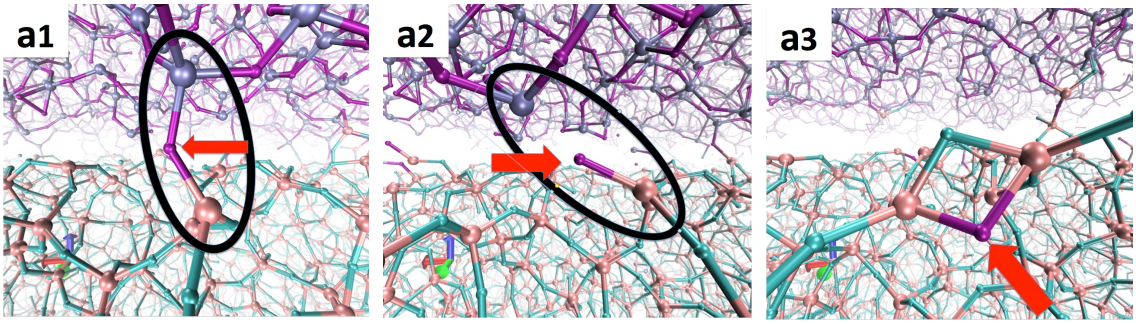

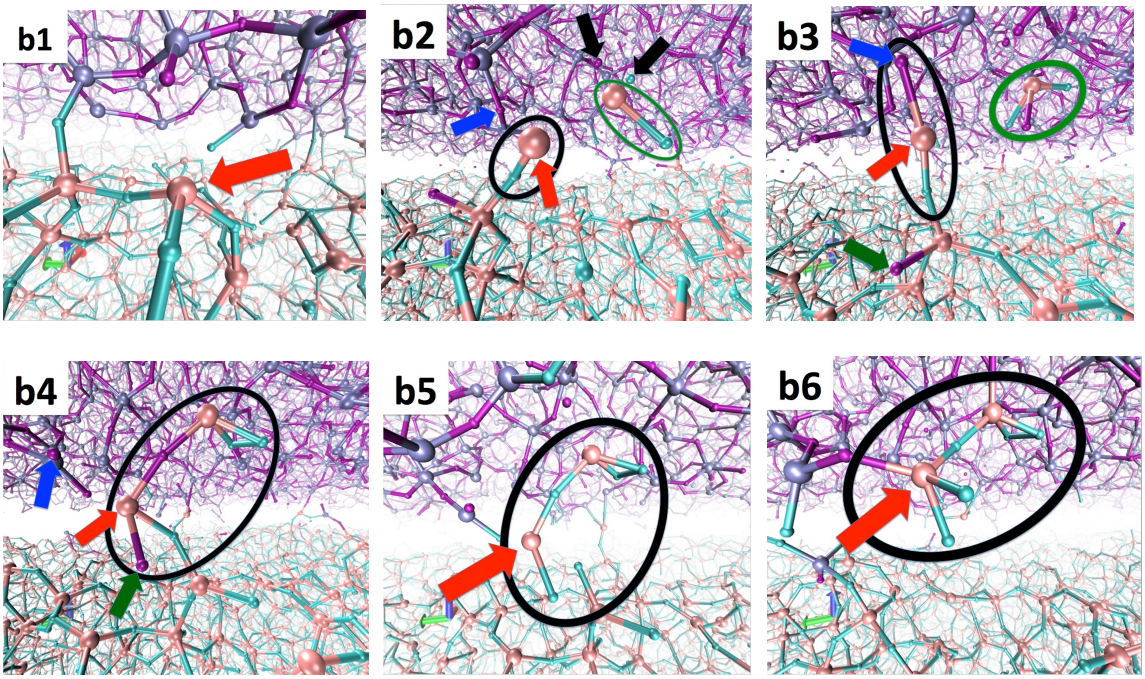

Figure 3.3.5 *Atomic scale wear mechanisms of silica/silica interface. Panels a1- a3 show a wear mechanism by transfer of an individual oxygen atom accompanied by breaking of one Si-O bond in the interfacial siloxane bridge. Panels b1-b6 show a wear mechanism by transfer of an atomic cluster. In all panels, pink and cyan spheres, respectively, are Si and O atoms of the bottom silica sample. Metallic blue and purple spheres, respectively, are Si and O atoms of the top silica sample. Red arrow in a1- a3 marks O atom that is at the center of an interfacial siloxane bridge. Red arrow in b1-b6 marks Si atom that is being transferred from the bottom to the top silica samples. Blue, black and green arrows in b2-b4 each marks a specified oxygen atom involved in cluster formation and transfer. Black and green circles show clusters participating in the material transfer during wear, as explained in detail in the main text.*

We investigate the atomic-level mechanisms of wear that took place in our MD simulations. Two most common mechanisms are shown in Figs. 3.3.5(a1-a3) and Figs. 3.3.5(b1-b6). Figures 3.3.5(a1-a3) show wear by transfer of an individual atom. By shearing the silica/silica interface, the pre-

existing interfacial Si-O-Si bridge (Fig. 3.3.5a1) becomes stretched and broken through the rupture of one of the Si-O bonds of the siloxane bridge (Fig. 3.3.5a2). As a result, the oxygen atom that used to be bonded to the top silica surface is pulled to the bottom silica surface by the remaining Si-O bond of the siloxane. Subsequently, the transferred oxygen atom forms a surface siloxane bridge on the bottom silica surface and becomes chemically non-reactive (Fig. 3.3.5a3). This wear mechanism by individual oxygen atom transfer is most common because it involves breaking of only one Si-O bond, as opposed to mechanisms that involve breaking of multiple bonds, such as pulling out a Si atom or the entire cluster of atoms from the silica surface.

However, when shearing two surfaces past each other, not all bond breakings occur in the interfacial siloxanes and some surface Si-O bonds will also be broken, which eventually will build up damage and lead to a transfer of the entire atomic cluster. Figures 3.3.5(b1-b6) illustrate how an atomic cluster is nucleated, how it grows, and finally how it is transferred to the counter surface. The Si atom marked by the red arrow is initially bonded to three O atoms in the bottom surface (Fig. 3.3.5b1). Due to shearing of the surfaces, local stress near the silicon atom accumulates and leads to breaking of two of the three Si-O bonds that hold the Si atom to the bottom silica surface (see Fig. 3.3.5b2). The silicon atom becomes highly reactive as it now participates in only one covalent bond. Moreover, without the geometric constraint of the tetrahedron that is typical of silica structure, the Si atom in question can move closer to the top silica surface than before, which makes it easier for this atom to react with oxygen atoms from the top silica surface. In Fig. 3.3.5b3, the Si atom has attracted an O atom (marked by blue arrow in Fig. 3.3.5b2 and Fig. 3.3.5b3) and is pulling it out from the top silica surface. This protruding cluster (marked by a black circle) consists of a linear chain of three Si-O bonds and therefore is chemically highly reactive. The group of atoms circled in green in Fig. 3.3.5b3 is another interfacial SiO_3 cluster with part of tetrahedron structure, formed through bonding reactions from two single oxygen atoms (marked by black arrows in Fig. 3.3.5b2) and a Si-

O cluster (marked by green circle in Fig. 3.3.5b2) during the sliding process. When these two clusters get close enough, they react and bond, forming one bigger cluster that consists of two Si and four O atoms (Fig. 3.3.5b4). This Si_2O_4 cluster also shows imperfect tetrahedron structure (i.e., one atom is missing from the tetrahedron) and is connected with the bottom silica sample with only one Si-O bond. In Fig.3.3.5b5, the newly formed bigger cluster leaves the bottom silica surface by breaking the remaining Si-O bond that holds it to the bottom silica surface and there are no covalent bonds between this cluster and the two silica surfaces. Finally, the cluster is incorporated into the top silica surface by forming new Si-O bonds (see Fig. 3.3.5b6).

Although the details of the transfer vary between different wear events, there are some general features that are characteristic of such transfers, as observed in our simulations. We find that Si atoms become reactive due to breaking of surface Si-O bonds. These reactive silicon atoms have a strong tendency either to bond to oxygen atoms from the opposite surface or to attract and bond interfacial atomic clusters. If an atomic cluster breaks off from a surface, it becomes and interfacial debris particle, which can slide or roll in the interfacial space. Interfacial clusters are highly reactive and they can be reabsorbed by one of the surfaces. In the case where the cluster is absorbed by the counter-surface (instead of the original surface from which it was removed), it becomes a transferred cluster. The clusters are nucleated and dissolved continually during the sliding process. They play an important role in friction and the wear of silica/silica interface because they can form more Si-O bonds across the interface than a single siloxane bridge. These conclusions are based on the analysis of images from approximately 100 sliding simulations.

We can quantify contributions of the above mechanisms to wear by comparing the atomic structure of the interface before sliding with the structure after 50ps of sliding. Specifically, we identify atoms that belonged to one of the surfaces before sliding and were transferred during sliding to the opposite surface. This analysis was performed for 56 sliding simulations and below we report

the average values. Not surprisingly, we found that the total number of transferred atoms (individually or as part of a cluster) increases significantly with the number of interfacial bridges formed before sliding. This number changes from $(46 \pm 2)\times10^{-2}$ atoms per nm^2 for the case $n = 3$ interfacial bridges to $(138 \pm 4) \times10^{-2}$ atoms per nm^2 for the case of $n = 30$, where the uncertainty corresponds to a standard deviation from this average. In Table 3.3.2 we also provide information about the percentage of events in which atoms were transferred individually or in a cluster of size S. Although many more simulations would be needed to obtain more quantitative trends (which is beyond the scope of this paper), data in Table 3.3.2 has a number of qualitative trends. These trends are also shown in Fig. 3.3.6. Specifically, the majority of wear transfer events involve individual atoms (S = 1). In addition, there are non-negligible contributions to wear transfer from clusters of up to size four. For these clusters the percentage of events generally decreases with an increasing size of the cluster. Although we do observe events involving cluster of size S>4, the number of these events is quite small with no clear trend with the cluster size. We also find that when the number of initial interfacial bridges increase, the percentage of transfers involving a single atom generally decreases and the total contributions to wear from clusters (S>1) increases. The total number of transfer events $N_{transfer}$ is also found to increase with the initial number of interfacial bridges, as is shown in Table 3.3.2.

Table 3.3.2 *Percentage of transfer events underlying wear that involve a cluster of size S. The reported values correspond to averages over 56 simulations and the uncertainty corresponds to a standard deviation from this average.* $N_{transfer}$ *represents the total number of transfer events for the interface size of* $32.55nm^2$.

Number of	S = 1	S = 2	S = 3	S = 4	S = 5	S = 6	S ≥7	$N_{transfer}$

interfacial bridges								
3	83.8 ±6.0	8.6 ±0.8	2.9 ±0.4	1.9 ±0.4	2.9 ±0.8	0.0 ±0.0	0.0 ±0.0	17.5±0 .25
6	82.1 ±5.2	10.3 ±1.8	4.3 ±0.7	0.9 ±0.3	0.9 ±0.3	0.9 ±0.3	0.9 ±0.3	19.5±0 .21
11	73.1 ±5.7	10.3 ±1.4	9.5 ±0.9	4.3 ±0.5	0.9 ±0.2	0.9 ±0.4	0.9 ±0.4	19.4±0 .49
14	75.5 ±5.5	12.2 ±1.1	10.7 ±0.9	1.5 ±0.4	0.0 ±0.0	0.0 ±0.0	0.0 ±0.0	21.8±0 .42
19	69.6 ±2.4	12.1 ±1.4	8.2 ±1.7	6.3 ±1.1	1.5 ±0.6	1.5 ±0.7	1.0 ±0.5	25.9±1 .20
23	68.2 ±3.1	13.6 ±1.5	8.0 ±1.2	5.3 ±0.9	3.4 ±1.6	1.1 ±0.5	0.4 ±0.4	33.0±0 .63
27	73.6 ±1.6	10.0 ±0.7	7.8 ±0.8	5.0 ±1.2	1.2 ±0.8	0.0 ±0.0	2.4 ±0.8	40.1±1 .76
30	73.2 ±0.9	11.3 ±1.2	7.9 ±1.2	4.5 ±1.2	1.4 ±0.4	0.6 ±0.3	1.1 ±0.8	44.4±2 .42

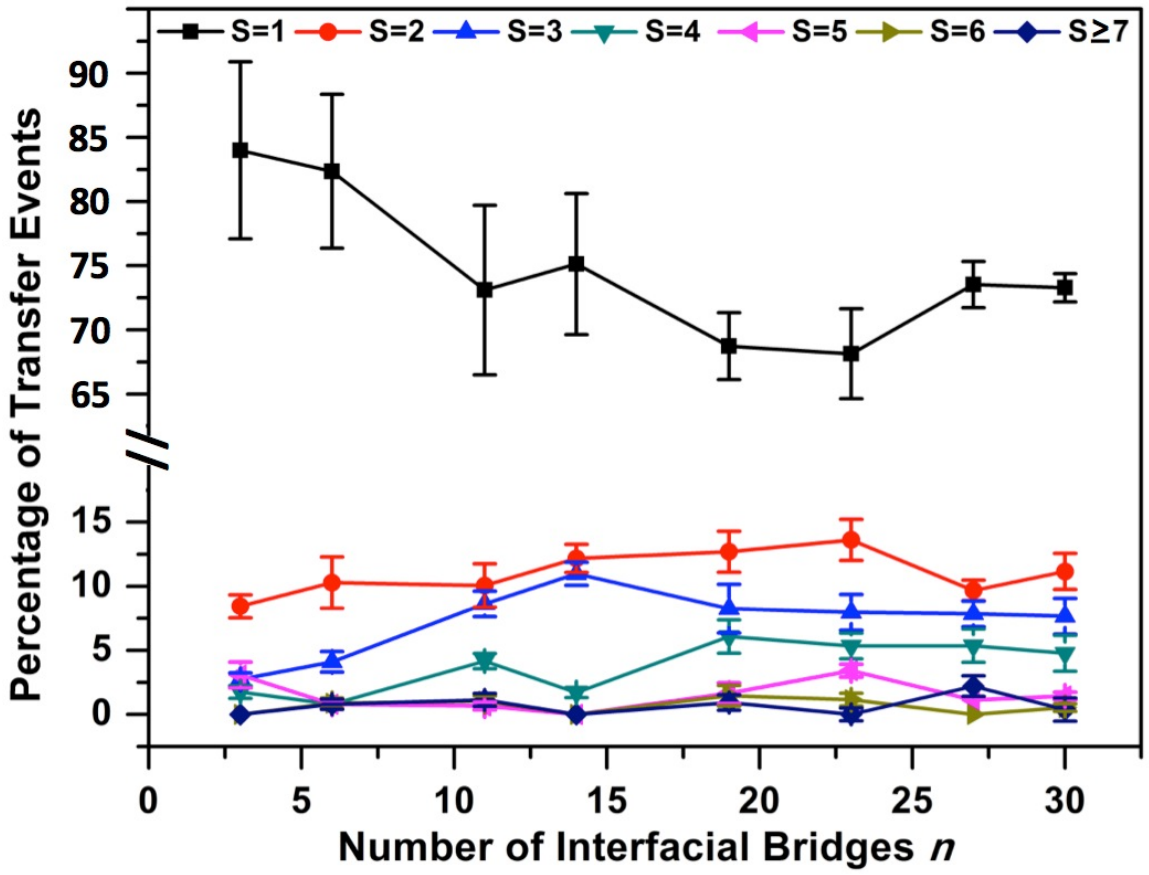

Figure 3.3.6 *Percentage of wear events in which atoms were transferred individually (S=1) or in a cluster of size S (S≥2). Error bars correspond to 70% confidence interval.*

3.4 Conclusions

We find that for two flat silica surfaces with the same siloxane bridge concentration, the static friction between them increases linearly with the normal pressure (and therefore also with load). We also find that the static friction force increases nonlinearly with concentration of interfacial siloxane bridges, which can be explained by interactions among neighboring bridges. By analyzing atomic scale wear mechanisms of silica/silica interface, we demonstrated two dominant wear mechanism which are individual-oxygen-atom transfer accompanied by breaking one of Si-O bonds in the interfacial siloxane bridge, and atomic-cluster transfer initialized by ruptures of surface siloxane

bridges. Small clusters are continually formed and dissolved at the sliding interface, which play an important role in wear of silica/silica interface.

Reference

1 Lasky, J.B. : Wafer bonding for silicon-on-insulator technologies. Appl. Phys. Lett. 48, 78-80 (1985).

2 Ventosa, C., Rieutord, F., Libralesso, L., Morales, C., Fournel, F., Moriceau, H.: Hydrophilic low-temperature direct wafer bonding. J. Appl. Phys. (2008).: 10.1063/1.3040701

3 E. Taran, E., Donose, B.C., Vakarelski, I.U., Higashitani, K.: pH dependence of friction forces between silica surfaces in solutions. J. Colloid Interface Sci. 297, 199-203 (2006).

4 Scholz, C.: Earthquakes and friction laws. Nature 391, 37-42 (1998).

5 Li, Q., Tullis, T.E., Goldsby, D., Carpick, R.W.: Frictional ageing from interfacial bonding and the origins of rate and state friction. Nature 480, 233-236 (2011).

6 Chandross, M., Webb III, E.B., Stevens, M.J., Grest, G.S.: Systematic Study of the Effect of Disorder on Nanotribology of Self-Assembled Monolayers. Phys. Rev. Lett. (2004). doi: 10.1103/PhysRevLett.93.166103

7 Chandross, M., Lorenz, C.D., Stevens, M.J., Grest, G.S.: Simulations of Nanotribology with Realistic Probe Tip Models. Langmuir 24, 1240-1246 (2008).

8 Toro, G.D., Goldsby, D.L., Tullis, T.E.: Friction falls towards zero in quartz rock as slip velocity approaches seismic rates. Nature 427, 436-439 (2004).

9 Xu, J., Kato, K.: Formation of tribochemical layer of ceramics sliding in water and its role for low friction. Wear 245, 61-75 (2000).

10 Heim, L., Blum, J., Preuss, M., Butt, H.: Adhesion and friction forces between spherical micrometer-sized particles. Phys. Rev. Lett. 16, 3328-3331 (1999).

11 Chen, J., Ratera, I., Park, J., Salmeron, M.: Velocity dependence of friction and hydrogen bonding effects. (2006). doi: 10.1103/PhysRevLett.96.236102

12 Subhalakshmi, K., Devaprakasam, D., Math, S., Biswas, S.K.: Use of Eyring equation to explore the frictional responses of a –CF3 and a –CH3 terminated monolayers self-assembled on silicon substrate. Tribol. Lett. 32, 1-11 (2008).

13 Taran, E., Kanda, Y., Vakarelski, I.U., Higashitani, K.: Nonlinear friction characteristics between silica surfaces in high pH solution. J. Colloid Interface Sci. 307, 425-432 (2007).

14 Zhuravlev, L.T.: The surface chemistry of amorphous silica. Zhuravlev model. Colloids Surfaces A Physicochem. Eng. Asp. 173, 1-38 (2000).

15 Plößl, A., Kräuter, G.: Wafer direct bonding: tailoring adhesion between brittle materials. Mater. Sci. Eng. R 25, 1-88 (1999).

16 Vigil, G., Xu, Z., Steinberg, S.,Israelachvili,J.: Interactions of silica surfaces. J. Colloid Interface Sci. (1994). doi: 10.1006/jcis.1994.1242

17 Riedo, E., Lévy, F., Brune, H.: Kinetics of capillary condensation in nanoscopic sliding friction. Phys. Rev. Lett. (2002). doi: 10.1103/PhysRevLett.88.185505

18 Szoszkiewicz, R. Riedo, E.: Nucleation time of nanoscale water bridges. Phys. Rev. Lett. (2005). doi: http://dx.doi.org/10.1103/PhysRevLett.95.135502

19 Adler, J.J., Rabinovich, Y.I., Moudgil, B.M.: Origins of the non-DLVO force between glass surfaces in aqueous solution. J. Colloid Interface Sci. 237, 249-258 (2001).

20 Bhaskaran, H., Gotsmann, B., Sebastian, A., Drechsler, U., Lantz, M.A., Despont, M., Jaroenapibal, P., Carpick, R.W., Chen, Y., Sridharan, K.: Ultralow nanoscale wear through atom-by-atom attrition in silicon-containing diamond-like carbon. Nat. Nanotechnol. 5, 181-185 (2010).

21 Archard, J.F.: Contact and rubbing of flat surfaces. J. Appl. Phys. 24, 981-988 (1953).

22 Bocquet, L., Charlaix, E., Ciliberto, S., Crassous, J.: Moisture-induced ageing in granular media and the kinetics of capillary condensation. Nature 396, 735-737 (1998).

23 Dieterich, J.H.: Time-dependent friction in rocks. J. Geophys. Res. 77, 3690-3697 (1972).

24 Ruina, A.: Slip instability and state variable friction laws. J. Geophys. Res. 88, 10359-10370 (1983).

25 Dieterich, J.: Modeling of rock friction: 1. Experimental results and constitutive equations. J. Geophys. Res. 84, 2161-2168 (1979).

26 Capozza, R., Barel, I., Urbakh, M.: Probing and tuning frictional aging at the nanoscale. Sci. Rep. (2013). doi: 10.1038/srep01896

27 Beeler, N.M.: Review of the physical basis of laboratory-derived relations for brittle failure and their implications for earthquake occurrence and earthquake nucleation. Pure Appl. Geophys. 161, 1853-1876 (2004).

28 Nakatani, M., Scholz, C.: Frictional healing of quartz gouge under hydrothermal conditions: 2. Quantitative interpretation with a physical model. J. Geophys. Res. (2004). doi: 10.1029/2003JB002938

29 Rice, J.R., Lapusta, N., Ranjith, K.: Rate and state dependent friction and the stability of sliding between elastically deformable solids. J. Mech. Phys. Solids 49, 1865-1898 (2001).

30 Liu, Y., Szlufarska, I.: Chemical origins of frictional aging. Phys. Rev. Lett. (2012). doi: http://dx.doi.org/10.1103/PhysRevLett.109.186102

31 Mo, Y., Turner, K.T., Szlufarska, I.: Friction laws at the nanoscale. Nature 457, 1116-1119 (2009).

32 Mo, Y., Turner, K.T., Szlufarska, I.: Origin of the isotope effect on solid friction. Phys. Rev. B (2009). doi: http://dx.doi.org/10.1103/PhysRevB.80.155438

33 Fogarty, J.C., Aktulga, H.M., Grama, A.Y., van Duin, A.C.T., Pandit, S.A.: A reactive molecular dynamics simulation of the silica-water interface. J. Chem. Phys. (2010). doi:10.1063/1.3407433

34 Plimpton, S.: Fast parallel algorithms for short-range molecular dynamics. J. Comput. Phys. (1995). doi: 10.1006/jcph.1995.1039

35 Hölscher, H., Schirmeisen, A., Schwarz, U.D.: Principles of atomic friction: from sticking atoms to superlubric sliding. Philos. Trans. A. Math. Phys. Eng. Sci. 366, 1383-1404 (2008).

36 Socoliuc, A., Bennewitz, R., Gnecco, E., Meyer, E.: Transition from stick-slip to continuous sliding in atomic friction: entering a new regime of ultralow friction. Phys. Rev. Lett. (2004). doi: http://dx.doi.org/10.1103/PhysRevLett.92.134301

37 Evans, M., Polanyi, M.: Some applications of the transition state method to the calculation of reaction velocities, especially in solution. Trans. Faraday Soc. 31, 875-894 (1935).

38 Riedo, E., Gnecco, E.,Bennewitz, R., Meyer, E.,Brune, H.:Interaction Potential and Hopping Dynamics Governing Sliding Friction. Phys. Rev. Lett. (2003). doi: 10.1103/PhysRevLett.91.084502

39 Furlong, O.J., Manzi, S.J., Pereyra, V.D., Bustos, V., Tysoe, W.T.:Monte Carlo simulations for Tomlinson sliding models for non-sinusoidal periodic potentials. Tribol. Lett. 39, 177-180 (2010).

Chapter 4 How grain size controls friction and wear in nanocrystalline metals?

4.1 Introduction

Grain refinement to the nanometer regime has been shown to have important non-monotonic effects on mechanical properties of metals. Specifically, a number of studies reported existence of an optimum grain size that maximizes strength and hardness of metallic systems.[1,2] This maximum strength corresponds to the grain diameter for which mechanisms of deformation transition from being dominated by intragranular dislocation plasticity to grain boundary (GB) sliding. In addition to this intrinsic grain size effect, mechanical properties can depend on the dimensions of the specimen – a so-called extrinsic size effect. For instance, mechanical strength of metallic nanopillars can be significantly lower[3] or higher[4] than the strength of the corresponding bulk samples.

Grain refinement has been also shown to be a highly promising path for improving friction and wear resistance of metals.[5,6] However, despite these promising reports, at present the effects of grain size on wear and friction of nc metals are far from understood. For instance, it is unknown whether there is specific grain size that minimizes friction and wear or how the underlying mechanisms depend on the details of the microstructure. Molecular dynamics (MD) simulations have greatly contributed to discoveries of size effects in plasticity and of deformation mechanisms in nc metals during uniform shear, compression and during nanoindentation,[1,2,7-10] but MD simulations of wear of nc materials have only been reported in the last few years[11-13]. For example, the authors of Ref. [13] performed MD simulations of tip sliding on nc copper and discovered formation of folds in the worn material. This finding was supported by observations from atomic force microscopy (AFM)

experiments. However, the grain size effect on friction and wear and on the underlying mechanisms of deformation were not explored in that study.

4.2 Methods

To address the question of size effects in friction and wear of face-centered cubic (fcc) metals, we perform a series of large-scale MD simulations of frictional sliding between a rigid parabolic tip and nc Cu (Fig. 4.2.1a) with grain diameter *d* ranging from 5 to 50 nm. Our simulation setup mimics AFM experiments of single-asperity friction. MD simulations were conducted with the LAMMPS software[14] using the embedded atoms method force field[15]. Voronoi algorithm was used to generate samples with grain diameter between 5 nm and 50 nm, corresponding to 26-76 million atoms in each sample. Grain sizes distribution is close to the Gaussian distribution (Fig. 4.2.1b), which is consistent with typical grain size distribution in nc copper.[16] Dimensions of samples with different grain diameters are listed in Table 4.2.1. Before any mechanical testing each nc sample is relaxed at 300K for 1ns.

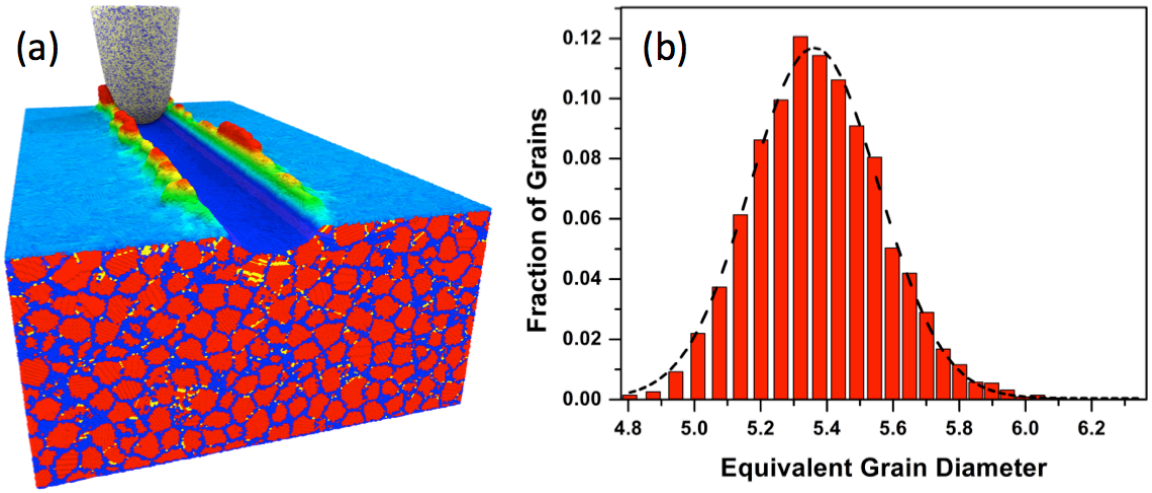

Figure 4.2.1 *(a) Tip sliding over nc-Cu with d=5nm. (b) Grain size distribution of the sample with d=5nm. Equivalent grain diameter is determined by calculating total number of atoms in a given grain and then calculating the diameter assuming the grain is spherical. Black dashed line shows the Gaussian fitting with* R^2*= 0.995.*

Table 4.2.1 *Sample dimensions and sizes for nc-Cu with different average grain diameters d.*

Grain Diameter *d* (nm)	Length (nm)	Width (nm)	Height (nm)	Number of Atoms
5.0	168	42	42	2,4409,623
15.0	170	42	42	2,537,0194
20.8	170	42	42	25,506,752
30.0	170	43	43	25,611,232
40.0	170	57	57	45,640,021
50.0	177	71	71	74,407,958

In order to test whether properties are converged with respect to substrate dimensions, we performed additional simulations on samples where we doubled the substrate width. We choose to test the effects of width because the tip-boundary distance along the width direction is much smaller than those along the depth and length directions (see Table 4.2.1 in main text). Our test was performed on a sample with the average grain diameter d = 5nm for a range of normal loads. The results for the two different widths show a good agreement with each other (Fig. 4.2.2), which means that the tip induced plastic deformation is highly localized in the nanocrystalline samples and is not influenced by the substrate size.

In contrast to the above results for nanocrystalline samples, friction and stresses measured for single crystal samples show a significant size dependence (not shown here). This is because in a single crystal dislocations can travel all the way to the rigid boundary (without being obstructed by grain boundaries), they become reflected from the boundary and then interact with the newly generated dislocations. For this reason, in this paper we do not report friction coefficients or wear data for single crystal samples.

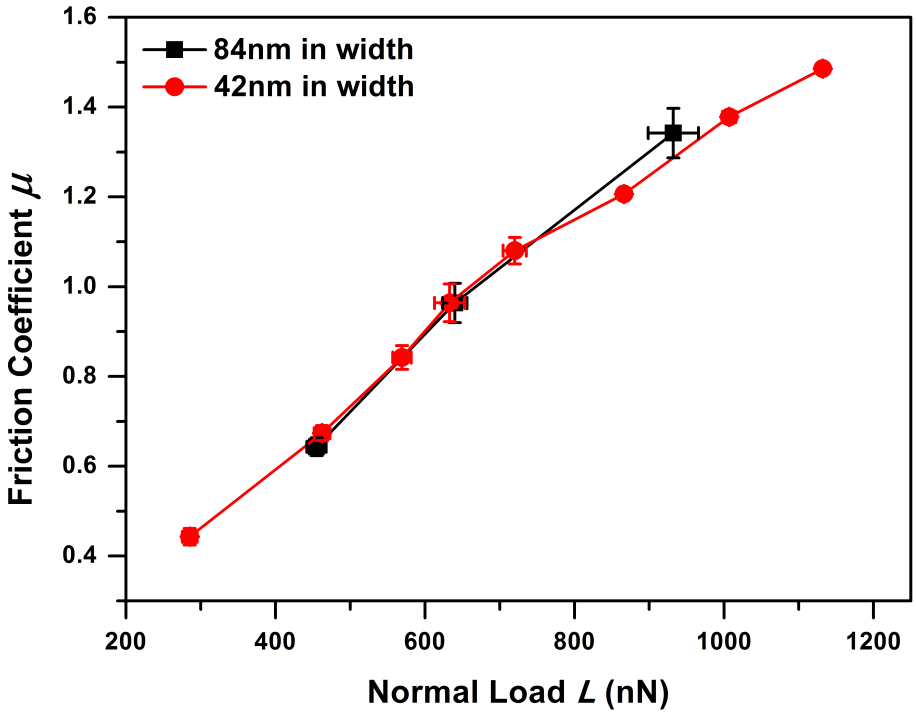

Figure 4.2.2 *Effect of sample's width on the measured friction coefficient μ. μ is plotted as a function of normal load L for samples with width of 84 nm (black) and 42 nm (red).*

In order to test the mechanical properties of the samples, uniaxial tension and compression tests are performed at 300K for true strains up to 0.14 and with a deformation rate of $5\times10^{8}\mathrm{s}^{-1}$. Flow stress is defined as the average stresses in the true strain interval between 0.11 and 0.14, where the stress fluctuates around an approximately constant value. Dependence of flow stresses on grain diameter is shown in Fig. 4.2.3a and it exhibits a maximum between 10 nm and 15 nm. We

confirmed that the presence of maximum is the result of transition from regime dominated by dislocation plasticity (large grain size) to regime dominated by GB sliding (small grain size), as shown in Figs. 4.2.3b-c.

It has been reported in literature that the transition from Hall-Petch relation to inverse Hall-Petch relation can be affected by thermal annealing of samples and relaxation of grain boundaries in MD simulations.[17] To verify that our results are not affected by thermal annealing and that our grain boundaries are relaxed, we have further annealed the nc-Cu samples at 1000K for 1 ns. The samples were then cooled down to room temperature and relaxed for another 1ns. Uniaxial tests on the samples annealed at 300K and at 1000K are shown in Fig. 4.2.3a. No significant difference was found in mechanical properties between the two types of samples, except for the sample with 5 nm grain diameter. The reason underlying the change in strength of the 5 nm sample is the grain growth, which is indicated by the significant decrease in fraction of GBs to atoms in crystalline grains (Fig. 4.2.3d).

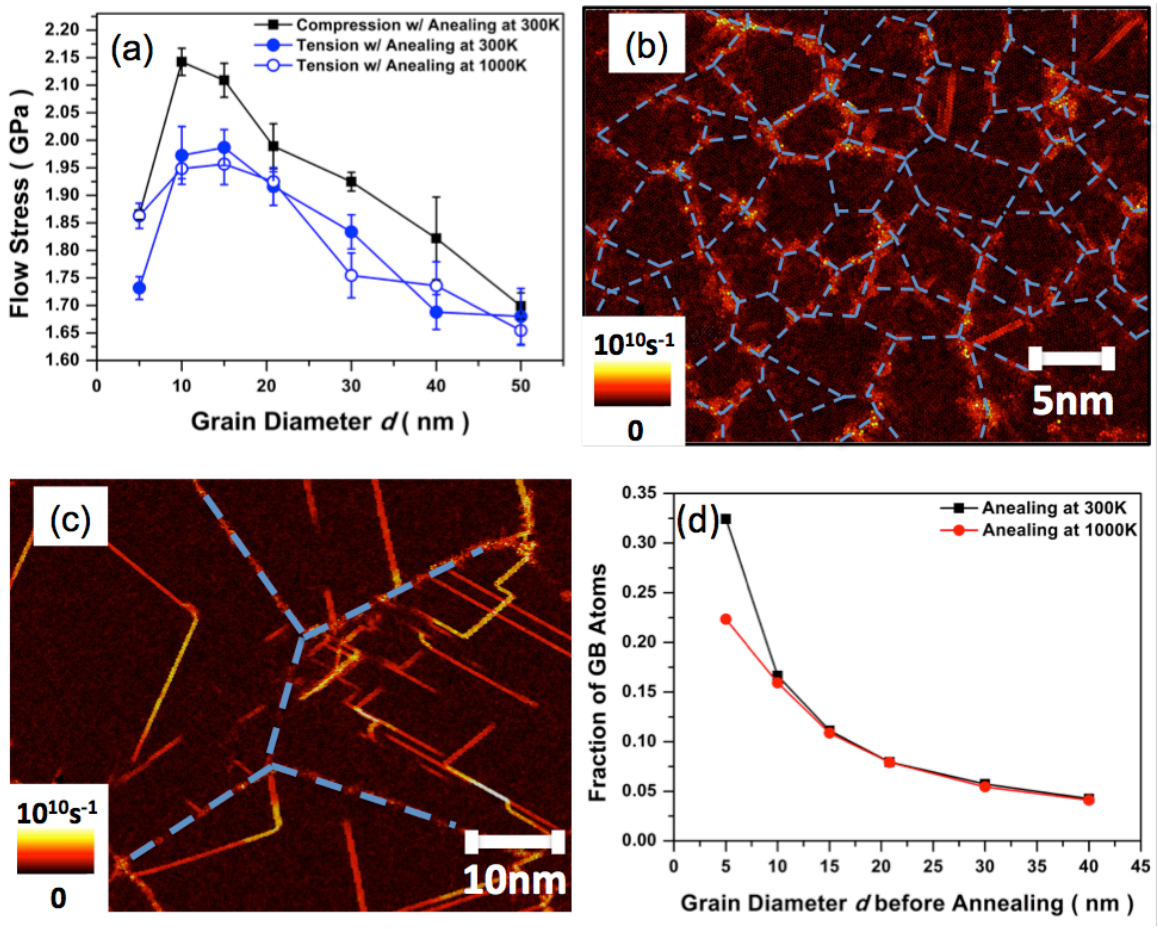

Figure 4.2.3 *Uniaxial deformation and annealing effects. (a) Dependence of flow stress on grain diameter d. Error bars correspond to a standard deviation from a mean value calculated in the regime where flow stress reaches a plateau as a function of strain. (b) and (c) Local shear strain rate in samples with grain size 5 nm and 40 nm, respectively. Blue dashed lines are added to indicate the positions of GBs. (d) Fraction of GB atoms in the entire sample as a function of the nominal grain size for two annealing temperatures. GB atoms were identified using common neighbor analysis*[18].

During sliding simulations, atoms in the bottom 1nm region and the 1nm thick vertical region far away from the sliding tip are kept fixed (frozen) to provide rigid boundaries. The temperature is

controlled using a velocity-rescaling algorithm in a 3nm-thick thermostat layer of atoms adjacent to the bottom frozen layer. Sliding simulations are performed at 300K.

The tip is prepared from a melt-quenched amorphous SiC by cutting out a spherical shell, which is 3 nm thick, has the radius of cap curvature of 10 nm and the height of 40 nm. The shell is relaxed at 300K for 200ps. In preparation of the amorphous SiC, we used the environment-dependent interatomic potential[19]. Tip-substrate interactions are described by Lennard-Jones potential[20], using the parameters: $\sigma_{Cu-Si} = 0.3039\text{nm}, \varepsilon_{Cu-Si} = 0.029\text{eV}$, $\sigma_{Cu-C} = 0.2869\text{nm}, \varepsilon_{Cu-Si} = 0.031\text{eV}$. These parameters were determined using Lorentz–Berthelot rules, $\sigma_{ij} = \frac{\sigma_i + \sigma_j}{2}$ and $\varepsilon_{ij} = \sqrt{\varepsilon_i \times \varepsilon_j}$ based on published parameters for pure Si, C[21], and Cu[22].

During sliding simulations, the tip is held rigid and it is moved laterally across the sample's surface with a velocity of 50 m/s. Simulations are performed at cutting depths between 1 nm and 11 nm. Maximum temperature observed at the contact interface is 390.1K and therefore it is not expected to have any significant impact on the results. The friction force and the normal forces are calculated by summing up all the forces acting on the tip in the lateral and normal directions, respectively. Dependences of the normal load L, the hardness H ,the friction coefficient μ,*the chip volume* V_{chip}, the total displaced volume V_{disp}^{tot}, and the anisotropy factor A on the lateral tip displacements are shown in Fig. 4.2.4. The values of these properties reported in the main paper are calculated as averages over at least 130 nm of sliding (after equilibration time). For L, μ, V_{chip}, and A, interval for averaging starts at a tip displacement of 25 nm. For H, average interval starts at 50 nm. The total displaced volume V_{disp}^{tot} increases linearly with the tip displacement for all samples and cutting depths (Fig. 4.2.4). The value of V_{disp}^{tot} shown in Fig. 4.3.5(a) of the main paper represents the total displaced volume accumulated over 130 nm of sliding distance. The concepts of L, H, μ, V_{chip}, V_{disp}^{tot} and *A will be discussed in section 4.3 in detail.*

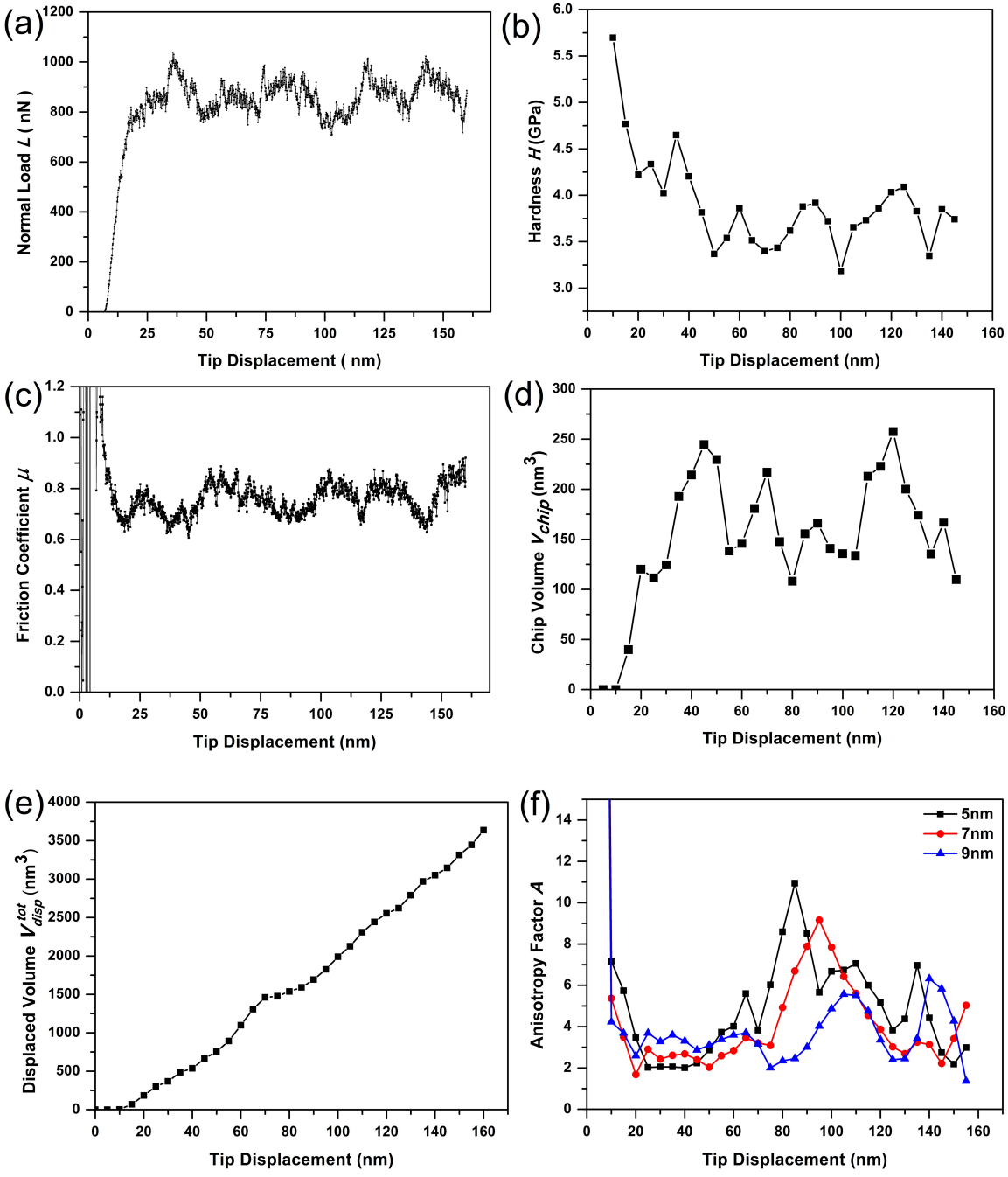

Figure 4.2.4 *L, H, μ, V_{chip}, V_{disp}^{tot}, and A as a function of tip displacement for a nanocrystalline sample with 30 nm grain diameter. Data for other grain sizes show similar qualitative trends. For (a)-(e), the dependences of L, H, μ, V_{chip}, V_{disp}^{tot} on the tip displacement are plotted at a cutting depth of 4 nm.*

Anisotropy ratio A vs tip displacement relation is plotted at cutting depths of 5 nm, 7 nm, and 9 nm, because these are the only cutting depths for which A values are reported in Fig. 4.3.7(c).

We first plot these averaged properties as a function of either the normal load or the cutting depth (Figs. 4.2.5a-d). In order to determine various quantities at the same normal load, we use the following approach. We first linearly interpolate data between the measured points. Then by taking cross-sections at different loads (vertical lines in Figs. 4.2.5a-d) we can make plots of measured properties as a function of grain size (figures in the main text). Crystallographic arrangement of atoms (fcc, hcp, or other) was determined using the common neighbor analysis[18].

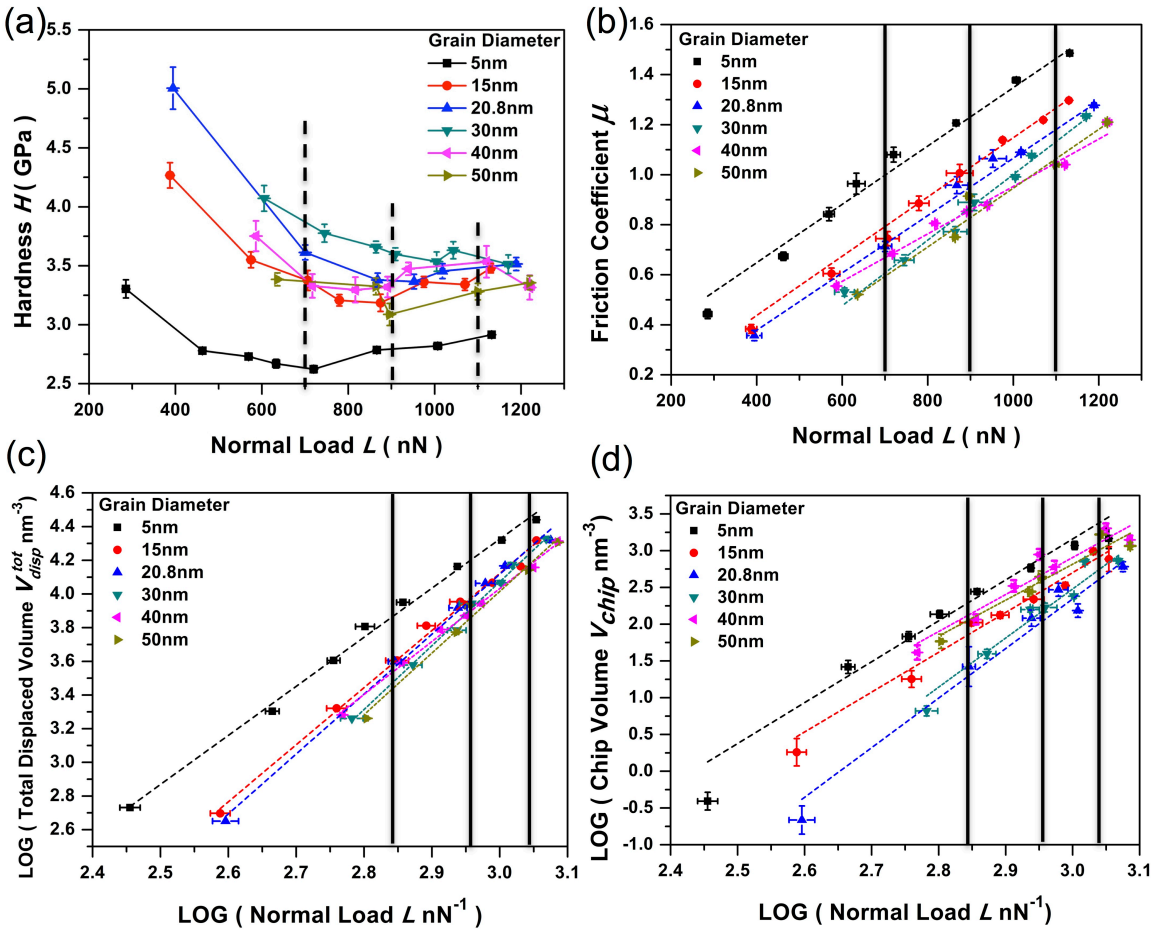

Figure 4.2.5 *Dependence of H, μ, V_{disp}^{tot}, V_{chip} on normal load. (a) Hardness H vs. normal load. (b) Friction coefficient μ vs. normal load. (c) Total Displaced volume V_{disp}^{tot} vs. normal load. (d) Chip volume V_{chip} vs. normal load. Each data point corresponds to an average calculated over sliding distance (excluding equilibration time). Error bars correspond to one standard deviation from the mean value. Three vertical dashed lines in (a) and three vertical solid lines in (b), (c), (d) represent the same normal load corresponding to 700 nN, 900 nN and 1100 nN.*

4.3 Results

4.3.1 Friction Coefficient

We have first calculated hardness *H* by dividing the average normal force *L* by the projected contact area *S*, both calculated during simulations of sliding. *H* was found to have a maximum at *d* = 30 nm (Fig. 4.3.1a), where *d* is the grain size averaged over the entire sample. One should note that the grain size near the surface is smaller than in the bulk because of the way the samples were prepared. The presence of the maximum in *H* is in qualitative agreement with trends in uniaxial deformation of nc Cu previously reported in literature[1] and reproduced in our simulations (Fig. 4.2.3a). We have also calculated friction coefficient μ, which is defined as the friction force divided by the normal load. The results are plotted in Fig. 4.3.1b as a function of grain diameter. We find that μ initially decreases with increasing *d*, but then becomes insensitive to it. μ is inversely proportional to *H* for grains smaller than ~30 nm (Fig. 4.3.1c). Because $\mu = F/L$ and $H = L/S$, we can calculate the lateral hardness $\tau = F/S = \mu H$, which is a constant if μ is inversely proportional to *H*. Thus provided that τ is constant, at the same normal load, *S* is smaller for harder materials, leading to a decreased resistance to sliding (μ) with increasing *H*. This is consistent with the traditional understanding of friction-hardness relation. However, it is interesting to note that for larger grains, we found that μ and *H* are no longer inversely proportional to each other, which suggests that in this

regime deformation mechanisms responsible for vertical hardness may be different than deformation mechanisms controlling friction.

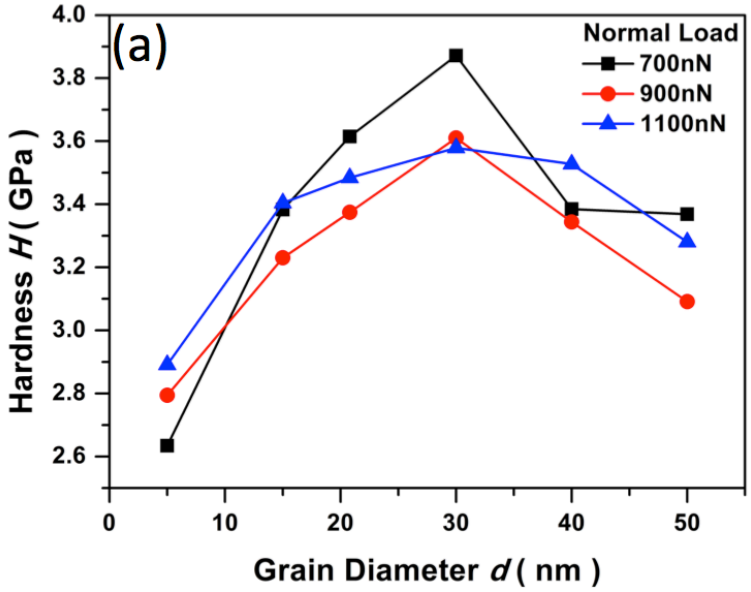

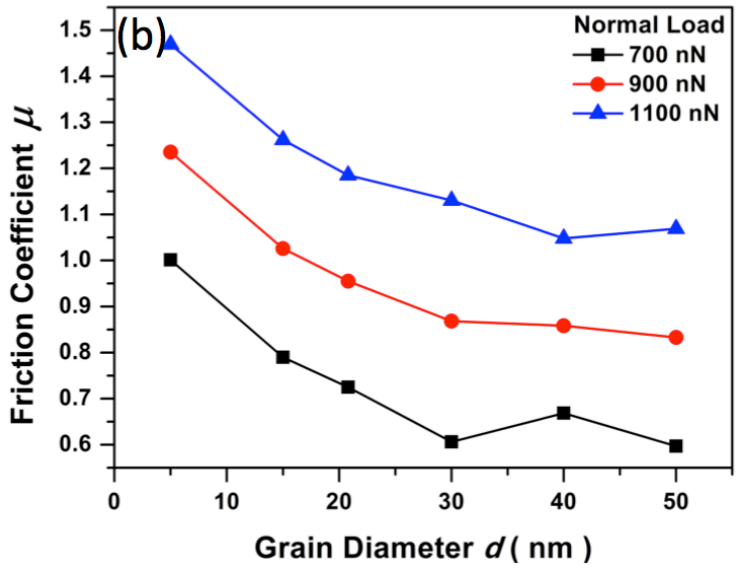

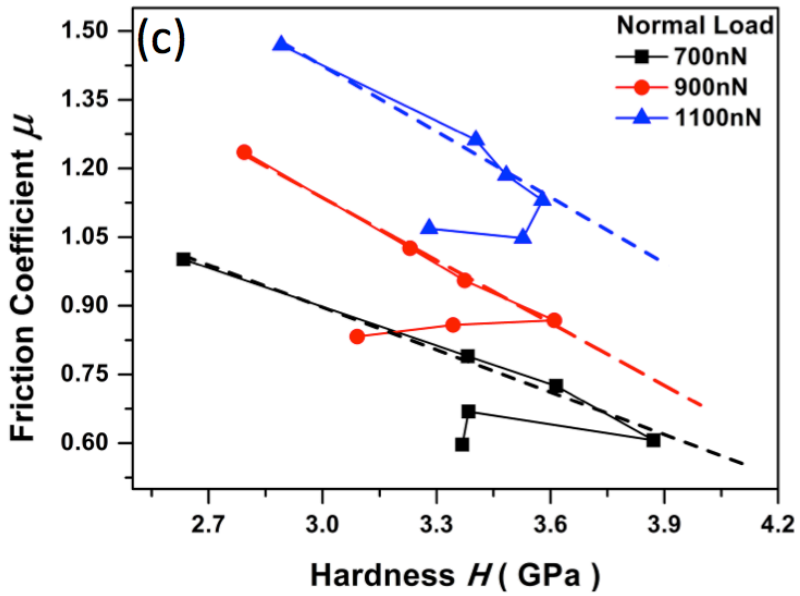

Figure 4.3.1 *(a) Hardness and (b) Friction coefficient as a function of grain size. (c) Friction coefficient vs. Hardness. Dashed lines correspond to expected linear trends.*

While deformation mechanisms that govern the decrease of hardness with increasing *d* in the larger grain size regime are already reasonably well understood in the context of the Hall-Petch relation[23,24], mechanisms that govern friction and its dependence on *d* are still unknown. To analyze the latter mechanisms, in Fig. 4.3.2a we show a cross-sectional view of the contact and we color code atoms based on their velocity component parallel to the sliding direction. Displayed velocities are averages calculated over 100 ps of sliding. The region outlined by points *ABEDC* represents the deformation regime of the Cu sample, which separates the undeformed material (below the *CDE* line) and the chip (above the *AB* line). There is essentially no plastic flow in the chip, except for a small amount of shear along the chip-tip contact line, which shear is generally ignored in this type of analysis.[25] In other words, almost all deformation takes place inside the *ABEDC* region and it is the shear in this region that accommodates frictional sliding and controls the friction force. Within this

region one can identify slip lines (the *CD* line is one of them), which are lines of constant velocity and which are parallel to the axes of maximum shear stress.[25]

So far we have not discussed how the geometric slip lines are related to the underlying structure of the nc Cu. To find such relations, in Figs. 4.3.2b and 4.3.2c we show distributions of local strain rate in samples with d = 5 nm and 30 nm, respectively. Details of strain rate calculations can be found in Chapter 2. For the 5 nm sample, the grain size is much smaller than the tip size. The tip-induced deformation regime encompasses multiple grains and plasticity proceeds by coordinated shearing in different directions along multiple GBs. Dislocation glide in the grain interior is inhibited by the dense network of GBs and there are no extended dislocation slips observed in our system. In contrast, in the 30 nm sample, where grain diameter is larger than tip size, deformation occurs partially or entirely in one grain and it is localized along a well-defined slip line. We will refer to this extended and relatively straight slip line as an easy-shear plane because it is expected to provide a lower resistance to shear than the meandering path of short-range shear events that accommodate tip-induced deformation in the 5 nm sample. One can now understand why friction transitions from grain size sensitive regime to grain size insensitive regime as the d increases. For $d \leq 30$ nm, both hardness and friction of nc Cu in our simulations are controlled by GB sliding as well as some limited dislocation activity inside the grains (Fig. 4.2.3b), which results in hardness and the friction coefficient being linearly dependent on one another (Fig. 4.3.1c). For larger grains, hardness is controlled by intragranular dislocations and their propensity to pile-up at the GBs (Fig. 4.2.3c), which mechanism is grain size dependent. Friction on the other hand is accommodated by formation of an easy-shear plane inside a single grain, which mechanism is not directly related to hardness and to a large extent is independent of the grain size.

We found two types of mechanisms to be responsible for formation of an easy-shear plane inside a crystalline grain. The first mechanism operates when one of the planes from the {111} family is

parallel or almost parallel to the direction of the geometric slip line (Fig. 4.3.2d). Partial dislocations propagate on the {111} plane, leaving behind a stacking fault (or a twin boundary), which in turn provides a plane with low resistance to shear. The second mechanism involves formation of a new GB along the geometric slip line (Fig. 4.3.2e), which is the result of a pile-up of dislocations (either statistically stored or geometrically necessary). Continued sliding is accommodated by development of parallel easy shear-planes as shown in Fig. 4.3.2f.

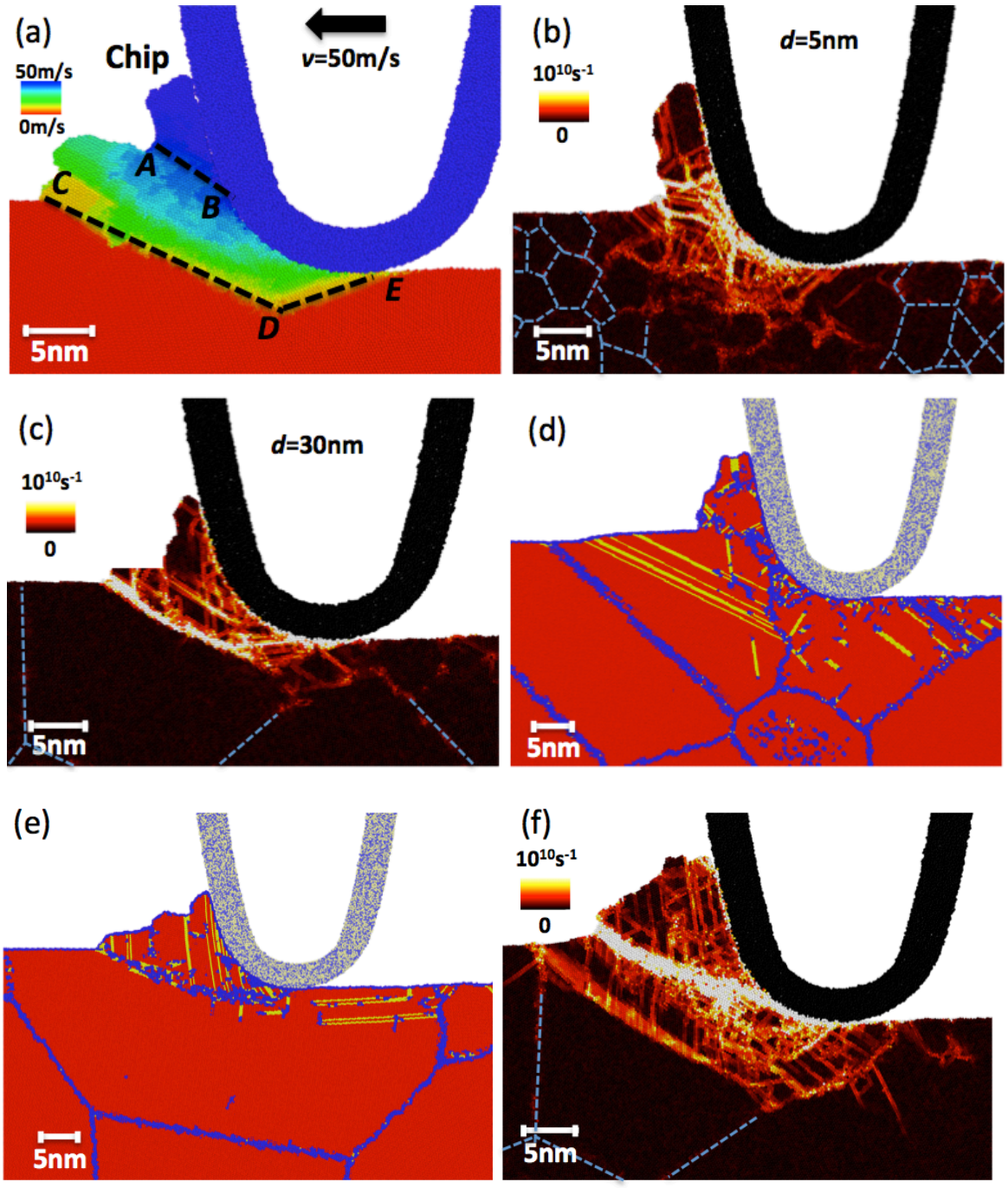

Figure 4.3.2 *Cross-sectional views of the contact area: (a) Atoms are color-coded by their lateral velocities. Dashed lines are slip-lines representing lines of constant lateral velocity. (b) and (c) Local shear strain rate in samples with grain size d=5 and 30 nm, respectively. Formation of (d) stacking faults and twin boundaries (yellow) and (e) a new GB (blue) in fcc Cu (red). (f) Formation of two*

parallel easy-shear planes. Colors represent the same local shear strain rate as in (b) and (c). Grain size in (d) and (f) is d=40 nm and in (e) d=50nm. Blue dashed lines in (b), (c), and (f) are added to indicate the positions of GBs away from the deformation region.

As discussed above, for the case where the tip size is small as compared to the grain size, there is a clearly defined slip line that develops inside individual grains during frictional sliding. This slip line is accommodated either by formation of twin boundaries and stacking faults (Fig.4.3.2d) or by formation of a new GB (Fig.4.3.2e). Here, we show that there are two general mechanisms of such GB formation. One involves pile-up of dislocations in the region of the slip line, which is a line parallel to the direction of the highest shear stress based on the geometry of the sample. The dislocations are nucleated at the surface of the sample or are emitted from existing GBs. The entangled dislocations in the pile-up rearrange to form a new GB and provide a plane of easy slip. This mechanism is illustrated in Fig. 4.3.3a. The second mechanism involves formation of geometrically necessary dislocations due to bending of the grain by the sliding tip. This mechanism is shown in Fig. 4.3.3b, where an array of geometrically necessary partial dislocations evolves into a new GB.

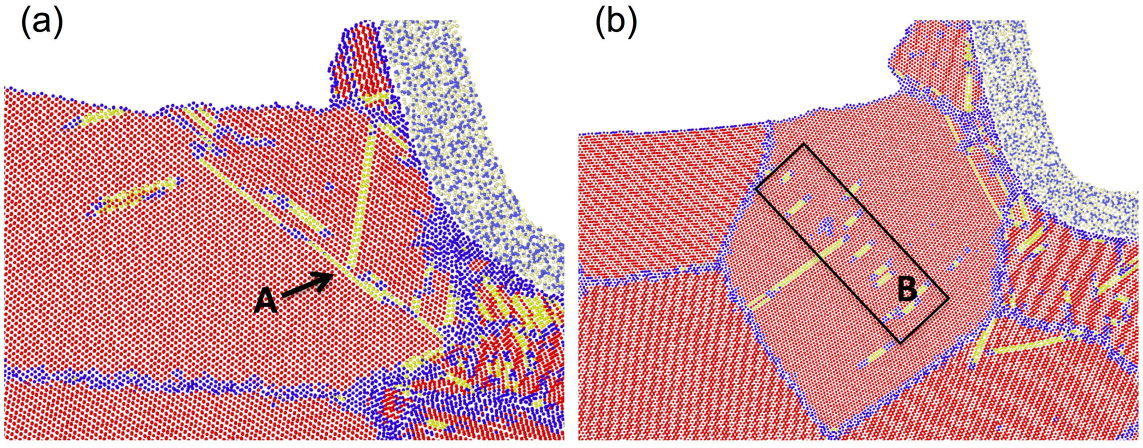

Figure 4.3.3 *Mechanisms of friction-induced GB formation. (a) Glide of partial dislocations nucleated at the surface is hindered (at location A) by a twin boundary parallel to the direction of the geometric slip line. (b) Formation of an array of geometrically necessary partial dislocations in region B. In both (a) and (b), fcc Cu atoms are shown in red. Yellow Cu atoms have hcp structure and represent stacking faults and twin boundaries. Blue represents those Cu atoms that do not have either fcc or hcp structure. Tip atoms are colored in white and light blue.*

4.3.2 Wear

How does wear of nc Cu depend on the grain size? In general wear can refer either to surface damage or to loss of material during sliding.[26] During tip sliding, surface material may be effectively displaced to the two sides of the groove and it may not accumulate in front of the tip. This wear mode is called plowing and it only leads to ridges and grooves left in the wake of the tip. Although in this case material is displaced, no chip formation or material loss takes place during sliding. In other words, wear does happen but there is no material loss. The displaced volume V_{disp} is a useful measure to quantify this type of wear.

In another case, displaced material can accumulate in front of the tip and form a chip. This wear mode is referred to as cutting. Chips only attach loosely to the surface and can easily become wear debris by fracturing with the help of small external force. Fracture often occurs at weak connections between the chip and the surface. It is much easier for chips in the cutting mode to become wear debris than for groove ridges to turn into debris in the plowing mode. As a result, chips can be regarded as precursors of wear debris. [25,27]

In experiments, tip vibration, irregular tip shape, and other external force during sliding will initiate the fracture and turn chips into surface debris. In our simulations, we do not apply such external forces, since this is not the focus of our study. As a result chip removal does not take place

in simulations, but chips are still precursors of wear debris and the chip volume V_{chip} is a reasonable measure to quantify such form of wear.

One important property of the chip material is that it is pushed forward by a tip and it moves together with a tip. Based on this property, one can use the velocity of each atom onto the sliding direction as the criterion for determining which atoms belong to the chip (blue atoms in Fig. 4.3.2a and Fig. 4.3.4a). It is interesting to note that the pile-up and chips have nc structure and form GBs, which is illustrated in Fig. 4.3.4b.

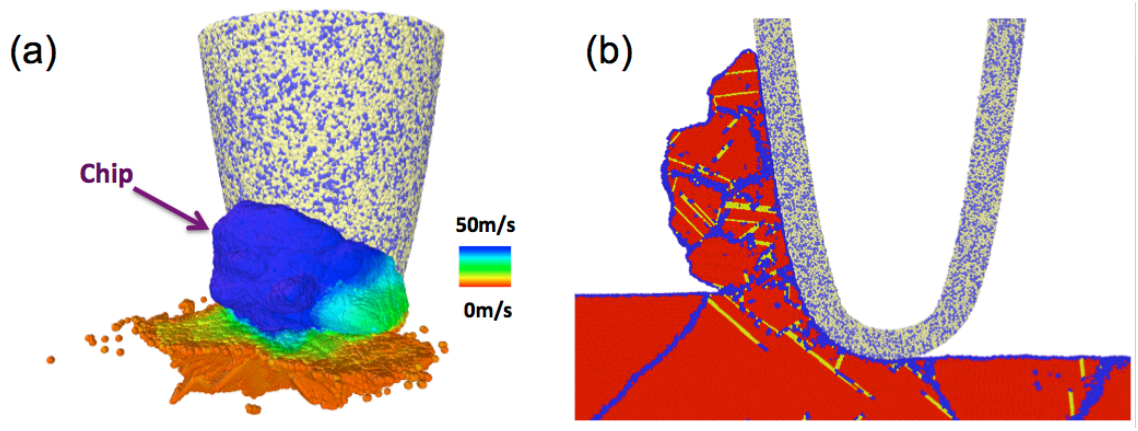

Figure 4.3.4 *(a) Chip formation in our simulations. Sample atoms are color-coded by their lateral velocities. (b) Formation of GBs inside the pile-up. Grain diameter is 40 nm and the average normal load is 1120nN. Color scheme is the same as in Fig. 4.3.3.*

We first quantify surface damage by calculating the total volume of displaced material V_{disp}^{tot} above the original surface of the sample after 130nm of sliding distance. V_{disp}^{tot} includes the pile-up in front of the tip and the plowed material behind it (Fig. 4.2.1a). This analysis is essentially equivalent to the measurements of groove volume or groove depth that are widely used in ball-on-disk wear tests[6] and nanoscratch experiments[28]. As shown in Fig. 4.3.1a, V_{disp}^{tot} first decreases with increasing d (in the small grain size regime) and then it becomes approximately constant (in the larger grain size

regime). It is perhaps not surprising that the dependence of V_{disp}^{tot} on d during sliding (Fig. 4.3.5a) qualitatively resembles the trend in μ (Fig. 4.3.1b), because larger friction leads to more displaced volume. In the large d regime, frictional sliding is accommodated by slip along an easy-shear plane inside a crystalline grain, where the size and position of the easy-shear plane depend on the contact geometry and are to a large extent independent of d. Slip along the easy-shear plane controls both the resistance to sliding (i.e., the friction coefficient) and the displaced volume.

What is unexpected, however, is the trend with d that we found for the average chip volume V_{chip} (Fig. 4.3.5b). Because chips are regarded as precursors of wear debris, V_{chip} is one of the accepted ways to quantify wear-induced material loss. In our simulations, chip atoms are identified as having almost the same lateral velocity as the tip (atoms above the AB line in Fig. 4.3.2a and blue atoms in Fig. 4.3.5a). Chip volumes reported in Fig. 4.3.5b are averaged over the sliding distance.

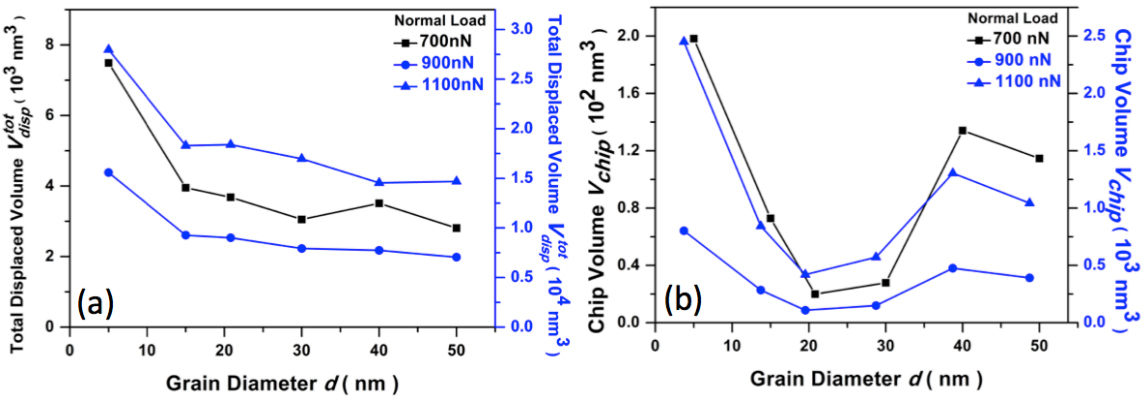

Figure 4.3.5 *Dependence of wear on grain diameter d. (a) Volume of total displaced material after 130nm of sliding distance. (b) Average chip volume during tip sliding.*

We find (Fig. 4.3.5b) that there is an optimum grain size (~20 nm) that minimizes V_{chip}. There are two factors that contribute to V_{chip}, which are mass flux into the chip and mass flux out of the chip. Mass flux into the chip is controlled by hardness and since it is more difficult to displace a hard material, mass flux into the chip is smaller for harder materials. Interestingly, the mass flux out of the

chip is controlled not only by hardness, but also by another mechanism that can reduce the chip volume. This mechanism is cracking of the pile-up (Fig. 4.3.7a and 4.3.7b), which increases the flow of displaced material to the back of the tip. Cracking in turn is influenced by the anisotropy of the pile-up material because the more anisotropic the pile-up, the easier it is to initiate a crack. Grain size plays an important role in cracking because it is responsible for the anisotropy of the pile-up (see Fig. 4.3.7a,b and section 4.3.5) and because cracking occurs primarily along GBs (Fig. 4.3.7b).

To quantify pile-up anisotropy, we divide the atoms of the pile-up (material displaced above the surface) into vertical slices, where each slice is defined based on the polar angle θ it forms with the direction of sliding (Fig. 4.3.6). Anisotropy can be manifested in two ways. First, the center of mass of the pile-up ($\theta = \theta_c$) can be misaligned with the direction of sliding ($\theta = 0°$) (Figs. 4.3.6a-4.3.6c). This contribution to anisotropy can be quantified as $|\frac{\sum_0^n \theta \times N_\theta}{\sum_0^n N_\theta}|$, where N_θ stands for the number of atoms in a vertical slice of the pile-up.

The second contribution to anisotropy represents variation of the mass within each slice from the value averaged over all the slices (Figs. 4.3.6d-4.3.6f) and it can be quantified as $\sqrt{\frac{\sum(\frac{N_\theta - N_0}{N_0})^2}{n}}$. Here, N_0 is the value of N_θ averaged over all n slices. Anisotropy factor A is defined as the product of the two terms $A = |\frac{\sum_0^n \theta \times N_\theta}{\sum_0^n N_\theta}| \times \sqrt{\frac{\sum(\frac{N_\theta - N_0}{N_0})^2}{n}}$.

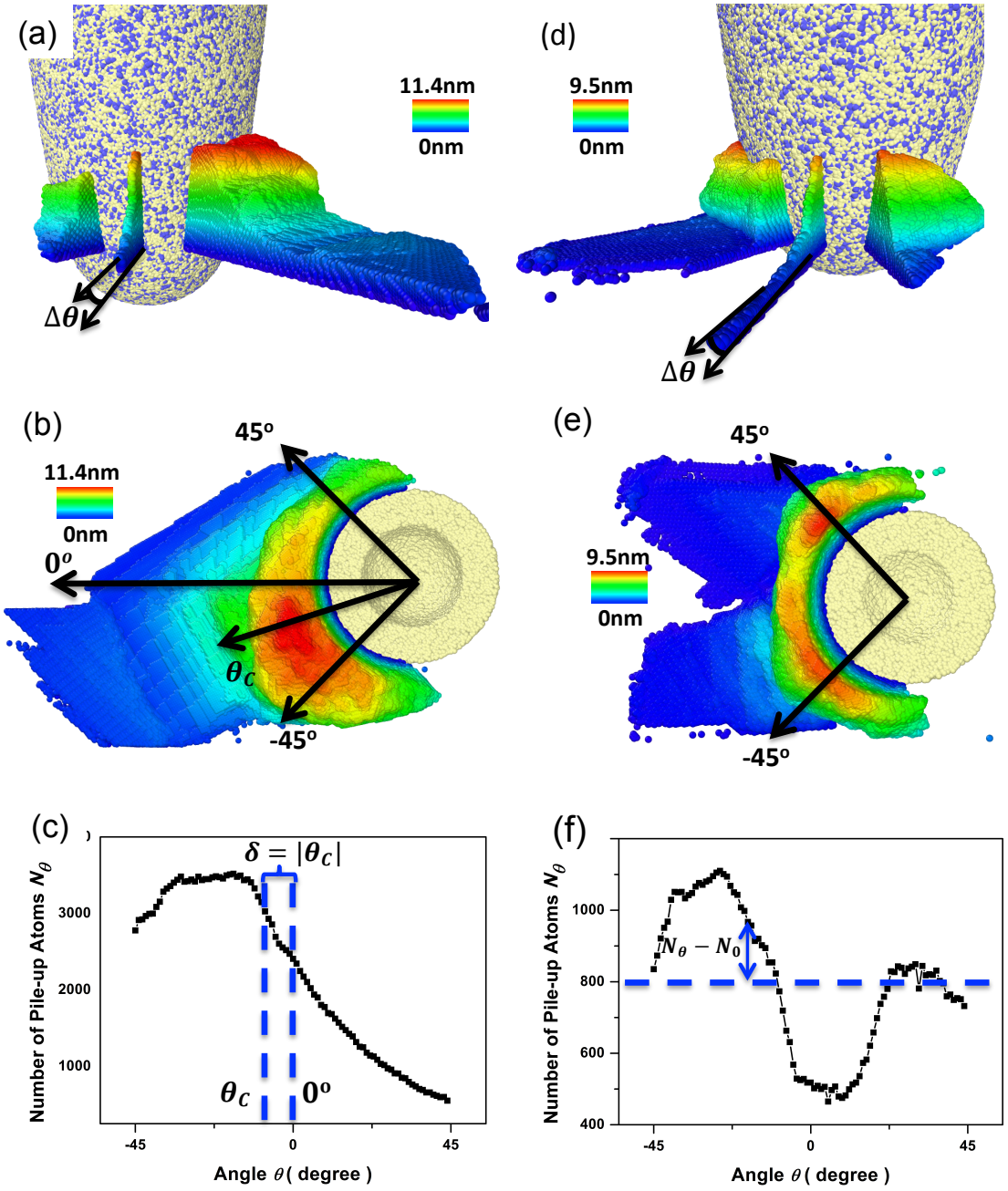

Figure 4.3.6 *Physical meaning of the anisotropy factor A. (a) side and (b) top view of the pile-up, where colors represent the height of material above the surface. This example shows deviation of a center of mass θ_c from the direction of sliding (θ = 0°). (c) Number of atoms in the pile-up N_θ as a function of the angle θ for the example shown in (a) and (b). (d) side and (e) top view of the pile-up for the case where contributions to anisotropy comes from deviation of mass in each slice from the*

average value. (f) Number of atoms in the pile-up N_θ as a function of the angle θ for the example shown in (d) and (e).

Anisotropy factor *A* captures both, the deviation of the pile-up's center of mass from the sliding direction and fluctuation of the number of atoms among the different slices. As shown in Fig. 4.3.7c, *A* has a maximum at *d*~20 nm, which explains why chip volume is minimized for this grain size.

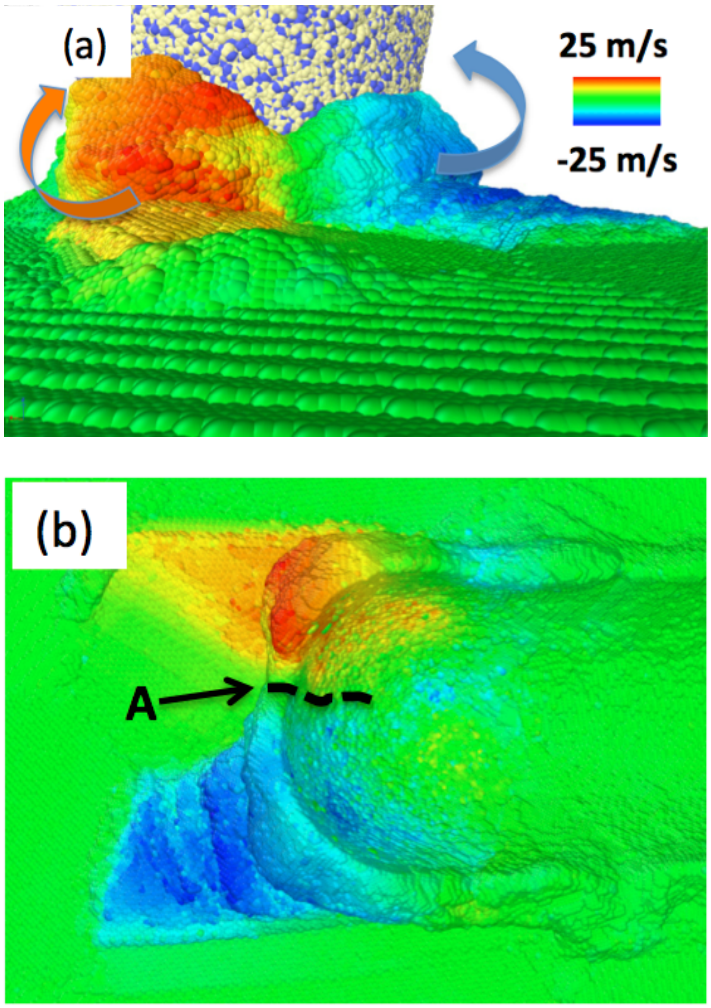

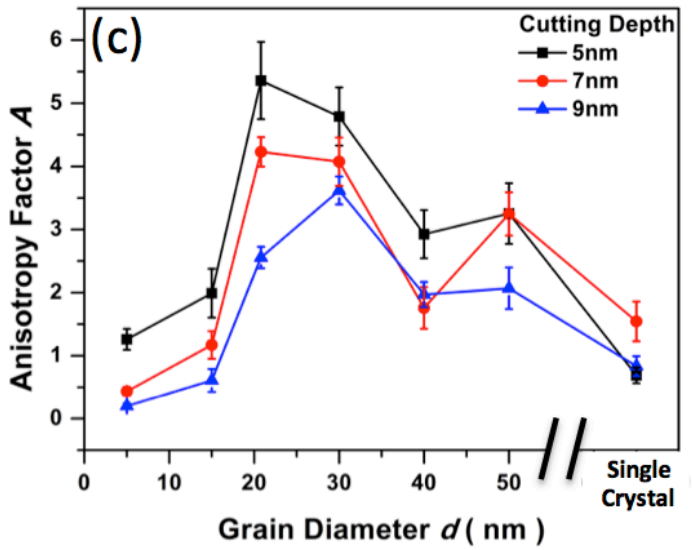

Figure 4.3.7 *Anisotropy of pile-up: (a) Perspective view and (b) top view. Atoms are color-coded by their velocity component perpendicular to the sliding direction. In (b), the region marked as A shows where cracking initiates and the dashed line denotes crack propagation path. (c) Anisotropy factor A as a function of grain size d for three different cutting depths. Cutting depth is defined as the vertical distance between the lowest point on the tip and the undamaged surface of the sample. The reported values of A are averages calculated over at least 130 nm of the sliding distance and error bars are defined as a standard deviation from the mean.*

The reason why A has a maximum at d~20 nm is a coupling between the grain size and the size of the cutting tool. Specifically, the diameter of the projected area of the tip is ~20 nm. For larger grain sizes (single crystal being an extreme case), the wavelength of heterogeneity that results from the grain structure of the material is too large to have a significant influence on the anisotropy on the length scale probed by the tip. In this case the tip is most of the time plowing through a single crystal grain with sporadic encounters of GBs. For smaller grain sizes (amorphous material being an extreme case), the wavelength of the grain heterogeneity is small compared to the tip size and even if small

cracks develop, they do not propagate and do not fracture the pile-up as effectively as observed in the case of intermediate grain sizes.

In order to further test the hypothesis that A is maximized when the tip size and the grain diameter are comparable, we fix the grain size and change the diameter of the tip. For this purpose, we use a series of cylindrical tips with diameters d_{tip} that range from 4 nm to 28 nm and we perform scratch simulations on nc-Cu samples with average grain diameter of 15 nm and a cutting depth of 7 nm (Fig. 4.3.8a). To avoid stress concentrations at tip corners, we blunt the corners of the tip so that the radius of curvature of the corner r is 2 nm. Cylindrical tips are used instead of parabolic tips with a spherical cap in order to eliminate the effect of tip-attack-angle, which varies with the diameter of a parabolic tip and which is expected to have a significant effect on pile-up and chip formation during cutting.

We also introduce the ratio $k = \frac{S_g}{S_t}$. Here, S_g is the average cross-sectional area of grains intersected by the surface plane. It is measured as the ratio between the total surface area and the total number of grains observed on the surface. S_t is the cross-sectional area of the tip within the plane of the surface. Grain and tip sizes are comparable when k is close to 1. Dependence of A on k for 7nm cutting depth is shown in Fig. 4.3.8b. One can see that A is maximized when $k \approx 1$ for both cases considered in this study: changing the grain diameter and keeping the size of the tip constant and changing the diameter of the tip and keeping the grain size constant.

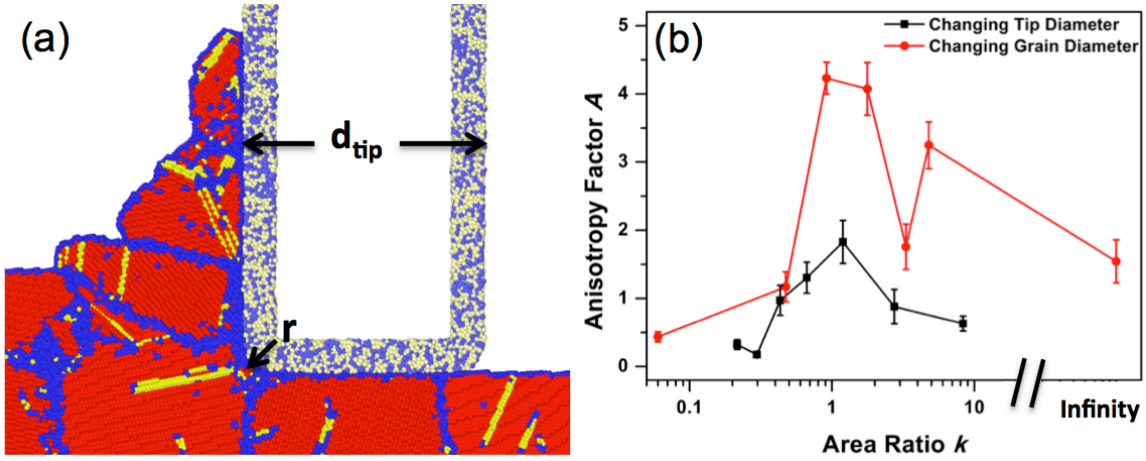

Figure 4.3.8 *(a) A cylindrical tip made of amorphous SiC with a diameter d_{tip} cutting a copper sample with grain diameter 15nm at a cutting depth of 7nm. Colors have the same meaning as in Fig. 4.3.4. (b) Dependence of anisotropy factor A on the area ratio k. The reported values of A are averages calculated over at least 130 nm of the sliding distance and error bars are defined as a standard deviation from the mean.*

4.4 Conclusions

Our results demonstrate that size-effects in friction and wear depend on both, intrinsic (grain size) and extrinsic (contact size) factors. When the average grain size is smaller than tip sizes, friction coefficient is inversely proportional to hardness. When the grain size is larger than the tip, friction coefficient becomes insensitive to hardness. The lack of dependence of μ on hardness is due to a newly found mesoscopic deformation mechanism, which is formation of an easy-shear plane. Surface damage first decreases with increasing hardness (in the small grain size regime) and then becomes insensitive to hardness (in the large grain size regime). We also found that there is a grain diameter that minimizes material loss. This effect is also due to a coupling of grain size and tip size, which coupling can maximize pile-up anisotropy and therefore maximize the volume of the chip.

References:

1. J. Schiotz, and K. W. Jacobsen, *Science* 301, 1357-1359 (2003).
2. J. Schiotz, F. D. Di Tolla, and K. W. Jacobsen, *Nature* 391, 561-563 (1998).
3. D. Jang, and J. R. Greer, *Scripta Materialia* 64, 77-80 (2011).
4. J. Y. Kim, D. Jang, and J. R. Greer, *Scripta Materialia* 61, 300-303 (2009).
5. Z. N. Farhat, Y. Ding, D. O. Northwood, and A. T. Alpas, *Mat Sci Eng a-Struct* 206, 302-313 (1996).
6. Y. S. Zhang, Z. Han, K. Wang, and K. Lu, *Wear* 260, 942-948 (2006).
7. E. M. Bringa, A. Caro, Y. Wang, M. Victoria, J. M. McNaney, B. A. Remington, R. F. Smith, B. R. Torralva, and H. Van Swygenhoven, *Science* 309, 1838-1841 (2005).
8. H. Van Swygenhoven, *Science* 296, 66-67 (2002).
9. K. W. Jacobsen, and J. Schiotz, *Nat Mater* 1, 15-16 (2002).
10. V. Yamakov, D. Wolf, S. R. Phillpot, A. K. Mukherjee, and H. Gleiter, *Nat Mater* 1, 45-49 (2002).
11. M. Mishra, and I. Szlufarska, *J Mater Sci* 48, 1593-1603 (2013).
12. M. Mishra, C. Tangpatjaroen, and I. Szlufarska, *Journal of the American Ceramic Society* 97, 1194-1201 (2014).
13. N. Beckmann, P. A. Romero, D. Linsler, M. Dienwiebel, U. Stolz, M. Moseler, and P. Gumbsch, *Physical Review Applied* 2, 064004 (2014).
14. S. Plimpton, J Comput Phys 117, 1-19 (1995).

15. Y. Mishin, M. J. Mehl, D. A. Papaconstantopoulos, A. F. Voter, and J. D. Kress, *Physical Review B* 63, 224106 (2001).

16. K. M. Youssef, R. O. Scattergood, K. L. Murty, and C. C. Koch, *Applied Physics Letters* 85, 929-931 (2004).

17. N. Q. Vo, R. S. Averback, P. Bellon, A. Caro, *Physical Review B* 78, 241402 (2008).

18. D. Faken, H. Jónsson, *Computational Materials Science* 2, 279-286 (1994).

19. J. F. Justo, M. Z. Bazant, E. Kaxiras, V. V. Bulatov, and S. Yip, *Physical Review B* 58, 2539-2550 (1998).

20. J. E. Jones, *Proceedings of the Royal Society of London. Series A* 106, 463-477 (1924).

21. N. Rajabbeigi, B. Elyassi, T. T. Tsotsis, and M. Sahimi, *J Membrane Sci* 335, 5-12 (2009).

22. P. Guan, D. R. Mckenzie, and B. A. Pailthorpe, *J Phys-Condens Mat* 8, 8753-8762 (1996).

23. See Supplemental Material at [] for additional description of methods, data, concepts, and analysis of the large-scale simulations.

24. E. O. Hall, *Proceedings of the Physical Society. Section B* 64, 742 (1951).

25. N. J. Petch, *The Cleavage Strength of Polycrystals*. (J. Iron Steel Inst., London, 1953), vol. 173.

26. M. C. Shaw, *Metal Cutting Principles*. (Clarendon Press, Oxford, 1984).

27. B. Bhushan, *Principles and Appliations of Tribology*. (A John Wiley & Sons Ltd., New York, ed. 2, 2013).

28. D. A. Stephenson, and J. S. Agapiou *Metal Cutting Theory and Practice*. (Marcel Dekker,Inc., New York, 1997).

29. Y.-R. Jeng, P.-C. Tsai, and S.-H. Chiang, *Wear* 303, 262-268 (2013).

Chapter 5. Morphology and Mechanical Properties of Nanocrystalline Cu/Ag Alloy

5.1 Introduction

Cu alloys with superior bulk mechanical properties have been the subject of intensive research for many years. One way to enhance the mechanical properties of Cu is through grain refinement to the nanometer regime, which has been reported to lead to significant increase in strength[1], hardness[2], and ductility[1,3]. Many experimental[1,2,3] and simulation[4,5,6] studies reported that there is an optimum grain size that maximizes the strength of Cu. It was hypothesized that this maximum strength is due to a crossover of the dominant deformation mechanisms, which are dislocation-mediated plasticity in the large grain size regime and GB sliding in the small grain size regime.[4,5,6] Another promising way to strengthen Cu is through alloying. Cu/Ag is a widely studied alloy not only because it is a simple model alloy system, but also because it has both high strength and high conductivity. These properties are important for instance for applications as high-field pulsed magnet.[7] Ag may be able to strengthen Cu in several ways. It has been reported that when Ag concentration is below 1.5%, Ag dopants segregate to GBs, they reduce the GB energy of nc Cu and make GB sliding more difficult, which in turn increases the yield strength of nc Cu.[9] In addition, nc metals are often energetically unstable and grain coarsening can happen rapidly even at modest temperature. [10] Ag dopants segregated at GBs can potentially stabilize the nc structures and thus preserve the superior mechanical properties of nc Cu. Thirdly, when Ag are supersaturated in Cu matrix, Ag precipitates can be nucleated and grow in the grain interiors which may strengthen Cu by impeding motions of dislocations. It has been observed that the ultimate tensile strength (UTS) of Cu-Ag alloys increases when Ag concentration increases from 0 to 6%. A quantitative model including contributions from

work-hardening, Ag solution, and Ag precipitates was used to explain the increase in UTS.[11] In another study, Sakai et al explored large Ag concentration regime and found that increasing Ag concentration from 2% to 60% leads to initial strengthening of the alloy with Ag concentration followed by saturation when Ag concentration reaches 10-20%. [7]

Mechanical properties and deformation mechanisms of Cu/Ag alloy are highly dependent on the details of the microstructure, which depend on Ag concentration. Based on scanning transmission electron microscopy (STEM) observations of various binary alloy systems,[8] the thickness of GB complexions first increases discontinuously and then continuously, with the increase of dopants concentration. When dopants concentrations are small, the dopants tend to fill GBs layer by layer in a stepwise manner. With the increase of dopants concentrations, the complexions of monolayer, bilayer, trilayer, and nanolayer are formed sequentially. Here the nanolayer complexions refers to structures that are 1-2 nm in thickness, which is thicker than trilayer complexions, but thinner than wetting layers with a bulk phase. The aforementioned four GB complexions, including the nanolayer one, are regarded as part of a GB. When the dopants concentration is large enough, the dopants form a GB layer that has crystallographic structure of bulk material and two newly formed interfaces. In this case, the layer thickness will increase continuously with the increase of dopants concentrations. Various models such as lattice-gas model have been proposed to interpret the discrete and continuous thickening of dopants layers.[8]

Besides dopants concentration, sample-preparation methods can also greatly influence the microstructure of Cu/Ag alloy. For instance, Cu-Ag alloys casted from the pure Cu and pure Ag are composed of Cu-rich region and Ag rich region. The Cu-rich region is located at grain interiors and the Ag-rich region is located at GBs.[12] When the concentration of Ag is low, Ag phase is dispersed as isolated islands at GBs. When Ag concentration increases, Ag phase shows a continuous network of layered region at GBs, which separates Cu grain interiors. The Ag GB layers and Cu matrix are

reported to have cube-on-cube orientation relationship. Cu/Ag alloys can be also prepared by physical vapor deposition and subsequent annealing. In such alloys, Ag precipitates at GBs grow to the size comparable to that of Cu grains.[13] It has been shown that the addition of tungsten restricts coarsening of Ag precipitates, resulting in the presence of a Ag wetting layer at GBs.

In addition to the morphology of Ag dopants regions, the types of Cu/Ag interfaces can also strongly influence the mechanical properties of Cu/Ag alloys. For a casted Cu/Ag alloy with Cu and Ag phases, only Cu/Ag interfaces with cube-on-cube and twin orientations have been reported.[14,15,16] The cube-on-cube interface has $\{111\}_{\mathrm{Ag}}||\{111\}_{\mathrm{Cu}}$ habit plane with misfit dislocations and atomic steps which can relax the interface energy due to Cu/Ag lattice mismatch. The twin interfaces can be hetero-twin interfaces with $\{111\}_{\mathrm{Ag}}||\{111\}_{\mathrm{Cu}}$ habit plane or incoherent-twin interfaces with $\{\bar{3}13\}_{\mathrm{Ag}}||\{\bar{1}12\}_{\mathrm{Cu}}$ habit plane. The hetero-twin interface also possesses misfit dislocations and atomic steps since they have the same lattice mismatch with the cube-on-cube interfaces, while only atomic steps have been reported for the incoherent-twin interface. Due to the abundance of the cube-on-cube, hetero-twin, and incoherent-twin Cu/Ag interfaces in the cased structures, it can be reasonably anticipated that these interfaces are more energetically stable than other type of Cu/Ag interfaces. Altering proportions of these interfaces in the Cu/Ag alloys by changing processing conditions can significantly influence the mechanical properties and deformation mechanisms.[16,17]

Despite the aforementioned findings about the relation of the microstructure to mechanical properties of Cu/Ag alloys, no research has been conducted on nc-Cu/Ag alloy with general GB types and with concentrations ranging from 0 to tens of mole percentage. Previous studies of mechanical properties of Cu/Ag alloys reaching concentration of tens of mole percentage are limited to polycrystalline samples with micrometer-sized grains. MD simulations have been used in the past to investigate the strength of nc Cu/Ag alloy but with only up to 1% Ag atoms segregated at GBs, when no precipitates are formed even in the GBs.[9] It is still unknown how the microstructure and

mechanical properties of nc-Cu-Ag alloys evolve in high Ag concentration regime when Ag precipitates or even Ag bulk phases are formed. A transition between monolayer Ag complexions and bilayer Ag complexions have been discovered in a $\sum 5(310)$ Cu GB using semi-grand canonical Monte Carlo simulations.[18] We still need to investigate the transitions of complexions in general GBs of a nc structure. It was found that Ag dopants segregated at GBs influence GB sliding through changing GB energy,[9] while their possible influence on dislocation-mediated plasticity in grain interiors was neglected and is still needed to explore. Moreover, despite that the strength of nc Cu/Ag alloys increases with Ag concentration when Ag is dilute,[9] it will be fascinating to know whether there is a Ag concentration at which the strength turns down and which maximizes the strength of Cu/Ag alloys if we continue to increase the Ag mole percentage.

5.2 Methods

5.2.1 Preparing nc Cu samples

To address the above questions, we conduct atomistic simulations of nc Cu/Ag alloys in the range of mole concentration between 0 and 24.4%. MD simulations are performed with the LAMMPS software package[19] using the embedded atoms method (EAM) force field[20]. We first generate nc structures of pure Cu using the Voronoi algorithm. The average grain diameters in different samples are 5, 10, 15, 20.8, 30, 40, and 50nm, which correspond to 24.4, 25.4, 25.5, 25.6, 45.6, and 74.4 million atoms, respectively. Grain diameter distribution follows the Gaussian distribution, which is consistent with experimental distributions reported for nc Cu.[21] Periodic boundary conditions are applied to all three dimensions. Samples prepared in this way are then relaxed for 1ns at 300K and zero pressure using Berendsen's thermostat and barostat.

5.2.2 Alloying

After relaxation, nc Cu samples with 5, 15, and 40nm grain diameters are selected for alloying with various concentrations of Ag. A hybrid MC/MD method[22] is utilized to introduce Ag dopants to the nc Cu samples, and to relax the structures energetically. The MC/MD simulations are performed at 300K and zero pressure for the total of time of 1ns. The key idea of this method is to perform iteratively transmutational MC steps, which sample semi-grand-canonical ensemble, and MD simulations for 50fs. In the MC run, trial swaps are carried out by randomly selecting an atom (can be either Cu or Ag) and by replacing it with the other species. The trial moves are accepted or rejected according to the Metropolis algorithm. During the 1ns alloying and relaxation, on average there are 20,000 trial moves performed on each atom in the system. One example of the doped nc Cu/Ag alloy is shown in Fig. 5.2.1a. As expected, Ag dopants are predominately segregated to GB regions because Cu/Ag is an immiscible alloy system.

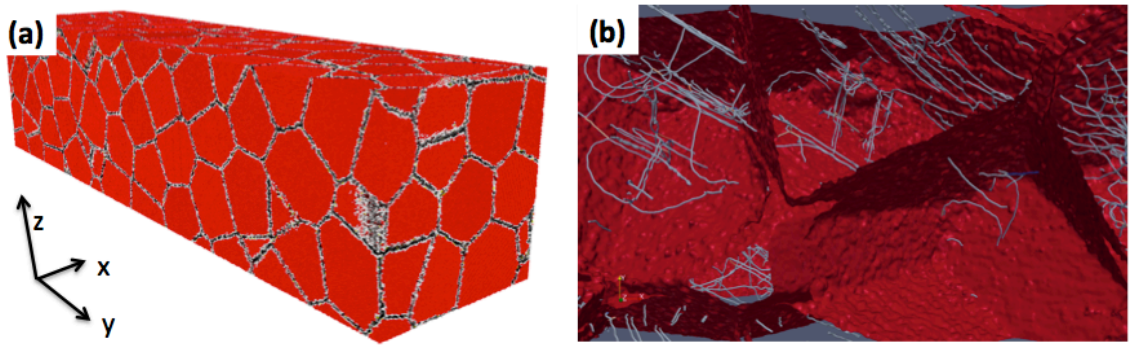

Figure 5.2.1 *(a) Ag-doped nanocrystalline Cu with 15 nm average grain diameter and 24.9 Ag atoms per nm^2 concentration. Red atoms are FCC Cu atoms. White atoms are defect Cu atoms, which means that they do not have FCC, HCP, or BCC structures. Ag atoms are colored black. Defect Cu atoms and Ag atoms mark the GB regions, and FCC Cu atoms are primarily found in grain interior. (b) Intragranular dislocation (grey). Red planes represent GBs.*

5.2.3 Loading

Uniaxial tension simulations are performed at 300 K with engineering strains up to 15% and with a strain rate of 5×10^8 s^{-1}. The deformation strain is applied in z- direction through alternating steps of straining the system by 0.05% and 1ps MD equilibration. During the entire processes, the Nose-Hoover thermostat is used in x-, y-, and z-directions to keep the temperature at 300K. The Nose-Hoover barostat is used to maintain zero pressure in x- and y-directions, and the x- and y- dimensions of the system are freed to account for Poisson effect. Flow stress is defined as the average values of stress measured between the engineering strain of 12% and 15%. In this regime the stress fluctuates around an approximately constant value.

5.2.4 Analysis Methods

5.2.4.1 Ag Concentration

In addition to the mole fraction of Ag, Ag concentrations C_{Ag} are also calculated as $C_{Ag} = \frac{N_{Ag}}{A}$, where N_{Ag} is the total number of Ag atoms in the system, and A is the total GB area in the system. The number of dopants per GB area is preferred instead of the number of dopants per volume because Ag dopants are predominately segregated to the GB region (Fig. 5.2.1a) and therefore the number of dopants per GB area would be more illustrative than the mole fraction of Ag. The GB area is calculated using Voronoi tessellation method.

5.2.4.2 Intragranular Dislocation Density

Dislocation Extraction Algorithm (DXA)[23] is used to identify all dislocations and to calculate the total dislocation length in deformed nanocrystalline samples. Examples of the identified dislocations are shown in Fig. 5.2.1b. Dislocations in GBs can also be detected by DXA, which leads to an unreasonably high initial dislocation density even before deformation. Only intragranular dislocations are considered here for the total dislocation length calculation because these dislocations

are responsible for intragranular dislocation entanglements and strain hardening. Intragranular dislocation density is calculated in four steps. In the first step, GB atoms are identified using the common neighbor analysis (CNA).[24] Specifically, the CNA algorithm is used to identify the local crystallographic order of each copper atom, i.e., atoms are identified as having FCC, hexagonal closed packed (HCP), body centered cubic (BCC). Atoms that do not have either of these local structures are labeled as defect atoms. As GB regions are comprised of defect Cu atoms and Ag atoms (since Ag atoms segregate to GBs), we use these two criteria to identify GB regions. In the second step, atoms identified as belonging to GBs are deleted. In the third step, the structures without GB atoms are analyzed by DXA, which calculates the total length of intragranular dislocations $l_{interior}$. In the last step, intragranular dislocation density ρ is calculated as $\rho = \frac{l_{interior}}{V_{interior}}$, where $V_{interior}$ is the total volume of the grain interiors. $V_{interior}$ is calculated as $(N - N_{GB})\times v_{Cu}$, where N is the total number of atoms in the system, N_{GB} is the number of deleted GB atoms, and v_{Cu} is the volume of a copper atom in pure FCC lattice. v_{Cu} is calculated by dividing the unit cell of a Cu FCC lattice by the number of atoms in unit cell.

5.2.4.3 Atomic local shear strain

To investigate deformation mechanisms and quantify plastic deformation, we calculate the atomic local shear strain.[25] Two atomic configurations are required to calculate atomic local shear strain, a current configuration and a reference configuration. Here the configuration of a deformed system is set as the current one and the initial configuration before deformation is set as the reference one. For each atom i in the system, its position relative to its neighbors changes after deformation. This position change can be represented as $\{d_{ji}^0\} \rightarrow \{d_{ji}\}, \forall j \in N_i^0$, where d_{ji}^0 and d_{ji} represent three-dimensional distance between atoms j and i in the reference configuration and current

configuration, respectively. j atom is one of the nearest neighbors of atom i, and N_i^0 is the total number of the nearest neighbors of atom i. A local transformation matrix $J_i = (\sum_{\forall j \in N_i^0} d_{ji}^{0T} d_{ji}^0)^{-1} (\sum_{\forall j \in N_i^0} d_{ji}^{0T} d_{ji})$ can be determined from d_{ji}^0 and d_{ji}, so that J_i minimizes the expression $\sum_{\forall j \in N_i^0} |d_{ji}^0 J_i - d_{ji}|^2$. A local strain tensor η_i is then calculated from J_i using the formula $\eta_i = \frac{1}{2}(J_i J_i^T - I)$. η_i is a very good approximation of the atomic-scale local deformation around atom i. Von Mises shear strain invariant is subsequently calculated from the local strain tensor as $\eta_i^{Mises} = \sqrt{\eta_{yz}^2 + \eta_{xz}^2 + \eta_{xy}^2 + \frac{(\eta_{yy}-\eta_{zz})^2 + (\eta_{xx}-\eta_{zz})^2 + (\eta_{xx}-\eta_{yy})^2}{6}}$. η_i^{Mises} is assigned to each atom and it is referred to as the atomic local shear strain. Analysis of the statistical distribution and geometrical distribution of atomic local shear strain is used in this paper to illustrate deformation mechanisms.

5.3 Results and Discussion

5.3.1 Microstructure

Figure 5.2.1a shows that almost all Ag dopants are located in the GB regions of Cu/Ag alloy, which is an immiscible binary alloy. The structure with Ag dopants segregated at GBs is more energetically stable than the structures with Ag precipitates in grain interiors of Cu matrix. In order to demonstrate the morphology and structures of GB complexions, cross-sectional view of Cu/Ag alloy with different concentrations is shown in Fig. 5.3.1. Specifically, Fig. 5.3.1a shows the cross-sectional view of Cu-Ag alloy with 15nm grain diameter and Ag concentration of 1.88 Ag atoms/nm^2 (0.55% of mole concentration). The GB between grains marked as G1 and G2 is a high-angle tilt GB. In this type of GB, Ag atoms are located at the cores of GB misfit dislocations and form an monolayer complexion of dopants. For a tilt GB, the high-energy sites of misfit dislocation cores are distributed periodically, and thus the Ag dopants are separated from each other by a nearly constant

distance. Such monolayer complexion of GB dopants has also been observed experimentally using high-angle annular dark field scanning transmission electron microscopy (HAADF-STEM) in other eutectic binary alloys with low dopant concentrations, such as Bi-doped bicrystal Cu.[8] However, previous observations of monolayer complexion in simulations and experiments have often been reported for high-symmetry GBs with ordered GB structures where high energy sites are distributed periodically. Here, we find local structures for both high-symmetry and general GBs. For general GBs (e.g., GB between G1 and G3 in Fig. 5.3.1a) Ag dopants are not evenly spaced as the location of high-energy sites in such GBs is relatively random.

When Ag concentration increases, Ag atoms are no longer isolated from each other. Instead additional Ag dopants accumulate around already incorporated Ag dopants (see Fig. 5.3.1a). Small Ag precipitates are thus formed at GBs. (Fig.5.3.1b) With further increase of Ag concentration, these precipitates have a strong tendency to grow along GBs, rather than into grain interiors. The isolated Ag precipitates gradually become connected to each other and form nanolayer complexions, which are several atomic layers (i.e., 1-3nm) thick. So far, the isolated Ag precipitates and nanolayer complexions are still regarded as part of the nc Cu GBs. They lack local crystalline structures and are not considered as a separate phase. It is also noteworthy that for general GBs we did not observe a discontinuous jump in GB thickness, whereas such discontinuity has been previously reported for high-symmetry GBs with ordered GB structures.[8] Instead, the thickness of general GB complexions increases gradually. This is because for high-symmetry GBs with ordered GB structures, the energies of GB sites are distributed discretely. Dopants will occupy the energy states of GB sites one by one, which leads to the discrete thickening at low dopants concentrations. For a general GB, however, GB structures are not ordered and energy states have a more random distribution. The energies states of GB sites are also continuously distributed. As a result, when Ag dopants fill the continuously distributed energy states, the thickness of the GB complexions increases gradually.

While Ag precipitates and nanolayer complexions are still components of nc Cu GBs, bulk Ag phase with FCC crystalline structures are observed when Ag concentration is above a certain concentration. This threshold concentration is around 50 Ag atoms/nm^2 (5.5% mole concentration for nc Cu/Ag alloy with 40nm average grain diameter). As is shown in Fig.5.3.1c, when C_{Ag} is as high as 223.7 Ag atoms/nm^2 (corresponding to 24.4% mole concentration), Ag atoms form wetting layers along some of the GBs. The morphology of wetting layers is similar to the morphology often observed in as-cast and cold-worked Cu/Ag hypoeutectic alloys.[12] When nanolayer GB complexions grow into wetting layers, the one interface of Cu GB with Ag dopants becomes two Cu/Ag interfaces between Cu grains and the newly formed Ag phase. First, it is important to point out that not all types of GB complexions transform into wetting layers. We ask what types of GBs make it easier to transform segregated dopants into nanolayer GB complexions. To answer this question we investigate the structures of the newly formed Cu/Ag interfaces. The atomic details of two major types of Cu/Ag interfaces are shown in Fig.5.3.1d and Fig.5.3.1e, which are cube-on-cube interfaces with $\{111\}_{\mathrm{Ag}}||\{111\}_{\mathrm{Cu}}$ habit plane and hetero-twin interfaces with $\{111\}_{\mathrm{Ag}}||\{111\}_{\mathrm{Cu}}$ habit plane, respectively. The cube-on-cube and hetero-twin interfaces are reported to be the predominant interfaces in the casted two-phase Cu/Ag alloys.[15,16,17] It can be reasonably expected that their energy is lower than general types of Cu/Ag interfaces. As a result, when a newly formed Ag phase in the Cu GB region is able to develop such interfaces, this Cu GB becomes preferable for formation of Ag wetting layers. Many defects, such as dislocations, stacking faults, and twins, are observed inside the newly formed Ag phases. Dislocations are nucleated during the MD equilibration and atomic steps at the interfaces are presented, which both relieve the interfacial stress due to lattice mismatch between Ag and Cu phases. The dislocation activity inside Ag layers changes orientation relations between Ag and Cu[16,17] enabling formation of cube-on-cube or twin interfaces between Ag and Cu phase.

Such interfacial dislocations and atomic steps have been reported for the cube-on-cube and hetero-twin interfaces observed in the as-cast Cu/Ag system in experiments. [15,16,17]

In addition to the structures and types of the Cu/Ag interfaces, another important question is why the newly formed Ag phase has a shape of wetting layer, instead of a spherical one since the spherical shape minimizes the Cu/Ag interfacial area. This question can also be explained by the low interface energies of cube-on-cube and hetero-twin interfaces. Even though a Ag phase with isotropic dimensions can reduce the interfacial area, the total energy is high because the interface is composed of segments of high-energy general types of Cu/Ag interfaces. Therefore, the Ag phase has a tendency to maximize the area of cube-on-cube and hetero-twin interfaces, which leads to the layered morphology. The layered structures with predominately cube-on-cube and hetero-twin interfaces have been widely reported for casted Cu/Ag alloys. [15,16]

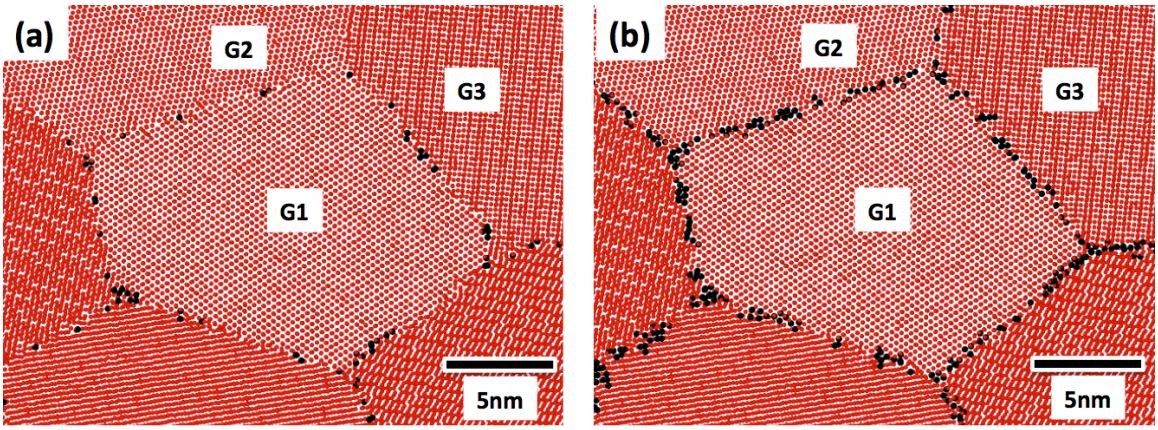

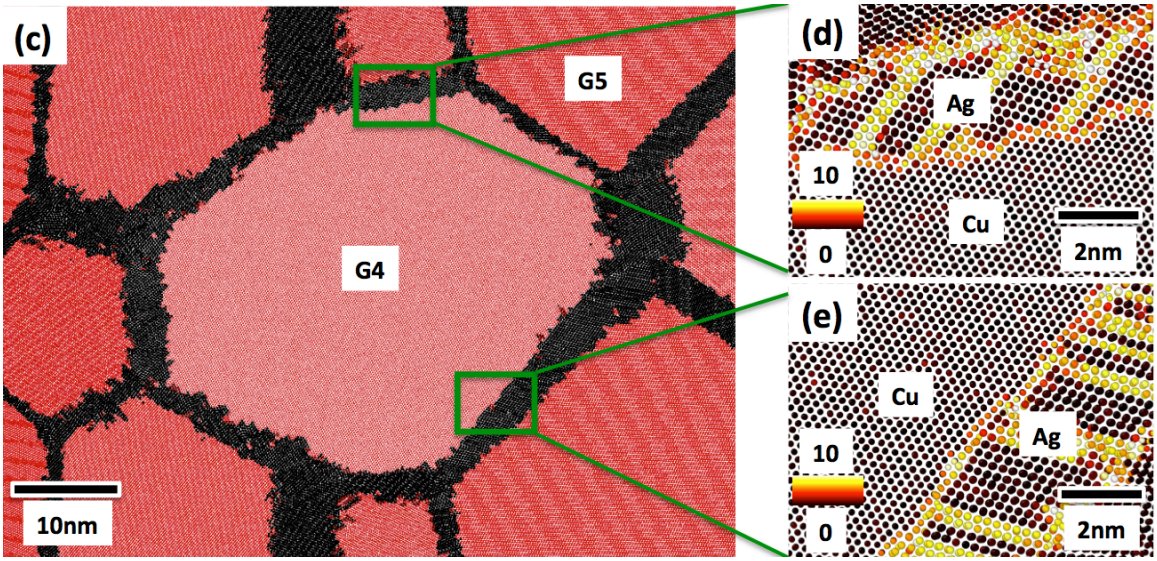

Figure 5.3.1 *Cross-sectional view of Cu-Ag microstructures with different Ag concentrations. (a) Grain diameter and Ag concentration are 15nm and 1.88 Ag atoms/nm², respectively; (b) Grain diameter and Ag concentration are 15nm and 8.35 Ag atoms/nm², respectively;(c) Grain diameter and Ag concentration are 40nm and 223.7 Ag atoms/nm², respectively; (d) and (e) are two enlarged local structures of regions shown in (c). These structures have cube-on-cube and hetero-twin Cu/Ag interfaces, respectively. In (a)-(c), red atoms are Cu and black atoms are Ag. In (d) and (e), atoms are colored by the centrosymmetry parameter. When the centrosymmetry parameter of an atom is close to 0, the atom has FCC local structure, while a larger centrosymmetry parameter indicates defects of dislocation cores, stacking faults, twins and interfaces. Ag atoms are also visualized to be slightly larger than Cu atoms.*

GB energy is calculated using the formula $\frac{E_{tot}-e_{Ag}\times N_{Ag}-e_{Cu}\times N_{Cu}}{A}$ for Cu/Ag alloys, where E_{tot} is the total energy of the system, e_{Ag} is the energy of one Ag atom in perfect Ag crystals (the cohesive energy), N_{Ag} is the number of Ag atoms in the system, e_{Cu} is the energy of one Cu atom in perfect Cu crystals, N_{Cu} is the number of Cu atoms in the system, and A is the total area of GBs in the

system. The calculated GB energy is plotted as a function of Ag concentration in Fig. 5.3.2. GB energies are calculated only for Ag-doped nc Cu GB below threshold concentration when no bulk Ag phases are formed. The GB energy first decreases and then increases with an increase in Ag concentration. The initial decrease is due to the fact that there are sites at Cu GBs with sufficiently high local energies so that this energy will decrease if Ag dopants are segregated there. Such sites include the ones with relatively large GB free volume and because Ag atoms have larger volume than Cu atoms, filling the sites with Ag dopants may relieve the tensile stress of these sites. However, there are other, lower-energy, sites at GBs that are not able reduce their energy further by accepting Ag dopants. When all the preferable GB sites have been filled by Ag dopants, Ag atoms begin to fill other GB sites thereby increasing the local energy. One should remember that these "other" GB sites are still more energetically favorable than adding Ag to the crystalline grain interiors. After the critical concentration around 10-15 Ag atoms/nm^2, the GB energy begins to increase. The critical concentrations are close for different grain sizes if we use the concentration units of number of Ag atoms per GB area. However, the critical mole fractions for different grain sizes are different since the GB densities are different. The critical mole concentration for 5nm grain-size sample is 14%, for 15nm grain-size sample is 3.5%, and for 40nm grain-size sample is 1.2%.

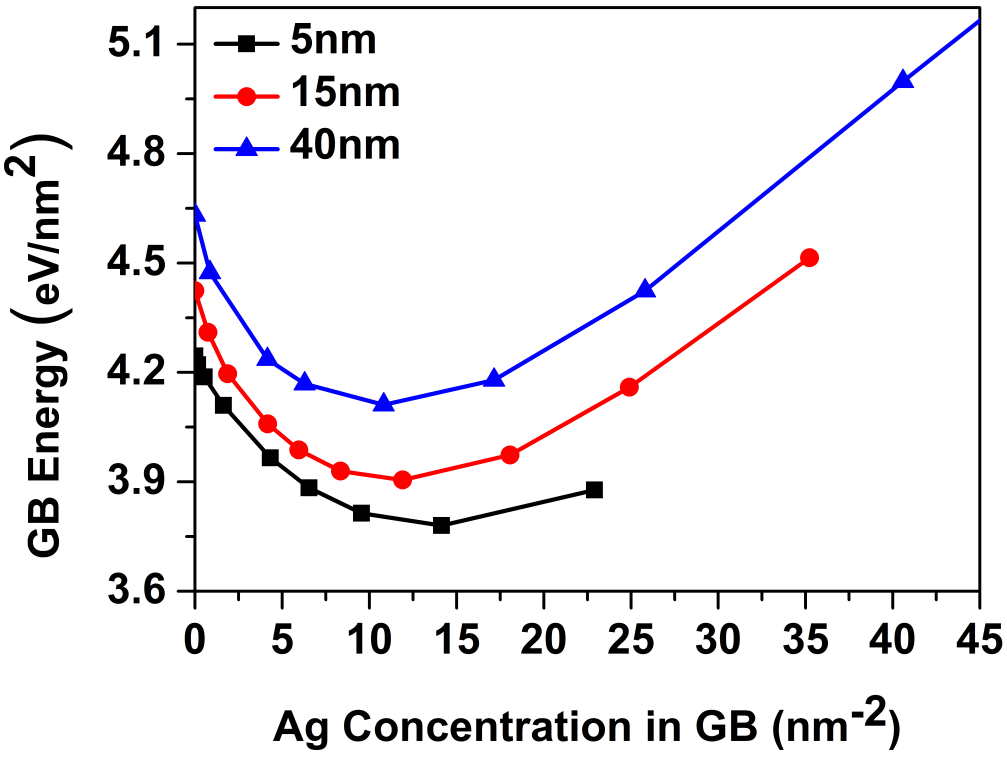

Figure 5.3.2 *Dependence of GB energy on Ag concentrations when average grain diameters are 5nm, 15nm, and 40nm.*

5.3.2 Deformation Mechanism

5.3.2.1 Pure Nanocrystalline Cu

We now turn to the questions of how Ag dopants influence the mechanical properties and deformation mechanisms of nc Cu/Ag alloys. Before analyzing the Cu-Ag alloy, it is instructive to briefly discuss mechanical response of pure nc Cu. Figure 5.3.3 shows a cross-sectional view of such sample with grain diameter of 40nm. Atoms are colored by the values of the atomic local shear strain η_i. Figures 5.3.3a and 5.3.3b correspond to samples deformed to 2% and 15% engineering strain, respectively. In both cases, the reference configuration is one with zero strain.

Yielding takes place at the engineering strain of 2.8% and this is when the first dislocations are nucleated As is shown in Fig. 5.3.3a, before yielding the deformation is confined to GB regions. In this case, there is no plastic deformation in grain interior. In Fig. 5.3.3b (after yielding), networks of bright lines, which represent dislocations in grain interiors, which dislocations mediate plastic deformation at this strain level.

In order to identify and quantify different deformation mechanisms, we analyze the statistical distribution of the values of the η_i, as shown in Fig. 5.3.3c and Fig. 5.3.3d. Since the values of the η_i represent the degrees of local deformations, different peak positions in Fig. 5.3.3c and Fig. 5.3.3d correspond to specific deformation mechanisms. Fig. 5.3.3c shows the statistical distributions of the values of the η_i in grain interiors at 2% and 15% engineering strains. One of the most pronounced differences between the distributions at 2% and 15% engineering strains is that the 2%-strain curve has one peak and the 15%-strain curve has two peaks. The second peak of the 15%-strain curve corresponds to dislocation-mediated deformation, which has not yet occurred at 2% engineering strain. The first peaks of both 2%-strain and 15%-strain curves correspond to the elastic deformation of the grain interior atoms. Another noticeable difference between the 2%-strain and 15%-strain curves for grain interior atoms is that the average strain values of the first peak at 15% engineering strain is larger than that at 2% engineering strain, which is because the former has larger elastic deformation than the latter.

Interestingly, similar distributions of values of the η_i are also observed for GB regions (Fig. 5.3.3d). Before yielding, there exists only one peak of strain, while after yielding, another peak appears (Fig. 5.3.3d). The first peak of both the 2%-strain and 15%-strain curves for GB regions correspond to the combination of elastic deformation, and GB sliding. Here the GB sliding means that two neighboring grains move in the opposite directions relative to each other, along the GB plane that separates these two grains. We hypothesize that the second peak is due to dislocation

activities because it is formed only after yielding. Though dislocations-mediated plasticity is often considered to occur mainly in grain interiors, GB regions can also be deformed by dislocations through various dislocation-GB interaction mechanisms including dislocation nucleation at GBs, dislocation gliding along GBs, and dislocation transmission across GBs, all of which may lead to local deformations in GB regions. The magnitude of the local deformation at GBs caused by dislocation activities is determined by the residual burgers vectors left by these dislocations at GBs.

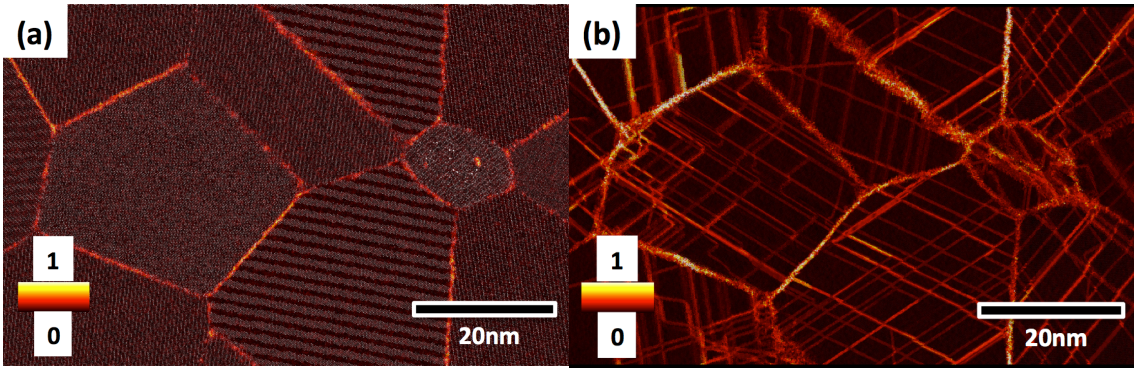

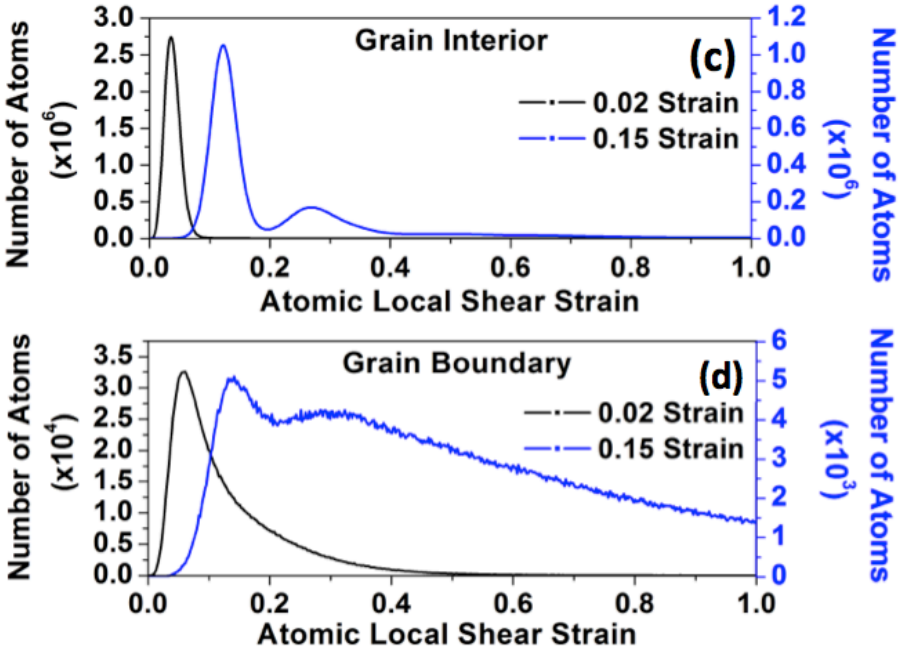

Figure 5.3.3 *Cross-sectional view of pure nc Cu with grain diameter 40nm when the engineering strain of tension is 2% (a), and 15% (b). In (a) and (b), all the atoms are colored by the values of the calculated η_i; (c) and (d) are statistical distributions of values of the η_i in grain interiors and GBs.*

It has been reported that GB sliding can be a dominating deformation mechanism in nc Cu in the small grain size regime. [4,5,6] In order to quantify the GB sliding, we introduce GB sliding index which is defined as the difference between the position of the first-peak in the distribution of η_i in GB regions (the first peak in the 0.15 strain curve in Fig. 5.3.3d) and the position of the first-peak position of the grain interior region (first peak of 0.15 strain curve in Fig. 5.3.3c). Because the first-peak position of GBs reflects both elastic deformation and GB sliding, while the first-peak position of the grain interiors involves only elastic deformation, the GB sliding index will qualitatively represent the magnitude of GB sliding. The index is not a quantitative measure because of the possible differences between elastic constants in the GBs and in grain interiors. Nevertheless, the larger the GB sliding index is, the more GB sliding takes place.

The dependence of GB sliding index on grain diameters is shown in Fig. 5.3.4a, which demonstrates that GB sliding becomes more significant when the grain size decreases. In nc metals, more pronounced GB sliding is expected to lead to a decrease of the flow strength, if GB sliding is the dominant mode of deformation. By decreasing the grain size, the flow stress first increases and then decreases,(Fig. 5.3.4b) which is due to the crossover of dominating deformation mechanisms from dislocation-mediated hardening to GB sliding-mediated softening.

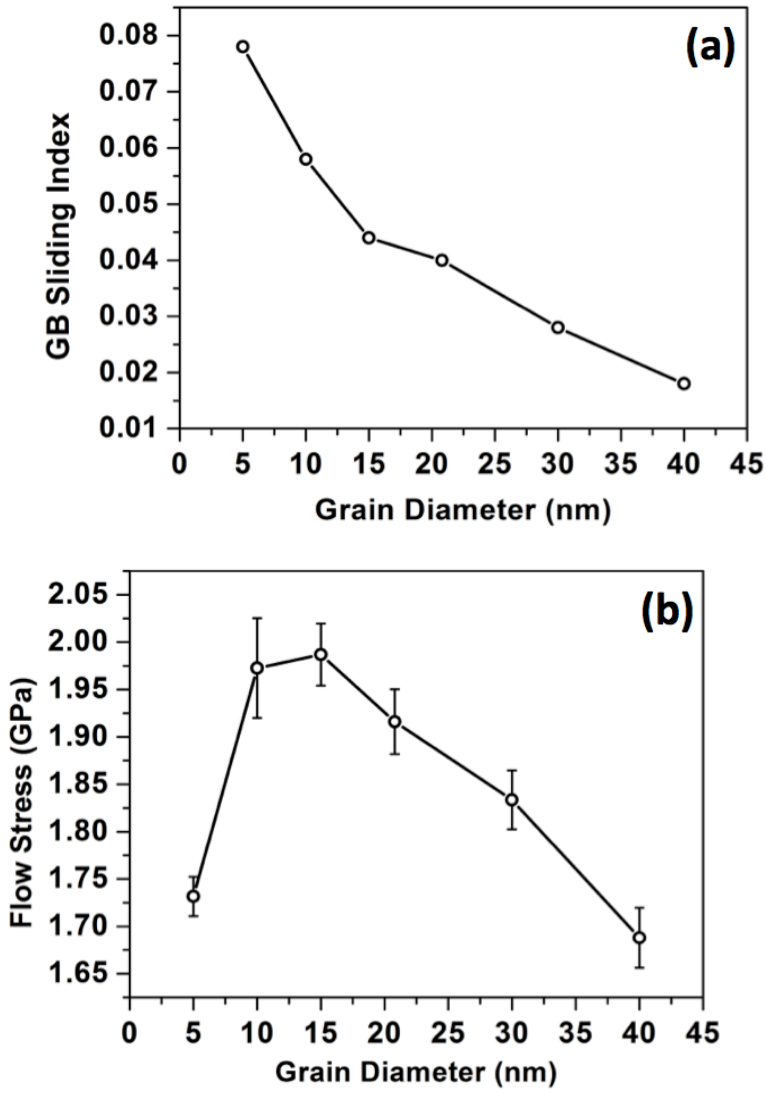

Figure 5.3.4 *Dependence of GB sliding index (a), and flow stress (b) on average grain diameters. For (a), and (b), the engineering strain is 15%.*

3.2.2 Ag Doped-Cu Alloy

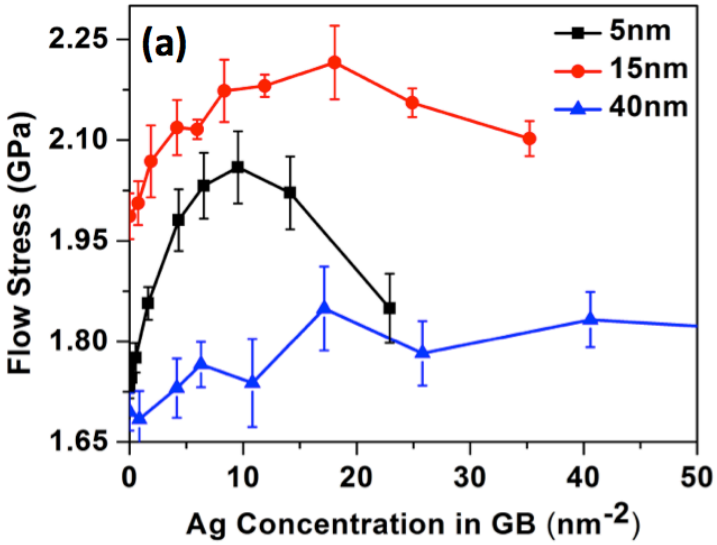
(a)
5nm
15nm
40nm
Flow Stress (GPa)
2.25
2.10
1.95
1.80
1.65
0
10
20
30
40
50
Ag Concentration in GB (nm-2)

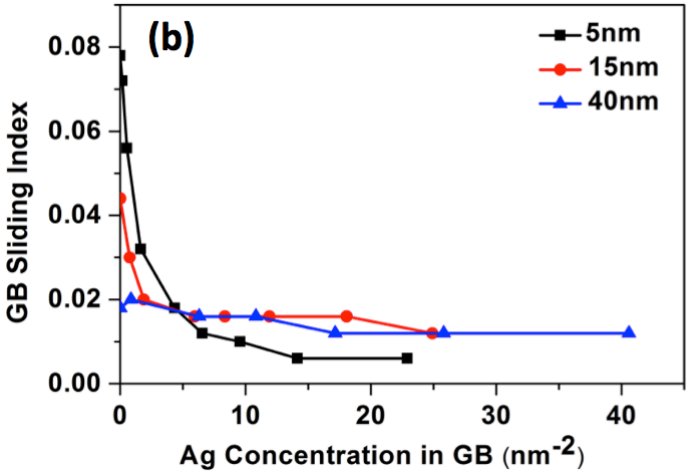
(b)
5nm
15nm
40nm
GB Sliding Index
0.08
0.06
0.04
0.02
0.00
0
10
20
30
40
Ag Concentration in GB (nm-2)

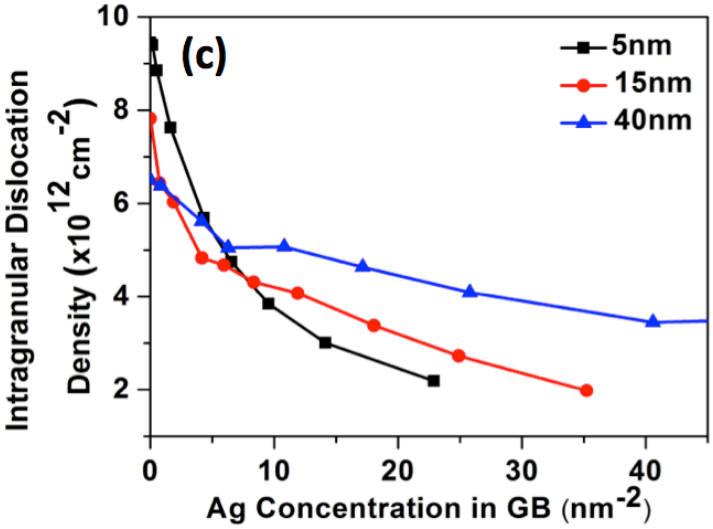
(c)
5nm
15nm
40nm
Intragranular Dislocation Density (x10 12 cm -2)
10
8
6
4
2
0
10
20
30
40
Ag Concentration in GB (nm-2)

Figure 5.3.5. *Dependence of GB sliding index (a), intragranular dislocation density (b), and flow stress (c) on Ag concentrations when the average grain diameters are 5, 15, and 40nm. For (a), (b) and (c), the engineering strain is 15%.*

We now consider the effect of dopants on mechanical properties and deformation mechanisms in Cu/Ag alloys. In Fig. 5.3.5a we show the dependence of flow stress on concentration of Ag for nc Cu/Ag alloys with average grain diameters of 5nm, 15nm, and 40nm. Here, only Ag concentrations below the roughening concentration are considered, which means that all samples are nc Cu with Ag dopants at GBs, instead of Cu/Ag bi-phase alloys. For the 5nm and 15nm grain diameter samples, flow stress first increases and then decreases with the increase in Ag concentration, while for the 40nm grain diameter sample, the flow stress is less sensitive to Ag concentration and the changes in the flow stress are comparable with the error bars.

In order to understand the above effects of Ag on the flow stress, we analyze changes in the amount of GB sliding and dislocation-mediated plasticity with Ag concentration (Figs. 5.3.5b and 5.3.5c). Dependence of GB sliding index on Ag concentration have two major features, as shown in Fig. 5.3.5b. The first one is that GB sliding index decreases monotonically and gradually reaches a plateau when Ag concentration increases. This feature indicates that GB sliding becomes more difficult when Ag concentration increases in a small concentration regime (C_{Ag}<5-10 $\mathrm{Ag/nm^2}$). In the large concentration regime (C_{Ag}>5-10 $\mathrm{Ag/nm^2}$), the strength of GBs reaches a plateau and the effects of Ag dopants are negligible. The second feature of Fig. 5.3.5b is that GB sliding index is not sensitive to Ag concentration when grain size is 40nm, even in the small concentration regime. The reason is that when the grain diameter is as large as 40nm, the deformation due to GB sliding is already negligible as compared to that when the grain diameter is 5nm (Fig. 5.3.4a). In this case, Ag

dopants' effect on mitigating GB sliding will be small, which leads to the lack of sensitivity of GB sliding to Ag dopants.

The dependence of intragranular dislocation densities on Ag dopants is shown in Fig. 5.3.5c. Since Ag dopants segregate to GBs, they will naturally influence GB sliding. Surprisingly, we observe that dislocation activities inside grains are also significantly influenced by GB dopants. As is shown in Fig. 5.3.5c, intragranular dislocation density decreases with the increase of Ag concentration, which indicates a decrease in the flow stress of the grain interior. It is expected that a crystal with larger intragranular dislocation densities will have a larger flow stress because of the dislocation interactions, if other deformation mechanisms are not active. Our finding suggests that even though Ag dopants are located in GB regions, they are able to reduce intragranular dislocation densities and thus soften grain interior during plastic deformation. Ag-doped Cu GBs can influence the dislocation densities of Cu grains both directly and indirectly. Ag dopants can influence dislocation densities directly by influencing dislocation-GB interactions. The dislocation-GB interactions may include the following phenomena: dislocation nucleation at GBs, dislocation gliding within confined grains (with ends of dislocation lines remaining on GBs when the dislocation sweep through a grain), and dislocations' transition across GBs. For instance, Ag dopants may alter GB energy[9] and thus influence the required stress for dislocation nucleation. Ag dopants may also change the Orowan stress to move a dislocation whose two ends are connected with GBs, and to overcome the resistance from GBs at the two ends. These direct effects of Ag dopants on dislocation-GB interactions will be all reflected in intragranular dislocation densities. The indirect effect of Ag dopants means that Ag dopants can influence GB sliding and thus change the total contribution of dislocation-mediated plasticity. In addition to the direct and indirect effects of Ag dopants through changing dislocation-GB interactions, dislocation-dislocation interactions also influence dislocation densities, which are anticipated not (or negligibly) influenced by Ag dopants. Since these various types of mechanisms

coexist to influence dislocation densities, it is challenging to isolate the contributions of each mechanism from the others. Further research is needed to investigate the effects of Ag dopants on each of these dislocation activities using more simplified systems. For instance, we are studying the influence of Ag dopants on the Orowan stress in a layered system, which is the stress required to overcome the GB resistance to dislocation motions.[26]

It is also notable that intragranular dislocation density becomes less sensitive to Ag concentration when grain diameter is as large as 40nm. The reason is that when grain size increases, the volume fraction of grain interior region increases and the volume fraction of the GB region decreases. In this case, the dislocation-GB interactions are less important than the dislocation-dislocation interactions which both control dislocation densities. As a result, when the grain diameter is 40nm, dislocation densities are less sensitive to the Ag concentration which only influences the GB-dislocation interactions.

We have demonstrated that an increase in Ag concentration, similar to an increase in grain sizes, will harden GBs and soften grain interiors. The competition of GB hardening and grain interior softening leads to a critical dopant concentration that maximizes the flow stress (Fig. 5.3.5a). In the large Ag concentration regime, grain interior hardening dominates, while in the small Ag concentration regime, GB softening dominates. The discoveries of the crossover of dominating deformation mechanisms due to introduction of Ag dopants, and the existence of an optimum concentration that maximizes hardness provide guidance to GB engineering of nc Cu/Ag alloy. In addition, when grain size is 40nm or larger, the flow stress is not as sensitive to Ag concentration as in the smaller grain size regime. The reason is that both GB sliding and intragranular dislocation activities are less influenced by Ag concentration in the large grain size regime, as is shown in Figs. 5.3.5b and 5.3.5c.

5.4 Conclusions

The microstructures and mechanical properties of Cu/Ag alloys have been discussed in this paper. Below the roughening concentration, Ag dopants at GBs of Cu/Ag alloys evolve from monolayer complexions to nanolayer complexions. Above the roughening concentration, a crystalline Ag bulk phase is observed in a form of wetting layer. Most of the interfaces between the Ag phase and the Cu grains are cube-on-cube and hetero-twin interfaces. The flow stress of the nc Cu/Ag alloys first increases and then decreases with an increase in Ag concentration, due to the transition of dominating deformation mechanisms from Ag dopants-mediated GB hardening to Ag dopants-mediated grain interior softening. This Ag effects on flow stress and deformation mechanisms are not significant when the average grain size is as large as 40nm.

Reference

1 C.C. Koch,: Optimization of strength and ductility in nanocrystalline and ultrafine grained metals. Scripta Materialia 49, 657-662 (2003)

2 M.A. Meyers , A. Mishra, D.J. Benson, Mechanical properties of nanocrystalline materials. Progress in Materials Science 51, 427-556 (2006)

3 L. Lu, M. L. Sui, K. Lu,: Superplastic Extensibility of Nanocrystalline Copper at Room Temperature. Science, 287, 1463-1466 (2000)

4 J. Schiotz, K. W. Jacobsen,: A Maximum in the Strength of Nanocrystalline Copper Science 301, 1357-1359 (2003).

5 J. Schiotz, F. D. Di Tolla, K. W. Jacobsen, : Softening of nanocrystalline metals at very small grain sizes. Nature 391, 561-563 (1998).

6 A. Li, I, Szlufarska,: How grain size controls friction and wear in nanocrystalline metals. Phys. Rev. B 92, 075418 (2015).

7 Y. Sakai, K. Inoue, T. Asano, H. Wada, H. Maeda,: Development of high-strength, high-conductivity Cu–Ag alloys for high-field pulsed magnet use. Applied Physics Letters 59, 2965 (1991).

8 P. R. Cantwell, M. Tang, S. J. Dillon, J. Luo, G. S. Rohrer, M. P. Harmer, : Grain boundary complexions. Acta Materialia 62, 1-48 (2014).

9 N.Q. Vo, J. Scha¨fer, R.S. Averback,a K. Albe,b Y. Ashkenazya, P. Bellon,: Scripta Materialia 65, 660-663 (2011).

10 T. Chookajorn, H. A. Murdoch, C. A. Schuh,: Design of Stable Nanocrystalline Alloys. Science 337, 951-4 (2012).

11 G. Bao, Y. Xu, L. Huang, X. Lu, L. Zhang, Y. Fang, L. Meng, J. Liu,: Strengthening Effect of Ag Precipitates in Cu–Ag Alloys: A Quantitative Approach. Materials Research Letters 1, 37-42 (2016).

12 Y.Z. Tian, Z.F. Zhang,: Microstructures and tensile deformation behavior of Cu–16 wt.%Ag binary alloy. Materials Science and Engineering A 508, 209-213 (2009)

13 Shipeng Shu, Xuan Zhang, Pascal Bellon, Robert S. Averback,: Non-equilibrium Grain Boundary Wetting in Cu–Ag Alloys Containing W Nanoparticles. Mater. Res. Lett. 1, 22-26 (2016)

14 S.J. Zheng, J. Wang, J.S. Carpenter, W.M. Mook, P.O. Dickerson, N.A. Mara, I.J. Beyerlein,: Plastic instability mechanisms in bimetallic nanolayered composites, Acta Materialia 79, 282-291 (2014).

15 Y.Z. Tian, Z.F. Zhang,: Bulk eutectic Cu-Ag alloys with abundant twin boundaries, Scripta Materialia 66, 65-68 (2012).

16 B.P. Eftink, A. Li, I. Szlufarska, and I.M. Robertson, : Interface mediated mechanisms of plastic strain recovery in a AgCu alloy. Submitted (2016).

17 B.P. Eftink, A. Li, I. Szlufarska, N.A. Mara, I.M. Robertson,: Deformation response of AgCu interfaces investigated by in situ and ex situ TEM straining. In preparation (2016).

18 T. Frolov, S. V. Divinski, M. Asta, and Y. Mishin,: Effect of Interface Phase Transformations on Diffusion and Segregation in High-Angle Grain Boundaries. PHYSICAL REVIEW LETTERS 110, 255502 (2013).

19 S. Plimpton, : Fast Parallel Algorithms for Short-Range Molecular Dynamics. J Comput Phys 117, 1-19 (1995).

20 Y. Mishin, M. J. Mehl, D. A. Papaconstantopoulos, A. F. Voter, J. D. Kress,: Structural stability and lattice defects in copper: Ab initio, tight-binding, and embedded-atom calculations.Physical Review B 63, 224106 (2001).

21 K. M. Youssef, R. O. Scattergood, K. L. Murty, C. C. Koch,: "Ultratough Nanocrystalline Copper With A Narrow Grain Size Distribution. Applied Physics Letters 85, 925-931 (2004).

22 B. Sadigh, P. Erhart, A. Stukowski, A. Caro, E. Martinez, L. Zepeda-Ruiz,: Scalable parallel Monte Carlo algorithm for atomistic simulations of precipitation in alloys. PHYSICAL REVIEW B 85, 184203 (2012).

23 A. Stukowski, K. Albe,: Extracting dislocations and non-dislocation crystal defects from atomistic simulation data. Modelling Simul. Mater. Sci. Eng. 18, 085001 (2010).

24 J. D. Honeycutt, H. C. Andersen,: Molecular dynamics study of melting and freezing of small Lennard-Jones clusters. J. Phys. Chem. 91, 4950-4963 (1987).

25 F. Shimizu, S. Ogata, J. Li,: Theory of Shear Banding in Metallic Glasses and Molecular Dynamics Calculations. Materials Transactions 48, 2923-2927 (2007).

26 A. Li, I. Szlufarska,: Confined layer slip of threading dislocations in nanolayer Cu doped with Ag. In preparation (2016).

Chapter 6 Interface mediated mechanisms of plastic strain recovery in a AgCu alloy

Contributions

This Chapter discusses results of combined MD simulations and experiments. Experiments were conducted by Dr. B.P. Eftink from University of Illinois Urbana-Champaign and Prof. I.M. Robertson from University of Wisconsin - Madison. Dr. Eftink and Prof. Robertson have also written text in this chapter that describes experimental results. I provided comments and edits on the experimental sections. I wrote sections describing results of MD simulations and Prof. Szlufarska helped edit these sections. Methods and discussion sections were written together with the experimental collaborators.

6.1 Introduction

High interface density materials have shown favorable properties in addition to high mechanical strength such as corrosion resistance, wear resistance, irradiation tolerance, and high electrical conductivity [1-6]. A fundamental understanding of the relationships between synthesis of materials with a high density of interfaces, the structure of those interfaces, and the resultant properties provides an avenue to guide material design. The AgCu eutectic system is a model material system for studying the dependence of the deformation mode and the transfer of strain across FCC/FCC interfaces as the interface can have either a cube-on-cube or coherent twin orientation relationship between the Ag and Cu layers with $\{111\}_{\mathrm{Ag}}||\{111\}_{\mathrm{Cu}}$ habit planes or incoherent twin interfaces with $\{\bar{3}13\}_{\mathrm{Ag}}||\{\bar{1}12\}_{\mathrm{Cu}}$ habit planes [7-9]. In directionally solidified material, the percentage of cube-on-cube versus incoherent twin interfaces decreases with decreasing bilayer thickness, which is

controlled by processing conditions. The interface type has important implications on the overall mechanical response of the material as the interaction of dislocations, both perfect and partial, is dependent on it [7]. For example, it has been found that the cube-on-cube interface permits transmission of deformation twins across it whereas the incoherent and coherent twin interfaces do not [7, 10, 11]. Furthermore, for AgCu eutectic loaded parallel to the incoherent twin interfaces, along the $[101]_{Ag}||[110]_{Cu}$ growth direction, in material with a bilayer thickness of 500 nm, which has a preponderance of incoherent twin interfaces, a significant plastic strain recovery has been observed following loading [12]. The magnitude of the plastic strain recovery decreased with increasing strain; 3.2 % plastic strain recovery was observed at a true strain of 9.3 % and no recovery was reported in samples loaded to a true strain of 21.9 %. Kingstedt *et al*. reported that the degree of recovery decreased with a change in the loading orientation with respect to the interface normal [12]. For example, loading 90° to $[101]_{Ag}||[110]_{Cu}$ at a strain rate of 10^3 s^{-1} to a true strain of 15.4 % resulted in a plastic strain recovery of 0.6 %. Figure 6.1.1 shows the stress-strain curves for the 500 nm bilayer thick eutectic loaded at different orientations, the true strains applied by the split-Hopkinson pressure bar compression (SHPB) are marked by the closed symbols while the true strains measured post compression are marked by the open symbols [12]. No plastic recovery was found in samples loaded quasi-statically along $[101]_{Ag}||[110]_{Cu}$ which is the growth direction and parallel to the interfaces. The dependence of the magnitude of the plastic recovery on the interface type, loading direction with respect to the interface, and the strain is summarized in Table 6.1.1. Kingstedt *et al*. proposed that a number of mechanisms and microstructural features acted collaboratively in the plastic recovery, although no definitive mechanism was identified [12]. They did, however, eliminate temperature increase as a possible mechanism as it was determined to be on the order of 10-12 degrees. Herein the microstructural state of the materials whose response is shown in Figure 6.1.1 is determined. Kingstedt *et al.* also reported that no measurable plastic strain

recovery occurs as the bilayer thickness increases and the majority of interfaces transitions to cube-on-cube [12].

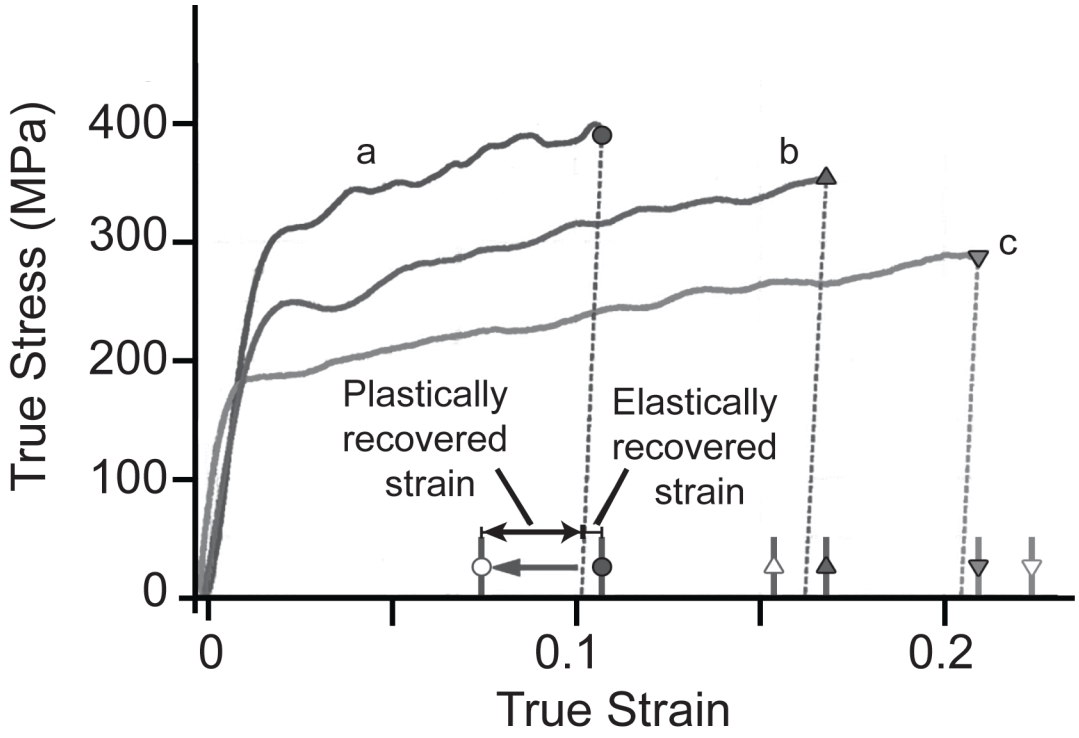

Figure 6.1.1 *Stress-strain curves for directionally solidified AgCu eutectic loaded with split-Hopkinson pressure bar (SHPB) at: a 0°; b 45° and c 90° to the growth direction. Closed symbols mark strain applied by SHPB, and open symbols mark strain measured from the recovered samples. Adapted from Kingstedt et al.[12].*

Table 6.1.1 *Compressive strain levels and strain recovered. Samples for tests 1, 2 and 6 were taken from the same directionally solidified rod and those for the other tests from a second rod. [12].*

Sample	Angle between load and $[101]_{Ag}\|\|[110]_{Cu}$ growth direction	Strain rate (s^{-1})	Strain (%)	Strain recovered (%)Elastic	Strain recovered (%) Plastic

1	0°	10^3	9.3	0.4	3.2
2 (repeated loading)	0°	10^3	10.6	0.4	2.7
	0°	10^3	15.1	0.4	2.1
	0°	10^3	17.0	0.4	1.5
	0°	10^3	21.9	0.4	0
3	0°	10^3	9.9	0.4	1.5
4	0°	10^3	6.8	0.4	1.4
5 (multiple samples)	0°	10^{-3}	2.5-10.5	0.5	0.0
6	90°	10^3	15.4	0.5	0.6

Plastic strain recovery has been found experimentally following room temperature deformation to a strain of 2 % in Al and Au thin films with 65 and 50 nanometer grain sizes, respectively [13]. However, for the recovery in Au to be observed, the specimens had to be heated to 210 °C. The amount of recovery in Al and Au was 0.33 % and 0.35 % strain, respectively [13]. Al films with a grain size of 180 nm did not exhibit recovery, even after annealing for 30 min at 220 °C. Molecular dynamics (MD) computer simulations have been performed to explain the recovery observed in Al and Au and it was attributed to dislocation retraction into the grain boundary along with grain boundary sliding [14]. Strain recovery has also been observed in a penta-twinned Ag nanowire strained *in situ* in a transmission electron microscope (TEM) [15]. The recovery was attributed to the

leading partial dislocations, which had been blocked by the twin boundaries, retracting to the nucleation site of the free surface on unloading; this mechanism was supported by the results of MD simulations [15]. An MD study of the deformation processes in a multilayered system comprised of both 2 and 8 nm-thick Cu and Ag layers with a cube-on-cube orientation relationship and $(111)_{\mathrm{Ag}}||(111)_{\mathrm{Cu}}$ interface habit planes showed that straining in tension along $[111]$ to a strain of 4% was carried by deformation twinning [16]. Complete recovery of the plastic strain was reported on unloading. However, since volume relaxation along the two spatial directions perpendicular to the loading axis was not allowed, the simulations did not account for the Poisson effect and it is unclear if such a constraint on volume could influence the plastic strain recovery mechanism. Furthermore, a measurable level of plastic strain recovery was not observed experimentally in a AgCu eutectic alloy in which the majority of the interfaces were cube-on-cube [12].

In this manuscript, MD computer simulations of the deformation and subsequent plastic recovery of Ag and Cu layers with incoherent twin and cube-on-cube interfaces are compared with the microstructure in samples that exhibited plastic strain recovery; the samples studied were provided by Kingstedt *et al*. and the pertinent results are documented in Fig. 6.1.1 and Table 6.1.1 [12]. It will be shown that the essential features of the deformation processes observed experimentally are captured fully by the MD simulations. Specifically and importantly, a rotation of the incoherent twin interface was observed both experimentally and in the simulations despite the differences in test conditions. The capturing of this unique signature of the deformation response implies that similar mechanisms are active in the simulations and the experiments. Consequently, it is possible to use the simulations to reveal characteristics of the plastic strain recovery that are not accessible experimentally. The dynamics of plastic strain recovery was found to involve dislocation interactions with and accommodation within the interface, which is driven by the stress buildup at and a reduction of the energy of the interface. This mechanism will be shown to explain the

dependence of the plastic strain recovery on the interface type as well as the loading direction with respect to the interface habit plane. Dislocation-dislocation interactions result in the formation of tangled structures or cell walls and, consequently, these dislocations cannot participate in supporting further strain. Similarly, the trapping of the dislocations will prohibit them from participating in the plastic strain recovery. It will be shown that dislocation tangles and even the formation of cell walls are more prevalent with increasing strain, which explains the dependence of the magnitude of the plastic strain recovery on the strain.

6.2 Methods

6.2.1 Experiments

The material used for this study was a directionally solidified AgCu eutectic alloy, which was processed to achieve a bilayer thickness of 500 nm with over 66% of the interfaces being of the incoherent twin type and the remainder being of the cube-on-cube type [7]. The samples were subjected to either SHPB at a strain rate of 10^3 s^{-1} or quasi-static compression at a strain rate of 10^{-3} s^{-1} using a load frame (the mechanical response of the compression tests are reported elsewhere [12, 17]); the key findings from these compression tests are summarized in Table 6.1.1. In Table 6.1.1, samples designated 1, 2 and 6 were prepared from one directionally solidified rod and samples 3, 4, and 5 were prepared from another; this was done to ensure the effect was not unique to one rod. To achieve high levels of strain and to follow the evolution of the recovery of plastic strain as a function of strain one sample was loaded, unloaded and recovered and then reloaded repeatedly.

Electron microscopy analysis was conducted on a Tecnai TF-30 TEM operating at 300 keV. Samples for TEM analysis were produced by using either a focused ion beam machining technique using a Zeiss Auriga with a final milling voltage of 2.0 keV or conventional ion milling preparation

of 3 mm disks using a Fischione 1050 ion mill with a final milling voltage of 1.0 keV. With both TEM sample preparation techniques, the sample normal was near the growth axis of the AgCu rod.

6.2.2 Molecular Dynamics Simulations

MD simulations were performed using the LAMMPS software [18] and embedded atom force-field was employed to describe Ag-Ag, Ag-Cu, and Cu-Cu interactions [19]. The dislocation density was calculated using a dislocation extraction algorithm (DXA) [20]. All visualizations were conducted using OVITO [21]. The system configurations, shown in Fig. 6.2.1, mimic the multilayer structure of the Ag/Cu alloy used in the experiments. Periodic boundary conditions were applied along the x-, y- and z-directions, as defined in Fig. 6.2.1. Two Ag and two Cu layers alternate along the y-direction and are infinite along the x- and z-directions.

Two types of interfaces were considered in the simulations, incoherent twin interfaces with $(\bar{3}13)_{\mathrm{Ag}}||(\bar{1}12)_{\mathrm{Cu}}$ habit planes and cube-on-cube interfaces with $(\bar{1}11)_{\mathrm{Ag}}||(\bar{1}11)_{\mathrm{Cu}}$ habit planes. For AgCu alloys with incoherent twin interfaces, the Ag and Cu layers have different crystallographic orientations, as shown in Fig. 6.2.1(a). The dimensions of each of the Ag and Cu layers were 38 nm in the x-direction and 35 nm in the z-direction. In the y-direction the Ag and Cu layers were 41 nm and 20 nm thick, respectively. For AgCu alloys with cube-on-cube interfaces, the Ag and Cu layers, as shown in Fig. 6.2.1(b), have the same crystallographic orientation. Each of the Ag and Cu layers were 36 nm in the x-direction and 35 nm in the z-direction. The Ag and Cu layers were 40 nm and 20 nm thick in the y-direction, respectively. Although these layer thicknesses are an order of magnitude smaller than the material used in the experiments, the 2:1 ratio of the thickness of Ag to Cu is consistent.

In order to construct the nanolayered structures, first single crystal Ag and Cu systems were generated. These single crystal systems were equilibrated for 1 ns at 5 K and 0 GPa using the

Berendsen thermostat and barostat. Equilibrated Ag and Cu layers were then joined to form nanolayers stacked along the y-direction. Each sample had four Ag/Cu interfaces and consisted of over 10 million atoms. The energy of the as-stacked Ag/Cu interfaces was minimized using the conjugate gradient algorithm and then relaxed at 300 K and 0 GPa for another 1 ns.

For both systems, the compression tests were conducted by applying strain uniaxially along the z-direction at a strain rate of $5\times10^{8}\ s^{-1}$. The strain was applied by alternately deforming the system by 0.05 % and equilibrating it for 1 ps. During compression, the Nose-Hoover thermostat was used in the x-, y- and z-directions to maintain the temperature at 300 K and the Nose-Hoover barostat was applied to the x- and y-directions to maintain zero stresses and to allow relaxation of the system along those directions. The maximum applied compressive strains were varied between 6 % and 25 %, which is consistent with the range of strains used in the experiments. Recovery was simulated by removing the constraint on the z-dimension of the sample and by performing simulations at a constant temperature and pressure, where the pressure was set to 0 GPa.

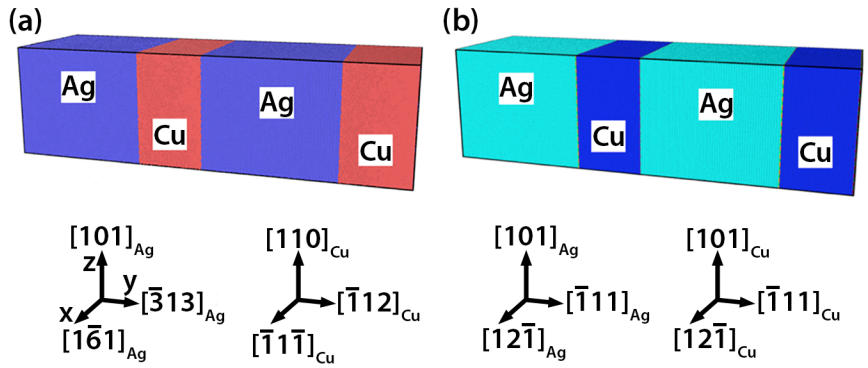

Figure 6.2.1 *Molecular dynamics simulation setup for (a) Ag/Cu incoherent twin interfaces and (b) Ag/Cu cube-on-cube interfaces.*

6.3 Results

6.3.1 Initial Structures

The microstructure of the directionally solidified material is predominantly lamellar (>66 %), although regions of globular platelets of Cu in a Ag matrix exist (<34 %) [7]. These structures are elongated in and are discontinuous along the growth direction. The layer thicknesses of the phases are approximately 170 nm and 330 nm for Cu and Ag, respectively. The lamellar morphology consists of an incoherent twin interface structure between Ag and Cu, as shown in Figs. 6.3.1(a)-(c). The interiors of both the Ag and Cu layers are mostly dislocation free. The interfaces, however, contain a higher density of dislocations, which are present as half loops terminating at the interfaces; examples are marked by arrowheads in the bright-field TEM micrograph presented in Fig. 6.3.1(a). From the selected area diffraction pattern, shown in Fig. 6.3.1(a), the orientation relationship between the phases is approximately 2° away from that of a coherent twin about the $[101]_{\mathrm{Ag}}||[110]_{\mathrm{Cu}}$ growth axis; this deviation is evident from comparison of the $(11\bar{1})_{\mathrm{Ag}}$ and $(11\bar{1})_{\mathrm{Cu}}$ diffraction spots, which are not collinear. The interface habit planes are incoherent twin and predominantly $(\bar{3}13)_{\mathrm{Ag}}||(\bar{1}12)_{\mathrm{Cu}}$ with variations toward the coherent twin plane of up to 10°, but more commonly up to 5°. The detailed structure of the incoherent twin interfaces is shown in the high-resolution TEM (HRTEM) micrograph presented in Fig. 6.3.1(b). The interfaces are stepped, with $(\bar{1}11)_{\mathrm{Ag}}$ and $(\bar{1}\bar{1}1)_{\mathrm{Ag}}$ planes on the Ag side and $(\bar{1}11)_{\mathrm{Cu}}$ and $(002)_{\mathrm{Cu}}$ planes on the Cu side. MD simulations of the Ag-Cu multilayers with incoherent twin interfaces, Fig. 6.3.1(c), show the same arrangement of atoms found in the HRTEM micrograph.

The second type of Ag/Cu interface that exists in this material has a cube-on-cube orientation relationship with interface habit planes of either $(\bar{1}11)_{\mathrm{Ag,Cu}}$ or $(11\bar{1})_{\mathrm{Ag,Cu}}$ With this interface, all of the crystallographic planes and directions between Ag and Cu are aligned. A region of this interface type is shown in the bright-field micrograph and selected area diffraction pattern presented in Fig. 6.3.1(d). Dislocations present in the initial material are primarily half loops in the Ag layer terminating at the interface. Examples of such dislocation loops are marked by arrowheads in Fig.

6.3.1(d). The HRTEM micrograph in Fig. 6.3.1(e) shows that the cube-on-cube interface is atomically flat with randomly spaced steps. Curved sections of the interfaces are a result of alternating segments of the $(\bar{1}11)_{Ag,Cu}$ and $(11\bar{1})_{Ag,Cu}$ planes. Misfit dislocations are observed at periodic intervals of 8-11 atomic planes of Cu and examples of these are marked by black circles in Fig. 6.3.1(e). In addition to the periodic dislocation structure, there is evidence of elastic strain at the interface, examples are marked by arrows in Fig. 6.3.1(e). The MD simulation for Ag-Cu multilayers with this orientation relationship, Fig. 6.3.1(f), shows nearly the same atomic-level structure as the interface observed experimentally. Specifically, the simulated structures contain an atomically flat $(\bar{1}11)_{Ag,Cu}$ interface with periodic misfit dislocations every nine Cu $(11\bar{1})_{Cu}$ atomic layers.

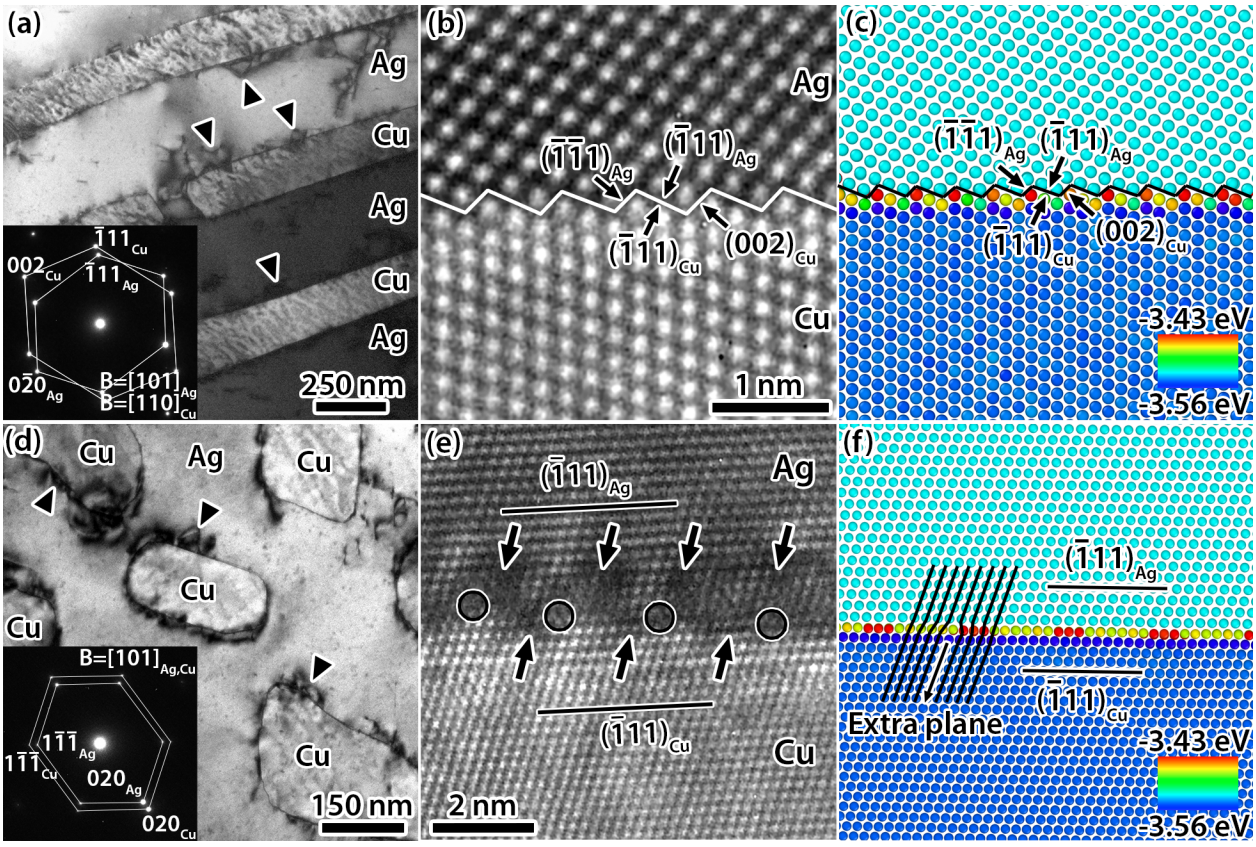

Figure 6.3.1 *(a) Bright-field TEM micrograph of incoherent twin Ag/Cu interfaces with selected area diffraction pattern shown in the inset. (b) HRTEM micrograph of an incoherent twin Ag/Cu interface. (c) MD simulation of incoherent twin Ag/Cu interface. (d) Bright-field TEM micrograph of cube-on-cube Ag/Cu interfaces with selected area diffraction pattern in the inset. (e) HRTEM micrograph of a cube-on-cube Ag/Cu interface. (f) MD simulation of a cube-on-cube Ag/Cu interface. Arrowheads in (a) and (d) mark dislocations in Ag at Ag/Cu interfaces. Arrows and circles in (e) mark periodic elastic strain and misfit dislocations, respectively. In (c) and (f), Ag atoms are colored with cyan, and Cu atoms are colored based on calculated potential energy.*

6.3.3 Mechanical Response of Incoherent Twin Interfaces

Stress-strain curves from MD simulations after compressing the material with incoherent twin interfaces along $[101]_{Ag}||[110]_{Cu}$ to strains of 10 % and 25 % are shown in Fig. 6.3.2(a). The curves have a distinct upper and lower yield point, which is followed by a region that shows a low work hardening rate. In this regard the simulations do not yield stress-strain curves consistent with those observed experimentally, compare Figure 6.3.2 with Figure 6.3.1 [12, 17]. Dislocation nucleation for both 10 % and 25 % strain simulations occurred at the maximum stress, which corresponded to an elastic strain of 3.8 %. After the systems were compressed uniaxially along the z-axis to the desired strain, the external constraint on the z-dimension was removed and the recovery process began. In the first stage of recovery, 1 ps after unloading, the strain decreased from an initial value of 10.00 % to 9.08 % as the average stress decreased to 0 GPa. This change in strain was due mainly to elastic recovery. Over the next 500 ps, the strain continued to decrease gradually to 8.25 %, which was due to plastic recovery that will be shown to be due to internal stresses. The change in strain with time during recovery is shown in the inset of Fig. 6.3.2(a). To estimate the error bar in the measured plastic strain recovery, we have performed eight simulations, all for the case of 10 % strain

but with different initiation conditions. The error bar corresponding to 97.5 % confidence interval calculated using student's t-distribution is 0.047 %, which is 1-2 orders of magnitude smaller than the average values of plastic strain recovery observed in our simulations. Higher strains were also simulated and it was found that as strain increased the amount of plastic recovery decreased. The degree of plastic recovery, both in the experiments and in the simulations, as a function of compressive strain is shown in Fig. 6.3.2(b), and is summarized in Tables 6.1.1 and 6.3.1, respectively. In comparison to the experiments, the magnitude of the measured plastic recovery is lower in the simulations. Potential reasons for this difference include: the time available for plastic recovery in the experiments was on the order of minutes whereas in the simulations it was on the order of nanoseconds and the density of the dislocations are likely different in the simulations and experiments. The latter potential difference could not be verified as in experiments the dislocation density prior to the plastic recovery is not accessible in a post-deformation analysis. However, both experiments and simulations show plastic strain recovery and that the magnitude of the recovery decreases with increasing strain. The DXA algorithm was used to quantify the dislocation density in the simulations after 10 % strain and then after 500 ps recovery. The results, presented in Fig. 6.3.2(c), show that during recovery the dislocation density decreased from $9.8\times10^{12}\text{cm}^{-2}$ to $7.3\times10^{12}\text{cm}^{-2}$ and from $3.8\times10^{12}\text{cm}^{-2}$ to $2.9\times10^{12}\text{cm}^{-2}$ in the Ag and Cu layers, respectively. Unfortunately, this change in the dislocation density cannot be confirmed experimentally.

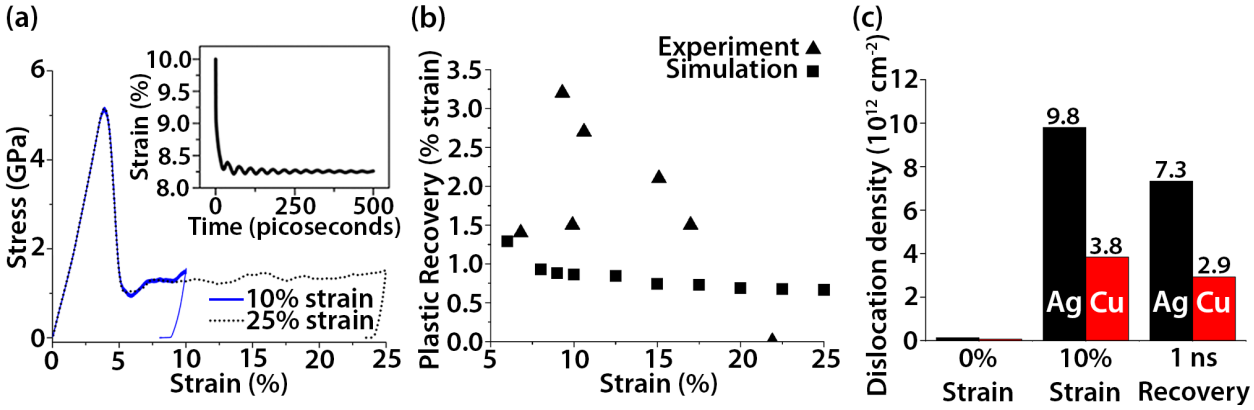

Figure 6.3.2 (a) Stress-strain relation during compression and recovery of the Ag-Cu system with *incoherent twin interfaces from MD simulations. Inset shows the change in strain with time during recovery when strained to 10 %. (b) Recovered plastic strain as a function of compressive strain present in the samples before recovery. (c) Dislocation density in Ag and Cu layers measured in MD simulations.*

Table 6.3. *Compressive strain levels and strain recovered for the simulations with incoherent twin interfaces.*

Sample	Angle between load and $[101]_{Ag}\|\|[110]_{Cu}$ growth direction	Strain rate (s^{-1})	Strain (%)	Strain recovered (%)Elastic	Strain recovered (%) Plastic
MD	0°	$5x10^8$	10.0	0.83	0.92
MD	90°	$5x10^8$	10.0	1.27	0.77

A comparison of the dislocation density in the Ag and Cu layers in samples strained dynamically that exhibited plastic strain recovery (sample 1, 3.2% plastic strain recovery) and ones that did not (sample 2, 4^{th} loading) are compared in Fig. 6.3.3. For completeness, the microstructure developed under quasi-static loading, which also showed no recovery, is included in Fig. 6.3.3. In comparing the dislocation structures it is evident that the dislocation density is always highest in the Ag layers, and that in samples that exhibited no plastic strain recovery the dislocations in the Ag were tangled (quasi-static, Fig. 6.3.3(c)) or organized into dislocation cells (sample 2, 4^{th} loading, Fig. 6.3.3(b)).

The primary difference in the Cu layer was that the dislocation density was lowest in the sample that exhibited plastic strain recovery. The locking of dislocations with each other provides a possible explanation for the decrease in plastic recovery with increasing strain.

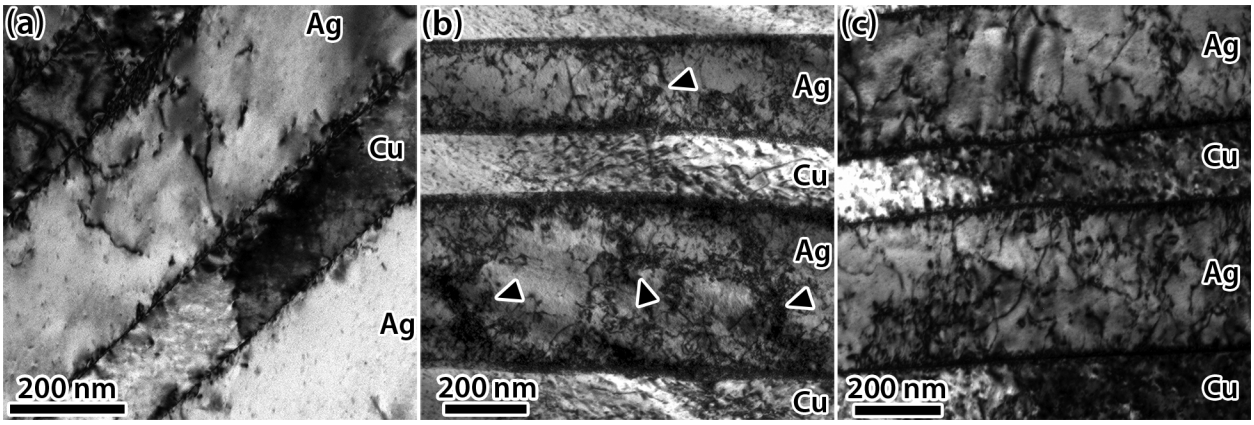

Figure 6.3.3 *Bright-field TEM micrographs of regions with incoherent twin interfaces (a) after loading to a true strain of 9.3 % dynamically; (b) after loading dynamically to a true strain of 21.9 %; (c) after loading to a true strain of 4 % by quasi-static compression. (d), (e), and (f) are selected area diffraction patterns of (a), (b), and (c), respectively. Arrowheads in (b) mark dislocation cell walls.*

The decrease in the dislocation density on recovery cannot be determined experimentally, however, a unique signature of this deformation response was that it caused a change in the interface character corresponding to an additional rotation away from the twin orientation relationship. The magnitude of this rotation and the loading conditions under which it occurred are summarized in Table 6.3.2. Representative zone-axis TEM micrographs and corresponding selected area diffraction patterns of samples loaded dynamically to strains of 9.3 % and 21.9 % and quasi-statically to a strain of 4 % are compared in Fig. 6.3.4. The rotation is measured by the angle between the $[11\bar{1}]_{\mathrm{Ag}}$ and $[11\bar{1}]_{\mathrm{Cu}}$ diffraction spots, and is visualized by the dotted lines in the selected area diffraction patterns

in Figs. 6.3.4(d)-(f). Rotation away from the twin orientation occurred for all loading conditions involving incoherent twin interfaces loaded along the $[101]_{Ag}||[110]_{Cu}$ growth direction. For loading dynamically along $[101]_{Ag}||[110]_{Cu}$, the rotation away from the twin orientation relationship increases with increasing strain, as shown in Table 6.3.2. Furthermore, even in the quasi-static loading case to a strain of 4.0 %, the interface rotated although no plastic recovery was observed. Interestingly, the degree of rotation observed for the quasi-static loading was similar in magnitude to the sample loaded dynamically to a strain of 9.3 %. However, it is worth noting that the latter sample exhibited recovery and the final strain was 5.7 %.

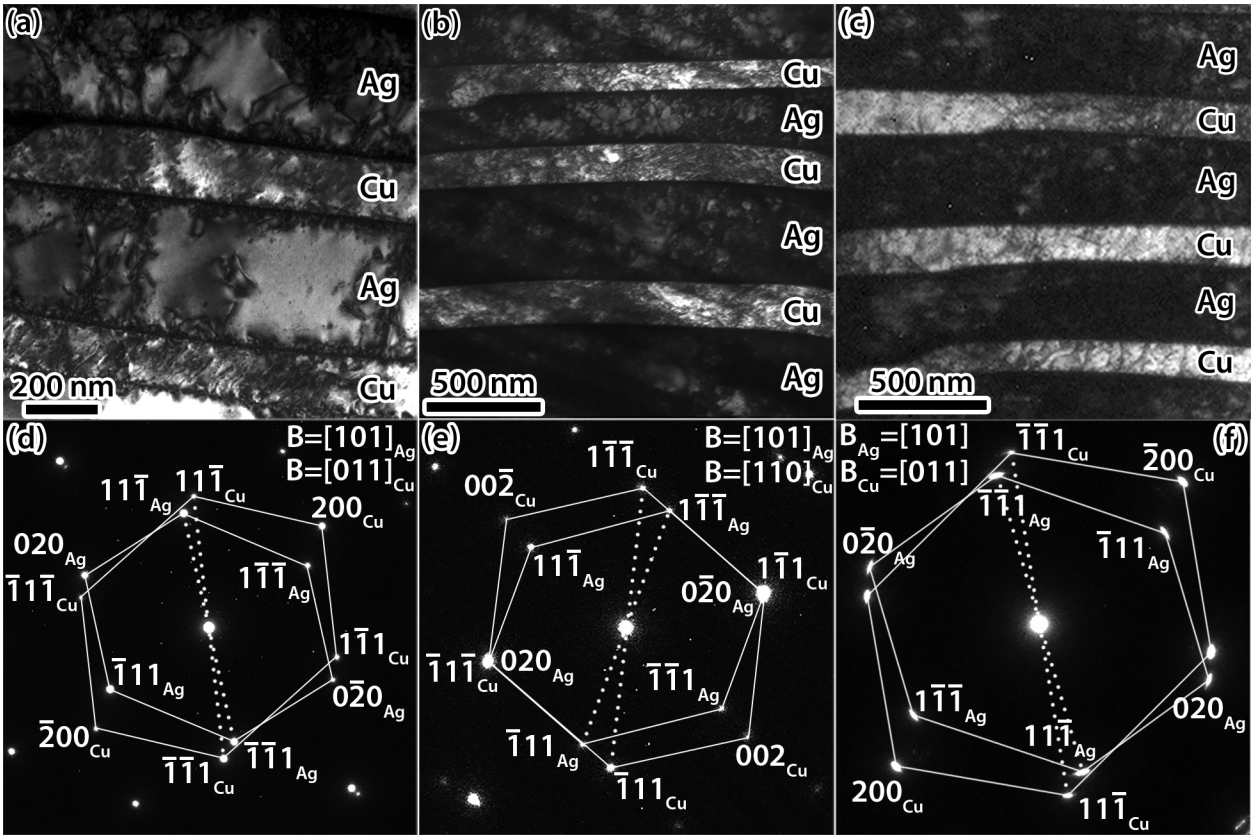

Figure 6.3.4 *Bright-field TEM micrographs of regions with incoherent twin interfaces after loading to dynamic strains of (a) 9.3 %, and (b) 21.9 % and quasi-statically to a strain of (c) 4 %.*

Analogous to the measurements taken experimentally, the angle between the $(\bar{1}11)$ plane in both Ag and Cu phases was measured from the Fast Fourier transforms of the undeformed, deformed, and deformed and recovered simulated layer structures. The simulated atomic structures are shown in Figs. 6.3.5(a)-(c) and the corresponding Fourier transforms can be found in Figs. 6.3.5(d)-(f). The rotation is measured as the angle between $[\bar{1}11]_{\mathrm{Ag}}$ and $[\bar{1}11]_{\mathrm{Cu}}$ and is indicated by the dotted lines in Figs. 6.3.5(d)-(f). The values of this angle for several of the simulations are summarized in Table 6.3.2. At peak loading the angle was found to be 6.6° at 10 % strain, and after 1 ns of recovery it decreased to 6.0°. This decrease did not occur after recovery following straining to 25 %, indicating that the mechanism which is responsible for the recovery and the decrease in the angle after loading to 10 % strain is not active at the higher strain.

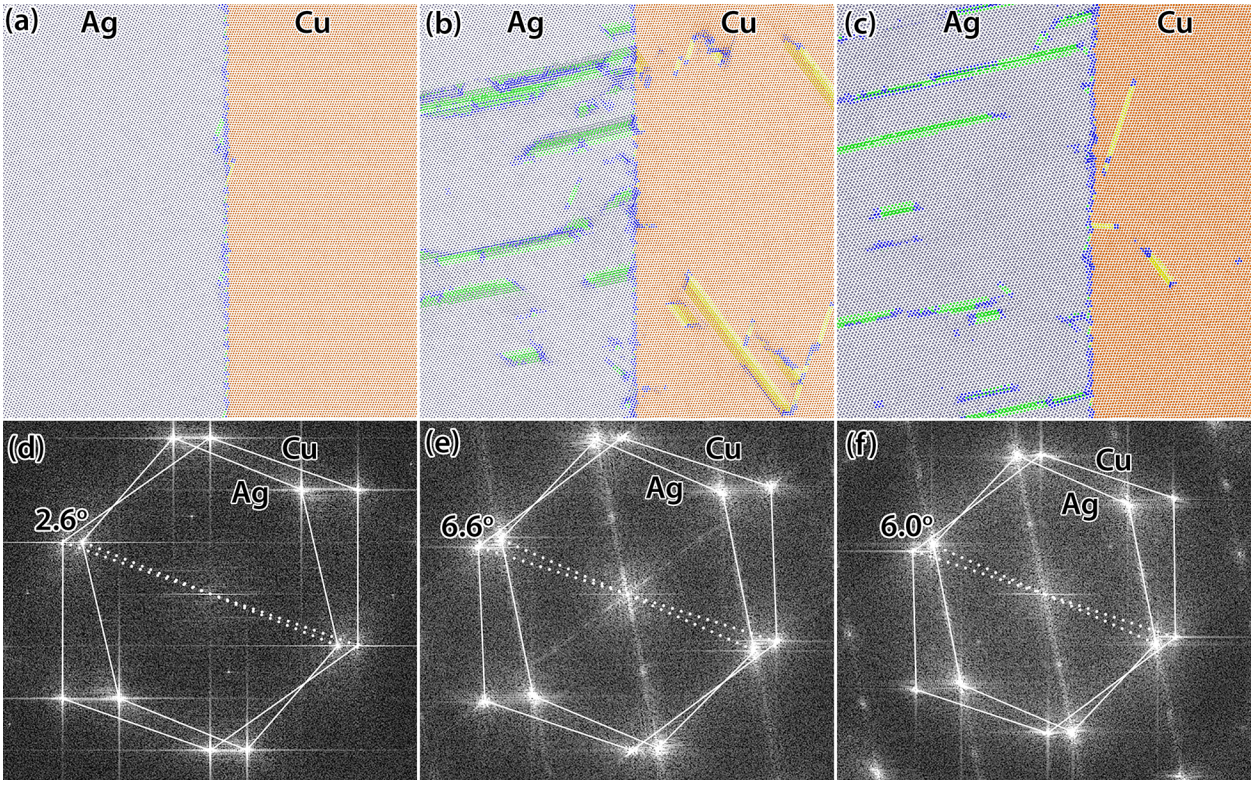

Figure 6.3.5 *Simulated atomic structures containing incoherent twin interfaces visualized in real space (a) before compression, (b) after compression at the peak strain of 10 % and (c) after*

recovery. (d), (e) and (f) are Fourier transforms of (a), (b), and (c), respectively. The direction normal to the image plane is $[101]_{Ag}$ *and* $[110]_{Cu.}$ *The difference between the* $(\bar{1}11)_{Ag}$ *and* $(\bar{1}11)_{Cu}$ *spots is visualized by the white dotted lines in (d), (e), and (f).*

Table 6.3.2 *Loading conditions and change in orientation relationship. SHPB and MD stand for split-Hopkinson pressure bar and molecular dynamics, respectively.*

Test method, strain (%), and load orientation with respect to the growth direction [13]	Range of rotation away from the twin orientation relationship (average value)	Test method, strain (%), and load orientation with respect to the growth direction	Range of rotation away from the twin orientation relationship (average value)
Undeformed material	0.7° to 2.4° (1.7°)	MD Undeformed	2.7° to 2.9° (2.8°)
SHPB, 9.3 %, 0°	5.9° and 9.8° (7.6°)	MD, 10 %, 0°	5.5° to 7.2° (6.2°)
		MD, 10 % and 500 ns recovery, 0°	4.2° to 6.0° (5.1°)
SHPB, 21.9 %, 0°	5.3° and 14.0° (10.3°)	MD, 25 %, 0°	10.1° to 10.7° (10.4°)
		MD, 25 % and 500 ns recovery, 0°	10.2° to 10.8° (10.4°)
SHPB, 15.4 %, 90°	0.0° to 5.2° (1.8°)	MD, 10 %, 90°	2.2° to 2.9° (2.4°)

		MD, 10 % and 500 ns recovery, 90°	2.0° to 2.7° (2.3°)
Quasi-static, 4 %, 0°	6.8° to 7.4° (7.0°)		

Experimentally, loading the incoherent twin interfaces 90° to the growth direction to 15.4 % strain did not result in a change in orientation relationship, that is, the angle between the $[\bar{1}11]_{\mathrm{Ag}}$ and $[\bar{1}11]_{\mathrm{Cu}}$ did not change. The deformed microstructures contained dislocations primarily in the Ag phase and these dislocations were organized into a dislocation cell structure. Deformation twinning was also observed to a limited extent at this load orientation and was confined to the Ag phase [7]. A representative bright-field micrograph of the deformation microstructure after loading 90° to the growth direction is shown in Fig. 6.3.6(a) and a corresponding selected area diffraction pattern in Fig. 6.3.6(b). An analogous MD simulation was performed, the system with incoherent twin interfaces, Fig. 6.2.1(a), was compressed along $[\bar{3}13]_{\mathrm{Ag}}$ and $[\bar{1}12]_{\mathrm{Cu}}$, which corresponds to loading 90° to the growth direction in the experiments. Numerical Fourier transformations conducted on atomic positions of the multilayers observed from the $[101]_{\mathrm{Ag}}$ and $[110]_{\mathrm{Cu}}$ direction show that the angle between $[\bar{1}\ 1\ 1]_{\mathrm{Ag}}$ and $[\bar{1}\ 1\ 1]_{\mathrm{Cu}}$ is approximately 2.6° before compression and does not change after straining to 10 % or after 1 ns of recovery.

Experiments and simulations of the cube-on-cube interface type reveal the orientation relationship between Ag and Cu remains cube-on-cube after deformation. The on-zone bright-field TEM image presented in Fig. 6.3.6(c) shows the deformation microstructure in a region with cube-on-cube interfaces after 9.5 % strain. Dislocations are found mainly in the Ag phase, with a higher density in regions of curvature of the Cu phase. The corresponding selected area diffraction pattern in Fig.

6.3.6(d) shows the orientation relationship between the two phases remains unchanged. Simulations also showed a retention of the orientation relationship between the two phases, because, unlike the incoherent twin interface case, the shape change of the layers due to dislocation slip was the same for both the Ag and Cu layers.

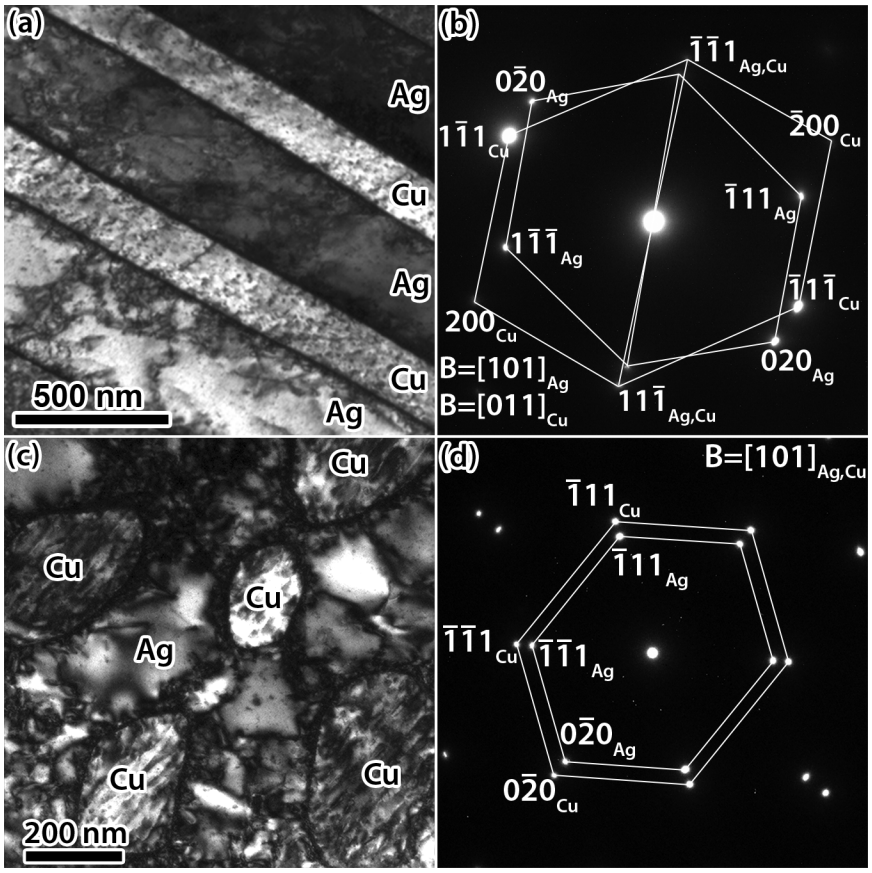

Figure 6.3.6 *(a) Bright-field TEM micrograph of incoherent twin interfaces after loading dynamically 90° to the growth direction to 15.4 % strain. (b) Selected area diffraction pattern of (a). (c) Bright-field TEM micrograph after loading dynamically along the* $[101]_{Ag,Cu}$ *growth direction to 9.3 % strain. (d) Selected area diffraction pattern of (c).*

Molecular dynamics simulations can provide details of dislocation activity during recovery in either the Ag or the Cu layer. The interactions were similar in nature in both layers and for ease of

describing different dislocation processes, we describe representative examples from the Cu layer. Figure 6.3.7 shows dislocation activity in layers with incoherent twin interfaces and illustrates the mechanisms of plastic recovery. During compression, dislocations were nucleated at the interfaces and these were observed to glide into interior regions of the layers. The observation of the interfaces serving as dislocation sources is consistent with the experimental observations of dislocation half-loops emerging from the interfaces. Different dislocation slip systems were activated and as these involved partial dislocations, the interaction of them resulted in the formation of stair-rod dislocations. As compression continued, dislocations were pinned either at the interfaces, or by other defects including other dislocations and stacking-fault tetrahedra. During recovery, the dislocation structure changed. Some dislocations interacted with other isolated dislocations or complex dislocation structures to become part of the immobile dislocation network. Other dislocations interacted with the interfaces and were incorporated into them. To illustrate two of the retraction mechanisms, activities of two representative interactions are presented in Fig. 6.3.7 and discussed in detail below. Again, for ease of discussion of the plastic recovery mechanism, the examples are selected from the Cu layer but similar interactions were observed to occur in the Ag layer.

The first example shows glissile partial dislocations generated from a dislocation tangle interacting with an incoherent twin interface and with other complex dislocation tangles in the Cu layer during loading and the reverse motion of these partial dislocations and their eventual incorporation back into the dislocation tangle from which they were generated on unloading. The Burgers vectors of the leading and trailing partial dislocations are $b_{\text{lead}} = \frac{a}{6}[11\bar{2}]$ and $b_{\text{trail}} = \frac{a}{6}[2\bar{1}\bar{1}]$, respectively. This pair of dislocations was generated from a stair-rod dislocation as part of the evolution of one of the complex dislocation tangles that exists in the Cu layer; the nucleation event is not captured in the images presented in Fig. 6.3.7, but the dislocation tangle from which they were generated is labeled E. The dislocation tangle results from the intersection of partial dislocations on different {111}

planes, which yields a stair rod dislocation at the intersection; another example of such a complex dislocation tangle is labeled D in Fig. 6.3.7. The glissile partial dislocations, along with the stacking fault (yellow atoms), following loading to a strain of 9.95 % are shown in Fig. 6.3.7(a) to be bowed out between pinning points at locations A and B. The pinning points are dislocation debris. The direction of motion of the leading partial dislocation is indicated by arrows in Fig. 6.3.7(a). The leading partial dislocation is blocked by the dislocation structure D. The intersection is with a partial dislocation with a Burgers vector of $\frac{a}{6}[\bar{1}\bar{2}1]$, which resides on $(\bar{1}11)_{\mathrm{Cu}}$, and intersects structure D beneath the viewing plane. This interaction resulted in the formation of a stair-rod dislocation, $\frac{a}{6}[\bar{1}\bar{2}1]+\frac{a}{6}[11\bar{2}]=\frac{a}{6}[0\bar{1}\bar{1}]$. As the strain was increased, the leading and trailing partial dislocations bowed out further between the pinning points and the leading partial dislocation intersected the interface and was blocked at location C, Fig. 9(b). On removing the external load, the leading partial dislocation was released from the interface pinning point and started to retract. After 9.5 ps from the time the external stress was removed, the two partial dislocations had retracted partially as shown in Fig. 9(c) but the reverse motion of the leading partial dislocation was hindered by the stair-rod dislocation generated from the intersection with defect structure D. After 15.5 ps, the leading partial dislocation was released from structure D and the stair-rod dislocation was eliminated. The leading and trailing partial dislocations remained pinned between pinning points A and B and started to bow out in the opposite direction, Fig. 6.3.7(d). With the release of the leading partial dislocation from structure D, it started to retract; this retraction can be seen by comparing Figs 6.3.7(c) and 6.3.7(d). On release of both partial dislocations from pinning point A, they move toward defect structure E, as shown in Fig. 6.3.7(e). At the recovery time of 27 ps, what was initially the trailing partial dislocation interacts with the dislocations within the complex structure E, which essentially results in assimilation of these partial dislocations into structure E, Fig. 6.3.7(f). This

series of images illustrates the role of the dislocation structure in the evolution of the microstructure during straining and during recovery.

The second example shows the interaction and annihilation of a layer of stacking fault through the interaction of a partial dislocation with the interface. The example shown in Figs. 6.3.7(g) through 6.3.7(i) is within the Cu layer. The leading partial dislocation, marked by the arrow in Fig. 6.3.7(g), lies on $(111)_{\mathrm{Cu}}$ plane and has a Burgers vector of $\frac{a}{6}[\bar{1}2\bar{1}]$ and is pinned at the interface at the locations marked by arrowheads. On removing the applied load, it retracts back to and spreads along the interface as seen in Figs. 6.3.7(h) and (i). Between Figs. 6.3.7(g) and 6.3.7(h), the dislocation retracts towards the interface and extends along it toward the dislocation structure F, which resides on $(11\bar{1})_{\mathrm{Cu}}$. At a recovery time of 50 ps, this partial dislocation had retracted to and spread along the interface in addition to part of the dislocation combining with structure F. The dislocation spreading along the interface and combining with dislocation content in the interface will cause rearrangement within the interface. There is also a reduction in the faulted area.

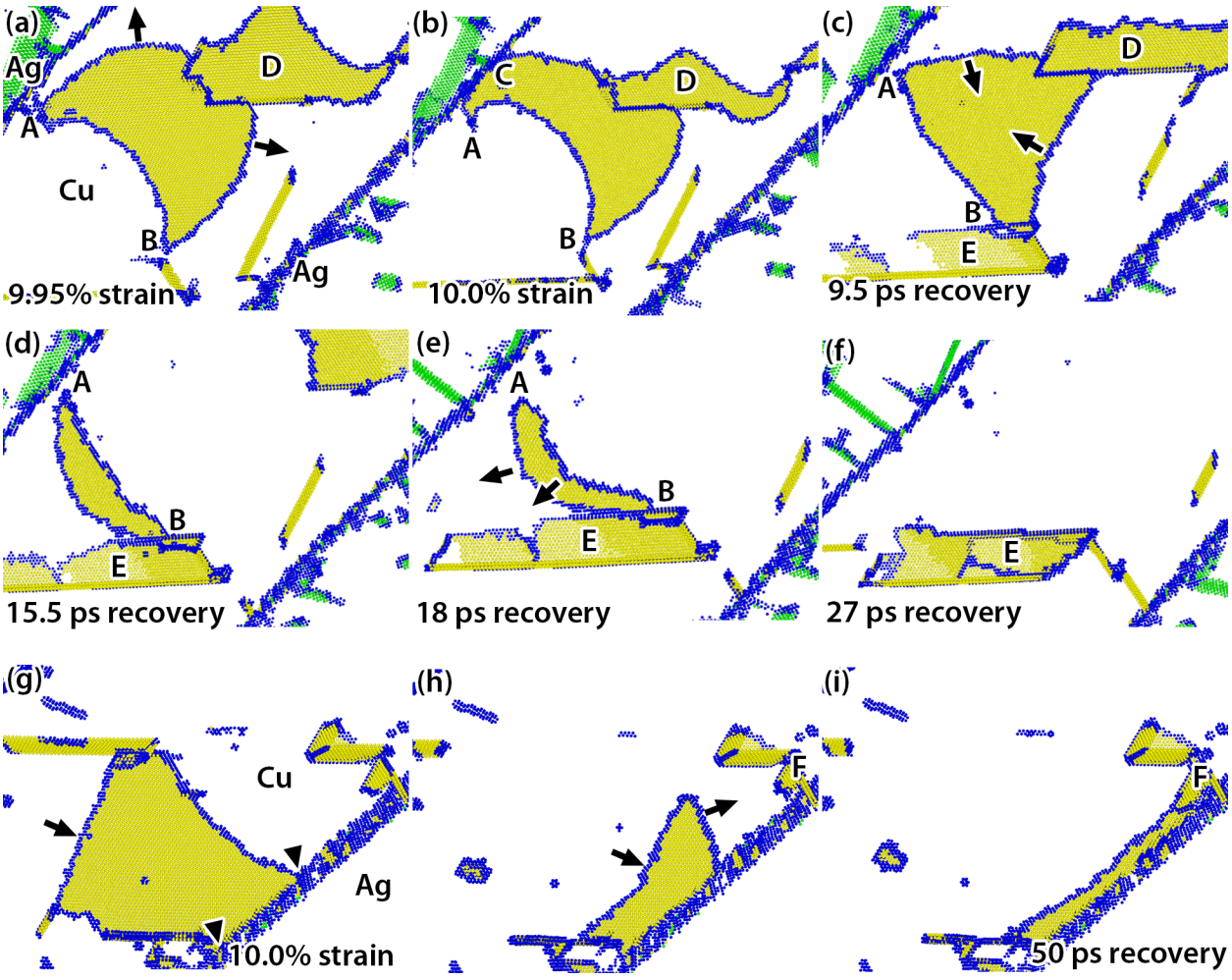

Figure 6.3.7 *Dislocation mechanisms underlying plastic recovery in samples with incoherent twin interfaces. (a)-(f) Dynamics of partial dislocation mobility and pinning at the interface and dislocation tangles during loading (a)-(b) and unloading (c)-(f). A and B are two stable defect sites. D and E are complex dislocation structures. (g)-(i) Annihilation of a stacking fault and dislocation line length on retraction into the interface nucleation site. Arrows indicate the direction of dislocation motion. Arrowheads in (g) mark dislocation pinning points at the interface. In (a)-(i), blue atoms do not have local fcc, bcc, or hcp order and represent grain boundary atoms, dislocation cores, and other defect structures inside the layers. Yellow atoms have hcp structure and represent*

stacking faults; fcc atoms are not visualized. Recovery time mentioned in (c)-(f) and (h)-(i) was measured from the time when the applied compressive stress was removed.

The change in interfacial structure and build-up of dislocations at the interfaces can be further interpreted from the perspective of the potential energy. Plotting local potential energy as a function of the distance from the interface provides a practical way to access information about the effect of the loading history on the evolution of interfacial energy. This is because interfacial energy is equal to the difference in potential energies of the interface and a corresponding single crystal, normalized by the interfacial area. The local potential energy is plotted in Figs. 6.3.8(a)-(c) for the cases of (a) incoherent twin interfaces with the load applied along the $[101]_{\mathrm{Ag}}$ and $[110]_{\mathrm{Cu}}$ directions, (b) incoherent twin interfaces with load direction 90° away from the experimental growth direction, specifically along $[\bar{3}13]_{\mathrm{Ag}}$ and $[\bar{1}12]_{\mathrm{Cu}}$, and (c) cube-on-cube interfaces with loading along the $[101]_{\mathrm{Ag,Cu}}$. The reported potential energy is averaged over 4 Å-thick slices parallel to the Ag/Cu interfaces (x-y plane). For the multilayer simulation with incoherent twin interfaces before compression (0 % strain), the energy at the interface region is slightly higher (by 0.0024 eV) than the energy in the Ag layer. After the samples are compressed to a strain of 10 % with the loading direction along the $[101]_{\mathrm{Ag}}$ and $[110]_{\mathrm{Cu}}$ direction, the interfacial energy increased from -2.8096 eV to -2.7968 eV and the energy of the inner Ag layers increased from -2.8120 eV to -2.8082 eV. After recovery, the interfacial energy decreased to -2.8000 eV and the energy of the interior of the Ag layers decreased to -2.8091 eV. The decrease in energy at the interfaces (by 0.11 %) is more significant than that inside the layers (by 0.03 %), Fig. 6.3.8(a).

After loading the same multilayer system with incoherent twin interfaces to a compressive strain of 10 %, but this time with the loading direction 90° away from $[101]_{\mathrm{Ag}}$ and $[110]_{\mathrm{Cu}}$, specifically,

along $[\bar{3}13]_{\mathrm{Ag}}$ and $[\bar{1}12]_{\mathrm{Cu}}$, the interfacial energy increased from -2.8096 eV to -2.7976 eV and the energy of interior of the Ag layers increased from -2.8120 eV to -2.8096 eV, Fig. 6.3.8(b). After recovery, the interfacial energy and the energy of the interior of Ag layers decreased to -2.7986 eV and -2.8104 eV, respectively. A decrease in energy at the interfaces (0.04 % decrease) is also greater than the decrease of energy inside layers (0.03 % decrease), though the difference is not as significant as in the case when the samples were loaded along $[101]_{\mathrm{Ag}}$ and $[110]_{\mathrm{Cu}}$.

A similar analysis for the multilayered structure with cube-on-cube interfaces loaded along $[101]_{\mathrm{Ag,Cu}}$ was performed. Here, before compression (0 % strain), the average energy in the interface region and the average energy inside the Ag layers were the same and equal to -2.8122 eV. The energy is distributed more evenly among the interfaces and the layer interiors than in the case of incoherent twin interfaces. After the samples with the cube-on-cube interfaces were compressed to a strain of 10 %, the interfacial energy increased to -2.7986 eV and the energy of the interior of the Ag layers increased to -2.8021 eV. After recovery, the interfacial energy and the energy of the interior of the Ag layers decreased to -2.8035 eV and -2.8051 eV, respectively (see Fig. 6.3.8(c)). Again, the energy decrease at the interfaces (by 0.18 %) is greater than in the layer interiors (0.11 %), but the difference between the layer interior and the interface is not as significant as that observed in the multilayers with incoherent twin interfaces loaded along the $[101]_{\mathrm{Ag}}$ and $[110]_{\mathrm{Cu}}$ direction.

Figure 6.3.8(d) shows the ratio of energy change at the interfaces to the energy change in the Ag layer interiors after 500 ps recovery. The ratios are shown for the multilayers with incoherent twin interfaces loaded along the $[101]_{\mathrm{Ag}}$ and $[110]_{\mathrm{Cu}}$ direction, and loaded along $[\bar{3}13]_{\mathrm{Ag}}$ and $[\bar{1}12]_{\mathrm{Cu}}$, as well as for the multilayers with cube-on-cube interfaces loaded along $[101]_{\mathrm{Ag,Cu}}$. In all three cases the ratio is larger than 1, which means that the energy change in the interfacial region is more significant than that in the Ag layer interiors. There are two reasons for this ratio being larger than 1.

The first is that during deformation, dislocation content builds up at the interfaces to a larger extent than the layer interiors. As a result, during recovery the dislocation density near the interfaces decreases more significantly than the dislocation density in the Ag layer interiors. The second is that dislocations blocked by the interfaces can be repelled from the interfaces by the local stress after the external load is removed.

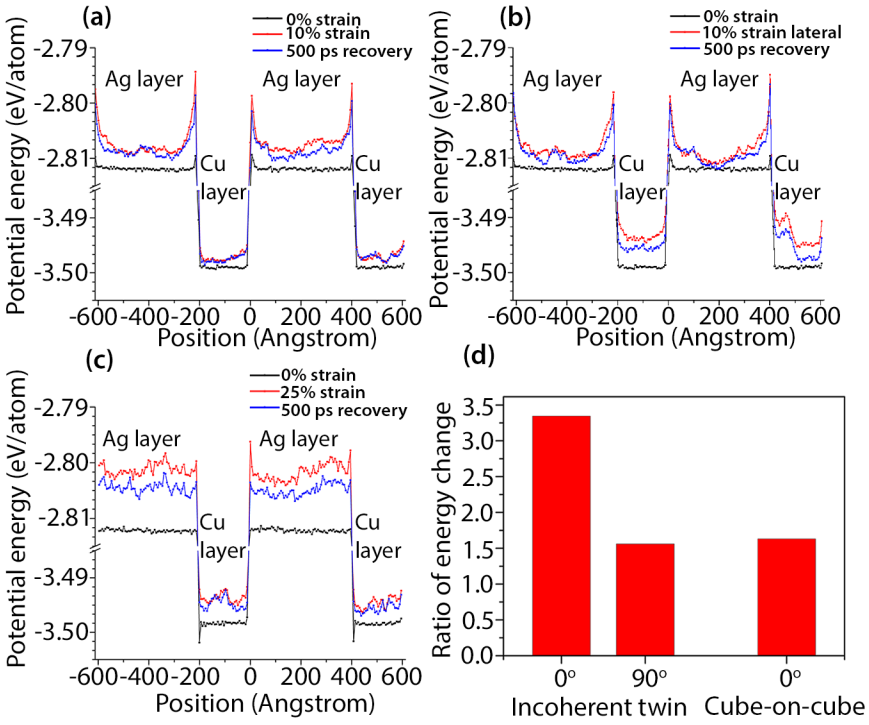

Figure 6.3.8 *(a) Potential energy calculated along the direction normal to the incoherent twin interfaces in the case of loading along* $[101]_{Ag}$ *and* $[110]_{Cu}$ *for 0 % strain (before loading), 10 % strain (at the peak of loading) and at 500 ps of the recovery stage. (b) Potential energy along the direction normal to the interface for the system with incoherent twin interfaces loaded at 90° to* $[101]_{Ag}$ *and* $[110]_{Cu}$*. (c) Potential energy along the direction normal to the interface in the system with cube-on-cube interfaces loaded along* $[101]_{Ag,Cu}$*. (d) Ratio of energy change between the interface and the Ag layer interior.*

6.4 Discussion

Comparison of the experimental and simulation results provides insights into the plastic strain recovery mechanisms, which are based on reversing the direction of dislocation motion, dislocation annihilation, and rearrangements at and within the interfaces. These mechanisms are dependent on the activated slip systems resulting in a change in interface structure and increasing the energy of the interfaces, providing the driving force for the plastic recovery. Specifically, the change of the interface structure, orientation relationship as described by the rotation of the interface, is proposed to be the driving force behind the plastic recovery. The degree of this recovery was dependent on the loading direction and the interface type; this was evident in the experiments but not the simulations. The degree of plastic strain recovery was greatest for loading along the $[101]_{\mathrm{Ag}}$ and $[110]_{\mathrm{Cu}}$ growth direction when the interfaces were incoherent twins. Specific to loading in this direction, the simulations showed that preferential deformation in the $[0\bar{1}0]_{\mathrm{Ag}}$ and $[00\bar{1}]_{\mathrm{Cu}}$ direction occurs and this causes the change in the orientation relationship between Ag and Cu. When the original orientation relationship between the Ag and Cu layers is cube-on-cube, and both phases are loaded along the $[101]_{\mathrm{Ag,Cu}}$ direction, the layers still deform anisotropically but in the same direction for Ag and Cu, and as a consequence retain their original orientation relationship. Similarly, loading of coherent twin interfaces 90° to the growth direction, along $[\bar{3}13]_{\mathrm{Ag}}$ and $[\bar{1}12]_{\mathrm{Cu}}$, did not change the orientation relationship between the layers. For this case the magnitude of the plastic recovery was similar in the simulations and experiments and was less than loading along the $[101]_{\mathrm{Ag}}$ and $[110]_{\mathrm{Cu}}$ growth direction.

The dependence of the magnitude of the recovery on the interface type and loading direction can be made based on the ratio of energy change between the interface and layer interiors, see Fig. 6.3.8(d). This ratio is larger for the case which shows the largest plastic strain recovery at low levels

of strain. That is, it is larger for loading of incoherent twin interfaces along $[101]_{Ag}$ and $[110]_{Cu}$, Fig. 6.3.8(a). The difference in this ratio is related to the slip systems that become active during compression in each loading geometry. For example, loading along the $[101]_{Ag}$ and $[110]_{Cu}$ directions for the incoherent twin interfaces activates dislocations that are blocked by the interfaces and also causes a change in orientation relationship between the Ag and Cu layers. In contrast, loading 90° from the $[101]_{Ag}$ and $[110]_{Cu}$ directions, when the interfaces are incoherent twins, activates some dislocations that can transfer across the interfaces and, additionally, the orientation relationship between the Ag and Cu layers is not changed by the deformation. Similarly, for cube-on-cube type interfaces loaded along the $[101]_{Ag,Cu}$ axis, the original orientation relationship is retained and some specific dislocations can transfer readily across the interfaces. The retention of the initial orientation relationship in the latter two cases results in a smaller local residual stress at the interface. This means incoherent twin interfaces with the applied load along $[101]_{Ag}$ and $[110]_{Cu}$ are more effective in decreasing dislocation density in the interface region after unloading, leading to plastic strain recovery, and resulting in a larger ratio of energy change between peak loading and recovery. While similar to the back motion of dislocations for plastic strain recovery cited in the penta-twinned Ag nano-wires [15], the AgCu eutectic, however, appears to require a change in the interface structure to drive the plastic strain recovery.

To explore the decrease in magnitude of the plastic strain recovery with increasing strain and the lack of any significant plastic strain recovery for quasi-statically deformed specimens with primarily incoherent twin interfaces compressed along $[101]_{Ag}$ and $[110]_{Cu}$, it is necessary to consider the evolved microstructure within the layers. In both cases, the evolved deformation microstructures consist of dislocation cell structures and dislocation tangles, Fig. 6.3.3. The lack of plastic recovery

can be attributed to the dislocation-dislocation interactions locking the dislocations in position, which inhibits dislocation motion and, hence, the plastic strain recovery.

6.5 Conclusion

The mechanism for plastic strain recovery in AgCu eutectic was determined to be dislocation retraction and annihilation, which is driven by stresses at the interfaces. This was most prominent for the case in which plastic deformation in the Ag and Cu layers was incompatible, such that the orientation relationship between Ag and Cu changes during loading. Dislocations on the activated glide systems were also found to be blocked, and residual stresses built-up at the interfaces promoting dislocation back motion during unloading. In the cases in which the deformation in the Ag and Cu layers were compatible and there is no change in the orientation relationship, plastic strain recovery was inhibited. In addition, only some of the activated dislocations were blocked by the interfaces. As a result, the driving force for dislocation back motion exerted by these interfaces was smaller than in the case with plastic strain recovery. Decreasing plastic strain recovery with increasing strain as well as lack of plastic strain recovery in quasi-statically loaded specimens is attributed to the locking of dislocations in dislocation tangles and cell structures in the layer interiors.

References

[1] A. Balyanov, J. Kutnyakova, N.A. Amirkhanova, V.V. Stolyarov, R.Z. Valiev, X.Z. Liao, Y.H. Zhao, Y.B. Jiang, H.F. Xu, T.C. Lowe, Y.T. Zhu. Corrosion resistance of ultra fine-grained Ti, Scripta Materialia 51 (2004) 225-229.

[2] P.Q. La, J.Q. Ma, Y.T. Zhu, J. Yang, W.M. Lu, Q.J. Xue, R.Z. Valiev. Dry-sliding tribological properties of ultrafine-grained Ti prepared by severe plastic deformation, Acta Materialia 53 (2005) 5167-5173.

[3] J.T. Wood, J.D. Embury, M.F. Ashby. An approach to materials processing and selection for high-field magnet design, Acta Materialia 45 (1997) 1099-1104.

[4] T. Hochbauer, A. Misra, K. Hattar, R.G. Hoagland. Influence of interfaces on the storage of ion-implanted He in multilayered metallic composites, Journal of Applied Physics 98 (2005) 1-7.

[5] K. Hattar, M.J. Demkowicz, A. Misra, I.M. Robertson, R.G. Hoagland. Arrest of He bubble growth in Cu-Nb multilayer nanocomposites, Scripta Materialia 58 (2008) 541-544.

[6] M.A. Meyers, A. Mishra, D.J. Benson. Mechanical properties of nanocrystalline materials, Prog. Mater. Sci. 51 (2006) 427-556.

[7] B.P. Eftink. Dislocation interactions with characteristic interfaces in Ag-Cu eutectic. Materials Science and Engineering, vol. Ph.D.: University of Illinois Urbana-Champaign, 2016.

[8] S.J. Zheng, J. Wang, J.S. Carpenter, W.M. Mook, P.O. Dickerson, N.A. Mara, I.J. Beyerlein. Plastic instability mechanisms in bimetallic nanolayered composites, Acta Materialia 79 (2014) 282-291.

[9] Y.Z. Tian, Z.F. Zhang. Bulk eutectic Cu-Ag alloys with abundant twin boundaries, Scripta Materialia 66 (2012) 65-68.

[10] O.T. Kingstedt, B. Eftink, J. Lambros, I.M. Robertson. Quasi-static and dynamic compressive deformation of a bulk nanolayered Ag–Cu eutectic alloy: Macroscopic response and dominant deformation mechanisms, Materials Science and Engineering: A 595 (2014) 54-63.

[11] J. Kacher, B.P. Eftink, B. Cui, I.M. Robertson. Dislocation interactions with grain boundaries, Curr. Opin. Solid State Mat. Sci. 18 (2014) 227-243.

[12] O.T. Kingstedt, B.P. Eftink, I.M. Robertson, J. Lambros. Inelastic strain recovery of a dynamically deformed unidirectional Ag-Cu eutectic alloy, Acta Materialia (accepted) (2016).

[13] J. Rajagopalan, J.H. Han, M.T.A. Saif. Plastic deformation recovery in freestanding nanocrystalline aluminum and gold thin films, Science 315 (2007) 1831-1834.

[14] X.Y. Li, Y.J. Wei, W. Yang, H.J. Gao. Competing grain-boundary- and dislocation-mediated mechanisms in plastic strain recovery in nanocrystalline aluminum, Proc. Natl. Acad. Sci. U. S. A. 106 (2009) 16108-16113.

[15] Q.Q. Qin, S. Yin, G.M. Cheng, X.Y. Li, T.H. Chang, G. Richter, Y. Zhu, H.J. Gao. Recoverable plasticity in penta-twinned metallic nanowires governed by dislocation nucleation and retraction, Nat. Commun. 6 (2015) 1-8.

[16] R.Z. Li, H.B. Chew. Deformation twinning and plastic recovery in Cu/Ag nanolayers under uniaxial tensile straining, Philos. Mag. Lett. 94 (2014) 260-268.

[17] O.T. Kingstedt, B.P. Eftink, I.M. Robertson, J. Lambros. Anisotropic dynamic compression response of a directionally-cast silver–copper eutectic alloy, Acta Materialia 105 (2016) 273-283.

[18] S. Plimpton. Fast parallel algorithms for short-range molecular dynamics, J. Comput. Phys. 117 (1995) 1-19.

[19] P.L. Williams, Y. Mishin, J.C. Hamilton. An embedded-atom potential for the Cu-Ag system, Model. Simul. Mater. Sci. Eng. 14 (2006) 817-833.

[20] A. Stukowski, K. Albe. Dislocation detection algorithm for atomistic simulations, Model. Simul. Mater. Sci. Eng. 18 (2010) 1-15.

[21] A. Stukowski. Visualization and analysis of atomistic simulation data with OVITO-the Open Visualization Tool, Model. Simul. Mater. Sci. Eng. 18 (2010) 1-7.

Chapter 7 Interaction Mechanisms between Dislocations and Ag/Cu Interfaces

Contributions

This Chapter discusses results of combined MD simulations and experiments. Experiments were conducted by Dr. B.P. Eftink from University of Illinois Urbana-Champaign and Prof. I.M. Robertson from University of Wisconsin - Madison. Dr. Eftink and Prof. Robertson have also written text in this chapter that describes experimental results. I provided comments and edits on the experimental sections. I wrote sections describing results of MD simulations and Prof. Szlufarska helped edit these sections. Methods and discussion sections were written together with the experimental collaborators.

7.1 Introduction

Deformation twinning in Cu has been reported to occur in AgCu alloys in regions with a cube-on-cube orientation relationship with $\{111\}_{\mathrm{Ag}}||\{111\}_{\mathrm{Cu}}$ interfaces after greater than 52.9% rolling reductions, and high strain-rate compression, 10^3 s^{-1}, for strains as low as 4% [1-3]. This response has been attributed to direct transmission of twinning partial dislocations from Ag through the interface into Cu [1, 2]. This particular mechanism does not derive from interface-mediated nucleation processes, and depends instead on a prolific supply of twinning partial dislocations from the Ag-phase transmitting into the Cu-phase. As such, in the AgCu system deformation twinning occurs in Cu under conditions it would otherwise not activate. Twinning partial dislocation communication across cube-on-cube interfaces from Ag to Cu, however, has barriers arising from the presence of misfit dislocations and coherency strains from the lattice mismatch between phases,

image forces due to differences in elastic modulus; and the necessity to leave a residual dislocation at the interface with a Burgers vector of $|\mathrm{b_{res}}| = \left|\frac{a}{6}\langle 112\rangle_{\mathrm{Ag}} - \frac{a}{6}\langle 112\rangle_{\mathrm{Cu}}\right| = 0.2$ Å for each twinning partial dislocation involved in the strain transfer, where a_{Ag} and a_{Cu} are the lattice parameters of Ag and Cu, respectively [4-6]. Rotation of the interface by the passage of different types of partial dislocations occurs as predicted by dislocation theory, however, has not been clearly observed experimentally. For the AgCu system, twinning in Cu has only been confirmed for cube-on-cube type interfaces, testing other characteristic interfaces will help elucidate the mechanism driving twinning in Cu for a variety of interface types. Rotations of the cube-on-cube interfaces consistent with dislocation theory will be shown, confirming the mechanism of direct communication of twinning partial dislocations across that interface type. Lack of deformation twinning in Cu when the Ag/Cu interfaces are incoherent twin type will be related back to strain transfer mechanisms developed for dislocations encountering grain boundaries.

7.2 Methods

Material for this study was produced by either water quenching or directional solidification of AgCu eutectic as has been described previously [7, 8]. Bulk samples were strained by Split-Hopkinson pressure bar compression at 10^3 s^{-1} with the experimental details and mechanical response reported in Kingstedt et al. [9]. *In situ* TEM straining was also performed on the as-cast material and samples were prepared by focused ion beam (FIB) machining as described by Field et al. [10]. This method allowed specific locations of the material to be strained at chosen orientations with respect to the interfaces. FIB was conducted on a FEI Helios 600i and the samples were thinned to electron transparency with a final milling voltage of 2.0 keV. The samples were then strained in a Gatan strain stage while observing with either a Tecnai TF-30 or JEOL 2010 LaB_6 microscope operating at 300 keV and 200 keV respectively.

MD simulations were conducted to investigate dislocation-interface interactions in Ag/Cu alloys with incoherent twin and cube-on-cube interfaces using the LAMMPS software [11]. Embedded atom force-field was used to describe Ag-Ag, Ag-Cu, and Cu-Cu interactions [12]. All visualizations were performed using OVITO [13]. The system configuration, mimics the multilayer Ag/Cu alloy used in the experiments. For both multilayers with incoherent twin and cube-on-cube interfaces, periodic boundary conditions were applied only in the y- direction, but not in the x- and z-directions.. The Ag layer and the two Cu layers were therefore infinite in the y- direction, but finite in the x- and z- directions with four free surfaces. In z- direction, surface atoms, which are within 0.5nm in distance from top surface and bottom surface, are termed as top edge and bottom edge layers. The dimensions of Ag and Cu layers were 30nm in z- direction and 2nm in y- direction. For the multilayer with incoherent twin interfaces, in the x-direction, the Ag layer was 220nm thick and the average thickness of Cu layers was 72nm. For the multilayer with cube-on-cube interfaces, in the x-direction, the Ag layer was 86nm thick and the average thickness of Cu layers was 37nm.The interfaces between the Ag and Cu layers for the incoherent twin interfaces were characterized by $(\bar{3}13)_{\mathrm{Ag}}||(\bar{1}12)_{\mathrm{Cu}}$ habit planes. The incoherent twin interfaces had a stepped structure, with $(1\bar{1}\bar{1})_{\mathrm{Ag}}$ and $(\bar{1}\bar{1}1)_{\mathrm{Ag}}$ planes on the Ag side and $(1\bar{1}\bar{1})_{\mathrm{Cu}}$ and $(002)_{\mathrm{Cu}}$ planes on the Cu side which is consistent with previous work [14]. The interfaces between the Ag and Cu layers for the cube-on-cube interfaces were characterized by $(\bar{1}11)_{\mathrm{Ag}}||(\bar{1}11)_{\mathrm{Cu}}$ habit planes.

In order to generate the nanolayered structures with incoherent twin and cube-on-cube interfaces, single crystal Ag and Cu systems were first created. These single crystals were then equilibrated for 1ns at 5K and 0GPa using Berendsen thermostat and barostat. Equilibrated Ag and Cu layers were then joined alternatively to form nanolayers stacked along the x- direction. The energy of the as-stacked Ag/Cu interfaces was minimized using the conjugate gradient algorithm and then relaxed at 300K and 0GPa for another 1ns.

Two preexisting dislocations in the Ag layer were introduced to study the specific dislocation/interface interaction mechanisms. The dislocations were first created by removing an atom plane with plane normal $[12\bar{1}]_{\mathrm{Ag}}$. This atom plane was in the center of the Ag layer and 4nm high in z- direction. After minimizing the energy of this defected region through conjugate gradient algorithm and relaxing the region at 300K and 0GPa for 1ns, two dissociated perfect dislocations were created in the center of the Ag layer with opposite Burgers vectors. The dislocation lines were along y- directions and the glide planes of these dislocations were $[1\bar{1}\bar{1}]_{\mathrm{Ag}}$.

Constant shear strain rate was applied to drive the preexisting dislocations to interact with the incoherent twin and cube-on-cube interfaces. During the shearing deformation, the top edge and the bottom edge which have been defined previously were frozen and moved in x and -x directions, respectively. The velocity of the top edge was 10m/s and the velocity of the bottom edge frozen layer was -10m/s, providing a shear strain rate of $6.67\times10^{8}\mathrm{s}^{-1}$. Nose-Hoover thermostat was used in the y- and z-directions to maintain the temperature at 300 K.

7.3 Results

AgCu eutectic produced by casting can exhibit cube-on-cube and incoherent twin interfaces. Both interface types were investigated to determine the conditions under which deformation twins in Ag, on interacting with the interface, induce deformation twinning in Cu, as well as how dislocations in general interact with the interfaces. These observations are related to the geometric arrangement of slip systems of the Ag and Cu.

7.3.1 Cube-on-cube Interfaces

Ag/Cu interfaces with a cube-on-cube orientation relationship have the same crystallographic planes and directions aligned between Ag and Cu. In this case it was observed that deformation twins are continuous across the interface. Both *in situ* and *ex situ* deformation experiments were

conducted and both deformation methods exhibited the same behavior. Figure 7.3.1 contains two time-resolved images of a continuous deformation twin crossing two Ag/Cu interfaces in 1100 nm thick bi-layer material with the cube-on-cube orientation relationship between Ag and Cu. A deformation twin is seen, marked with arrows, to propagate through both the Ag and Cu-phases in Fig. 7.3.1(a). That is, the deformation twin has transferred across a Ag/Cu interface and across a Cu/Ag interface. With increasing strain, the deformation twin thickens to approximately 38 nm in both phases, Fig. 7.3.1(b). A twin of that thickness would require 161 twinning partial dislocations in Ag, each on consecutive planes. The same number of twinning partial dislocations in Cu would result in a twin with a thickness of 34 nm, the difference in thickness could not be determined from the image. For the twin to transfer from Cu back into Ag, the thickness would return to 38 nm. Ultimately, the transfer of the twinning partial dislocations across the interface results in a rotation of the interface. From the selected area diffraction pattern the crystallographic planes of the twin and interfaces are determined, Fig. 7.3.1(c). Initially the interface is $(1\bar{1}\bar{1})_{\mathrm{M}}$ and after twin transmission it is $(\bar{1}1\bar{1})_{\mathrm{T}}$ indicating the twinning partial dislocations have a Burgers vector of $\frac{a}{6}[\bar{1}21]_{\mathrm{M}}$ and are glissile on the $(\bar{1}\bar{1}1)_{\mathrm{M}}$ plane; here M and T refer to the matrix and twin, respectively. The different planes are indicated in Fig. 7.3.1. The rotation of the interface was 39° which is consistent with rotations observed in several SHPB deformed samples, presented in a different publication as well as MD simulations [6, 8]. The idea that twinning in the Cu-phase can be induced by the transfer of Ag twinning partial dislocations across the interface is supported by MD simulations exhibiting the same geometric changes.

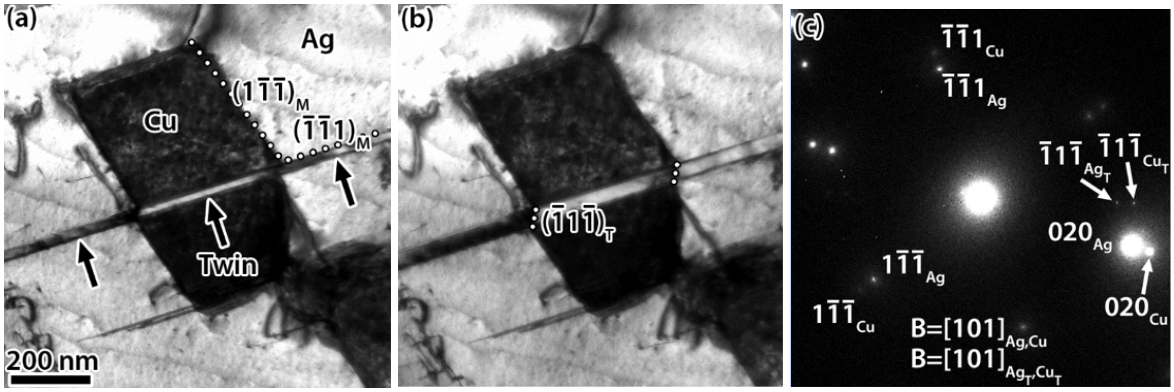

Figure 7.3.1 *(a) and (b) Time resolved images showing the thickening of a deformation twin in both Ag and Cu that is continuous across two cube-on-cube interfaces with increasing strain. Arrows mark a deformation twin. White dotted lines mark interface planes, twin as well as Ag/Cu. Images from material with 1100 nm bi-layer thickness. (c) Selected area diffraction pattern of (b).*

Figure 7.3.2 shows still frames from a MD simulation of a layered AgCu structure with cube-on-cube interfaces between the Ag and the Cu. Thickening of a deformation twin is observed by the slip of leading partial dislocations, twinning partials, with Burgers vectors of $\frac{a}{6}[\bar{1}21]$ on sequential $(\bar{1}\bar{1}1)$ planes. Transmission of the twinning partial dislocations was observed from both Ag to Cu as well as Cu to Ag which is shown in Fig. 7.3.2(a) and (b) respectively. Twinning partial dislocations in Fig. 7.3.2 are marked by arrowheads. The interface was rotated 36° from $(1\bar{1}\bar{1})_M$ to $(\bar{1}1\bar{1})_T$ consistent with the experimental observations. The number of twinning partial dislocations responsible for the twin are 14 and 15 in Ag and Cu, respectively, in Fig. 7.3.2(a). In Fig. 7.3.2(b) the numbers are 15 and 16 in Ag and Cu, respectively. These twinning partials were nucleated both at the cube-on-cube interfaces and at free surfaces with plane normal in x direction, to relieve the strain energy due to shearing.

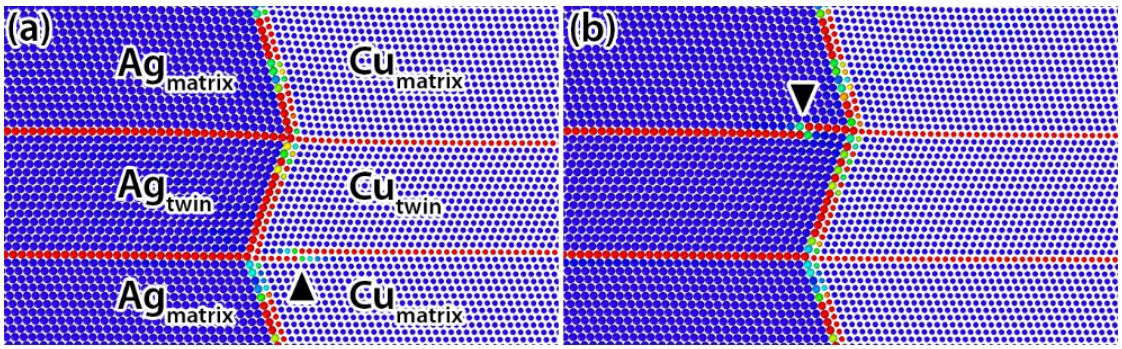

Figure 7.3.2 *MD simulation of layered AgCu structure with cube-on-cube interfaces showing twin thickening during straining. Thickening due to twinning partial dislocations that travels from Ag to Cu as well as from Cu to Ag, (a) and (b) respectively. Arrowheads mark twinning partial dislocations.*

Deformation twins were also observed to rotate the interfaces to a different plane, $(200)_T$. The bright-field electron micrograph presented in Fig. 7.3.3(a) shows the deformed microstructure from a sample with 250 nm bilayer thickness loaded *ex situ* to 4% strain at a strain rate of 10^3 s^{-1}. This shows a high density of deformation twins in Ag and Cu continuous across the cube-on-cube interface. However, it is noted that not all deformation twins in Ag generate one in Cu even if they impact the interface near locations that do. Examination of the boxed region in Fig. 7.3.3(a) at higher magnification, Fig. 7.3.3(b), shows that in regions where the twins appear continuous across the interface, the interface has rotated from $(1\bar{1}\bar{1})_M$ to $(200)_T$, determined from the diffraction pattern in Fig. 7.3.3(c). This rotation as well is consistent with dislocation theory and MD simulations for twinning partial dislocation transmission across a $(1\bar{1}\bar{1})_M$ interface and indicates the twinning partial dislocations responsible for the interfacial rotation have a Burgers vector of either $\frac{a}{6}[2\bar{1}1]$ or $\frac{a}{6}[\bar{1}\bar{1}\bar{2}]$ [6].

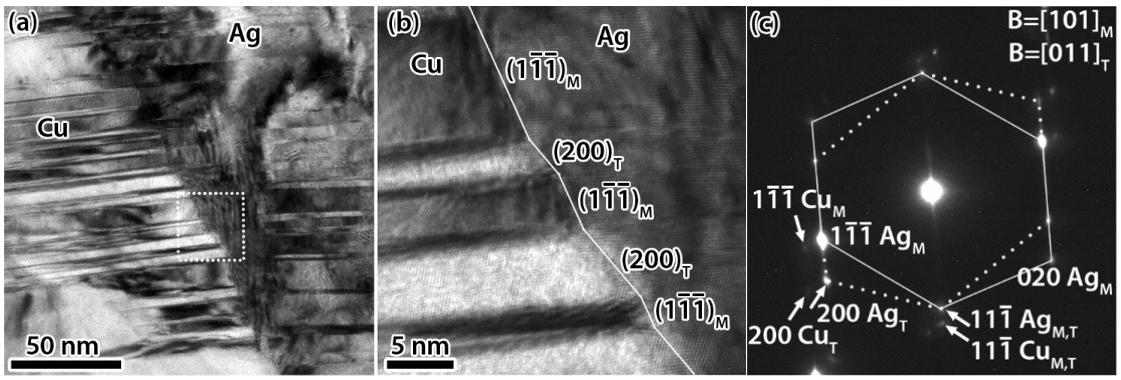

Figure 7.3.3 *(a) and (b) Bright-field TEM micrograph of water quenched material compressed to 4% strain by split-Hopkinson pressure bar. (b) is the region outlined by the white dotted lines in (a). (c) Corresponding selected area diffraction pattern. Subscripts M and T correspond to matrix and twin.*

Therefore, when the interface type is cube-on-cube, deformation twinning is observed continuous across the interfaces. Locations where the deformation twins are continuous across the interfaces are characterized by a rotation of $(1\bar{1}\bar{1})_M$ interface to either $(\bar{1}1\bar{1})_T$ or $(200)_T$. This was observed in both *in situ* and *ex situ* deformation experiments as well as in MD simulations.

7.3.2 Incoherent Twin Interfaces:

The two phases deform differently in regions exhibiting the incoherent twin orientation relationship between the Ag and Cu layers. In the 500 nm bi-layer thickness material loaded *ex situ* to 14.2% strain at a strain rate of 10^3 s^{-1}, deformation twinning was observed in the Ag-phase but it does not communicate across the incoherent twin interface into Cu, Fig. 7.3.4(a). As determined by the diffraction pattern in Fig. 7.3.4(b), deformation twins in Ag were only observed to form on the $(1\bar{1}\bar{1})_{Ag}$ plane which is the plane shared between Ag and Cu across the interfaces. The diffraction

pattern also shows spreading of the diffraction spots up to 10° from deformation induced rotations of the crystals. Subscripts T indicate twinning diffraction spots, which were only found for Ag.

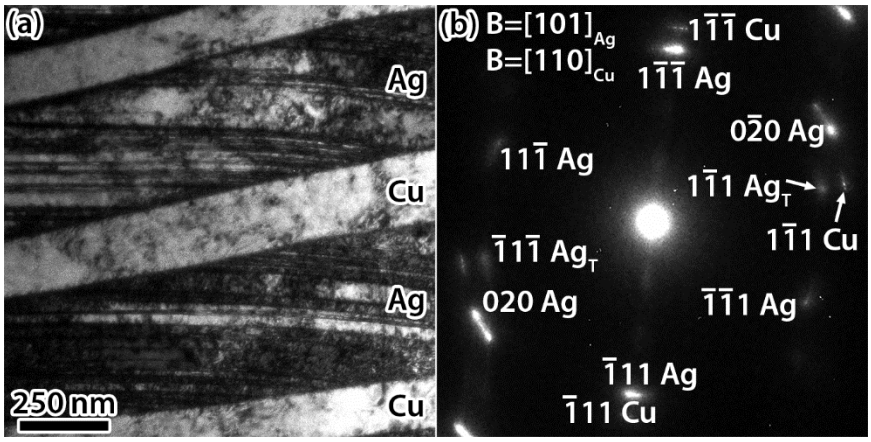

Figure 7.3.4 *(a) Bright-field electron micrograph of the deformation microstructure in a region of incoherent twin interfaces between Ag and Cu with 500 nm bi-layer thickness loaded 90° to the growth direction to 14.2%. (b) Selected area diffraction pattern of (a). Subscripts T indicate twin spots.*

Molecular dynamics simulations showed consistent deformation behavior with the experiments such that deformation twins were observed only in Ag, while deformation proceeded by dislocation slip in Cu which is highlighted in Fig. 7.3.5. In Fig. 7.3.5, partial dislocations are marked with arrowheads. In Fig. 7.3.5(a) it can be seen that a leading partial dislocation with Burgers vector $\frac{a}{6}[\bar{1}12]$ in Ag is trailed by a stacking fault. When the leading partial dislocation encounters the interface as shown in Fig. 7.3.5(b), the dislocation is blocked. Nucleation of another partial dislocation with a Burgers vector of $\frac{a}{6}[\bar{1}12]$ from the interface occurs on the next sequential plane back into Ag and creates a two layer stacking fault in Fig. 7.3.5(c). The second partial dislocation in Ag slips in the opposite direction as the first. Along with the nucleation of the second partial

dislocation was the nucleation of two perfect, extended, dislocations into Cu with Burgers vectors of $\frac{a}{6}[101]$ and $\frac{a}{6}[0\bar{1}1]$ on neighboring planes also observed in Fig. 7.3.5(c). The two layer stacking fault becomes a twin with the emission of a partial dislocation with a Burgers vector of $\frac{a}{6}[\bar{1}12]$ from the interface on the slip plane next to the two layer fault which is seen in Fig. 7.3.5(d). The rotation of the interface by the formation of the twin is 10° degrees and the interface structure is changed as shown in Fig. 7.3.6. In Fig. 7.3.6(a) the original interfacial structure is shown while the structure when the Ag has twinned by deformation is shown in (b). The original interface consists of $(1\bar{1}\bar{1})_{\mathrm{Ag}}$ and $(\bar{1}\bar{1}1)_{\mathrm{Cu}}$ for Ag while $(1\bar{1}\bar{1})_{\mathrm{Cu}}$ and $(002)_{\mathrm{Cu}}$. The section where the twin nucleated consist of the same type segments and steps of $(1\bar{1}\bar{1})_{\mathrm{Ag}}||(1\bar{1}\bar{1})_{\mathrm{Cu}}$ and $(002)_{\mathrm{Ag}}||(002)_{\mathrm{Cu}}$. By nucleating a twin into Ag, the local region of interface separating the two phases becomes a cube-on-cube interface. The change in interfacial structure certainly increases the interfacial energy, though by an unknown amount.

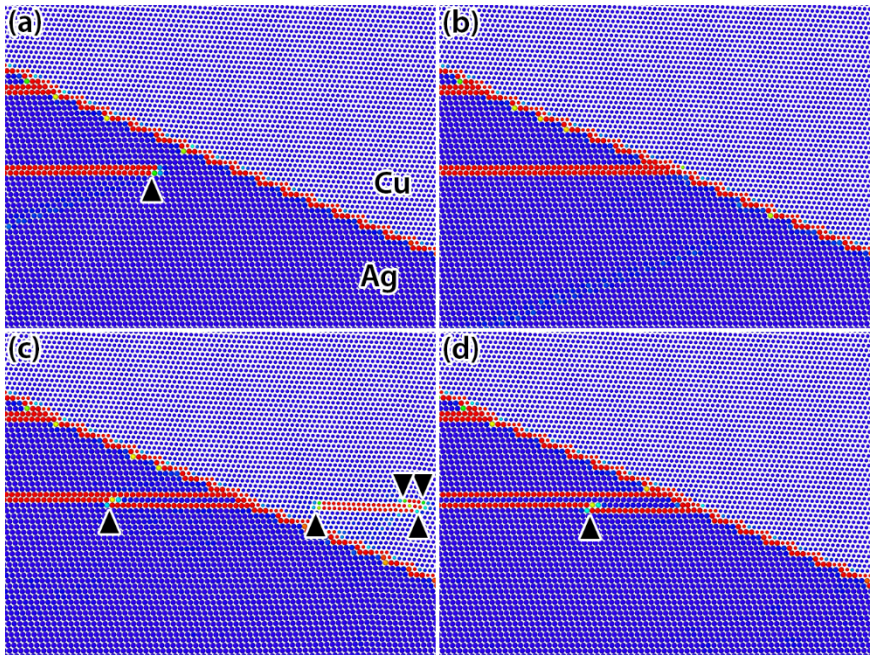

Figure 7.3.5 *MD simulation of layered AgCu with incoherent twin Ag/Cu interfaces during*

straining. Arrowheads mark partial dislocations.

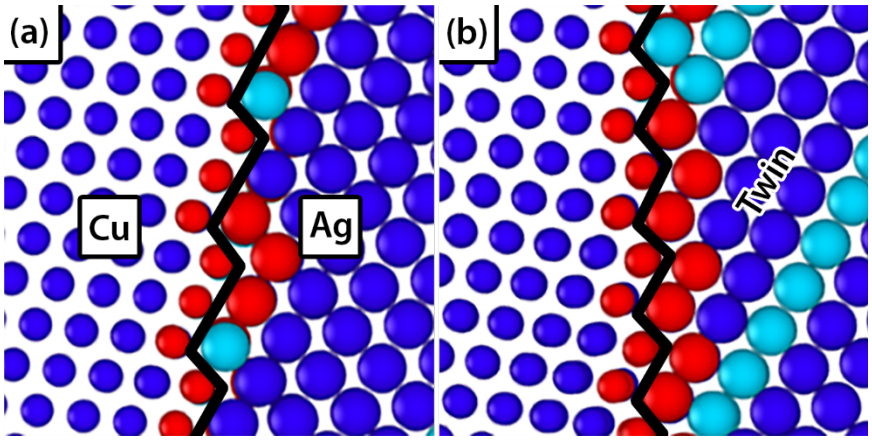

Figure 7.3.6 *MD simulated interfacial structure of Ag and Cu with (a) an incoherent twin interface, and (b) incoherent twin interface after twin nucleation into Ag which results in a region of cube-on-cube Ag/Cu interface.*

In situ TEM straining experiments help elucidate why deformation twinning is not occurring in Cu. Partial dislocations in Ag were observed to constrict before transferring across the interface as a perfect dislocation in Cu. An example of this is presented in Fig. 7.3.4. The stacking fault in Ag marked by the arrowheads in Figs. 7.3.4(a) and (c) resulted from the propagation of a leading partial dislocation across the Ag layer with a propagation direction of top right to bottom left. The leading partial dislocation is absorbed in the interface. Both the leading partial dislocation and the stacking fault are on the slip plane shared between Ag and Cu. Straining the sample more caused the trailing partial dislocation to emit and clear the stacking fault in Ag, and combine with the leading partial dislocation to form a perfect dislocation. Both events are observed in the difference image Fig. 7.3.4(c) which was created by overlaying the inverse of (a) onto (b). Perfect dislocation slip in Cu

was not directly observed but is evident from displacement of sample preparation ion damage, marked by the arrow in Fig. 7.3.4(c). The stacking fault in Ag and perfect dislocation in Cu were on the same plane which can be seen by where the stacking fault in Ag had been and the perfect dislocation in Cu had slipped in the difference image, Fig. 7.3.4(c). What has been highlighted is dislocation slip can directly cross incoherent twin interfaces on the shared plane for perfect dislocations but not partial dislocations.

Figure 7.3.7 *(a) and (b) Time resolved in situ straining of AgCu eutectic with 500 nm bi-layer thickness and incoherent twin interfaces and (c) difference image. Arrowheads mark stacking faults and the arrow marks displacement location of perfect dislocation slip in Cu. Interface in (c) is marked with the white dotted line.*

A MD simulation was performed to determine if the proposed mechanism for perfect dislocation transfer across the incoherent twin interfaces is reasonable. The simulation revealed that transmission was limited to perfect dislocations on the plane shared between Ag and Cu. Figure 7.3.5(a) shows a leading partial dislocation in Ag with a Burgers vector of $\frac{a}{6}[\bar{1}\bar{2}1]_{\mathrm{Ag}}$, marked by an arrowhead, propagating towards an incoherent twin interface on the shared plane, $(1\bar{1}\bar{1})_{\mathrm{Ag}}||(1\bar{1}\bar{1})_{\mathrm{Cu}}$, and trailed by a stacking fault and trailing partial dislocation with a Burgers vector of $\frac{a}{6}[1\bar{1}2]_{\mathrm{Ag}}$ also marked by an arrowhead. Upon encountering the interface, Fig. 7.3.5(b), the leading partial

dislocation is blocked. The trailing partial dislocation then combines with the leading partial dislocation to form a perfect dislocation in the interface, Fig. 7.3.5(c), before emitting as a perfect dislocation into Cu, marked by an arrowhead in Fig. 7.3.5(d), with a Burgers vector of $\frac{a}{2}[101]_{\mathrm{Cu}}$. The Burgers vector of the dislocation emitted in Cu is nearly the same, only slightly smaller from the difference in lattice parameters between Ag and Cu, than the original dislocation in Ag. The transmission shears the interface, changing its structure locally as shown in Fig. 7.3.5(d) marked with an arrow. Stress distributed in the interface is also present after transmission and resulted in the nucleation and emission of another perfect dislocation, extended dislocation, into Cu with a Burgers vector of $\frac{a}{2}[0\bar{1}1]_{\mathrm{Cu}}$ and a partial dislocation into Ag with a Burgers vector of $\frac{a}{6}[\bar{1}\bar{2}1]$, both marked with arrowheads in Fig. 7.3.5(e). It is not known whether the second perfect dislocation is due solely to relieving stress at the interface or nucleation as a result of the continued straining of the simulation. What the simulation shows is the interfaces are strong barriers to partial dislocations while perfect dislocations easily transfer directly.

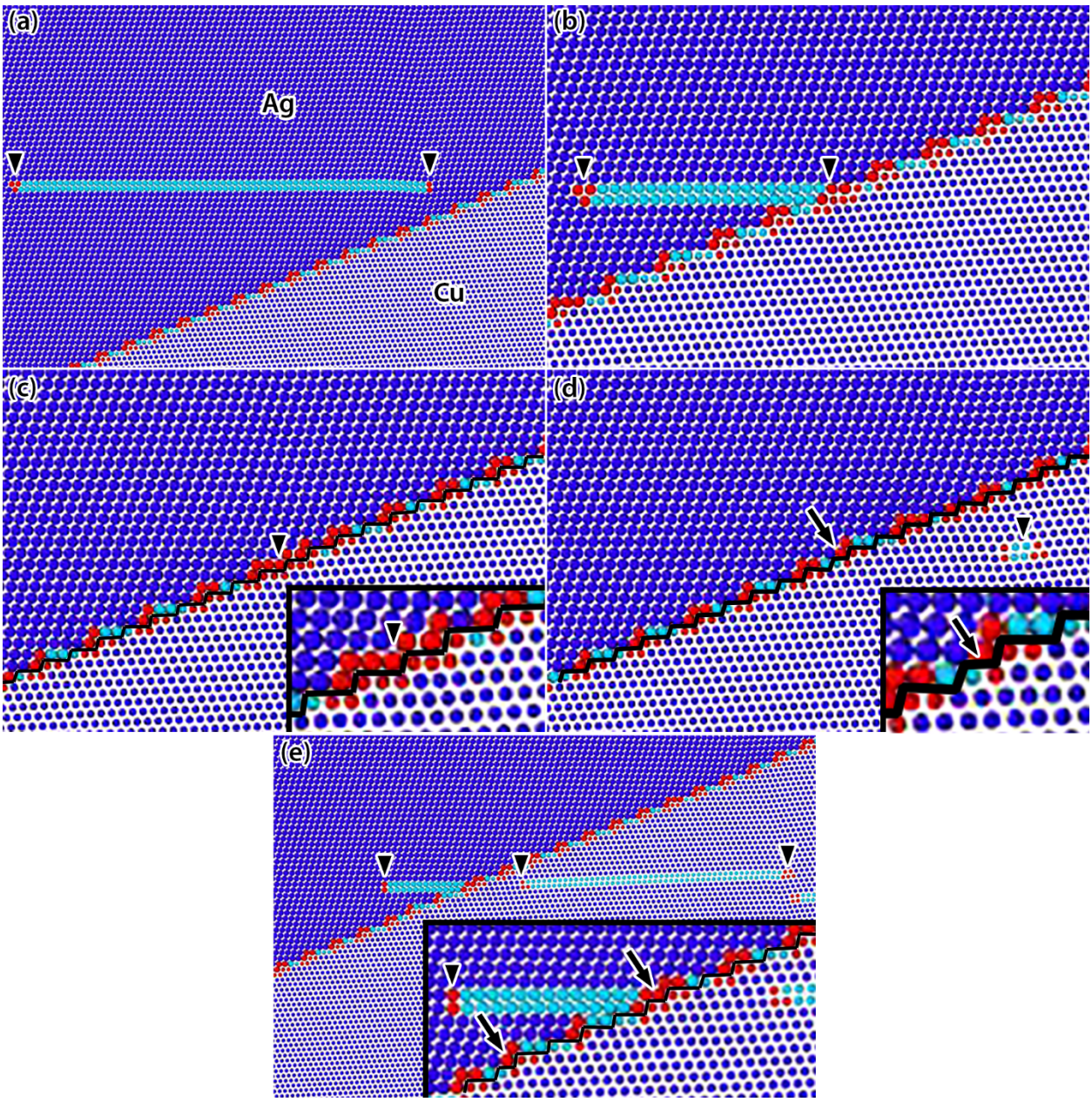

Figure 7.3.8 *MD simulation of an extended perfect dislocation with a Burgers vector of* $\frac{a}{2}[0\bar{1}1]_{Ag}$ *introduced in Ag and driven towards an incoherent twin Ag/Cu interface by an applied strain. Arrowheads mark partial dislocations in (a), (b) and (e). Arrowheads in (c) and (d) mark perfect dislocations. Arrows (d) mark disruptions in the interface structure. Black solid lines mark the interface between Ag and Cu.*

Perfect dislocations, as well as partial dislocations, encounter strong barriers at the incoherent twin interfaces when the dislocations are not on the shared slip plane, $(1\bar{1}\bar{1})_{\mathrm{Ag}}||(1\bar{1}\bar{1})_{\mathrm{Cu}}$. *In situ* TEM observations have shown reactions including cross-slip, absorption into the interface and back-emission into the Ag layer, and localized dislocation activity in the adjacent Cu layer. The first example shows an existing dislocation pile-up in Ag on one of the non-shared planes, Fig. 7.3.9, and shows the dislocation labeled "3" cross-slipping away from the dislocation pile-up. After the cross-slip event, the five dislocation pile-up against an incoherent twin interface between Ag and Cu in Fig. 7.3.9(a), becomes a four dislocation pile-up in Fig. 7.3.9(b). Difference image Fig. 7.3.9(c) was formed by overlaying the inverse of (a) onto (b) and shows the slip trace, which is on the $(1\bar{1}\bar{1})_{\mathrm{Ag}}$ plane, going away from the dislocation pile-up. The arrows in Fig. 7.3.9(b) and the difference image (c) mark the slip trace of the dislocation that cross-slipped. Slip was limited to the Ag layer as no evidence of dislocation activity in the top Cu layer was found despite the dislocation pile-up formed in Ag.

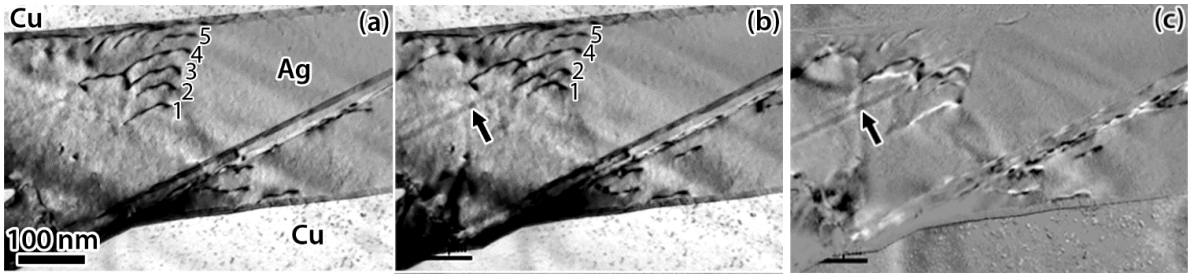

Figure 7.3.9 *(a) and (b) Time resolved images of AgCu eutectic with 500 nm bi-layer thickness and incoherent twin boundaries between Ag and Cu. Image (c) is a difference image. Arrows mark a slip trace.*

Emission of dislocations from the interface back into the Ag layer with the dislocation pile-up was also observed during the same straining experiment. In Fig. 7.3.10(b), emission of a partial dislocation from the interface is marked by an arrow. The emission occurred at a region of the interface that contained multiple dislocations. A short time later a second partial dislocation is emitted and they both extend into the Ag layer each trailing a stacking faults, Fig. 7.3.10(c). Contrast changes indicating dislocation emission into Cu were not observed throughout the straining indicating the plastic deformation was localized to the Ag layer. This experiment reveals that dislocations on the non-twin plane encounter a large barrier to communication across the interface and the resulting dislocation pile-ups do not generate sufficient stress for dislocation emission from the incoherent twin interface into the Cu layer.

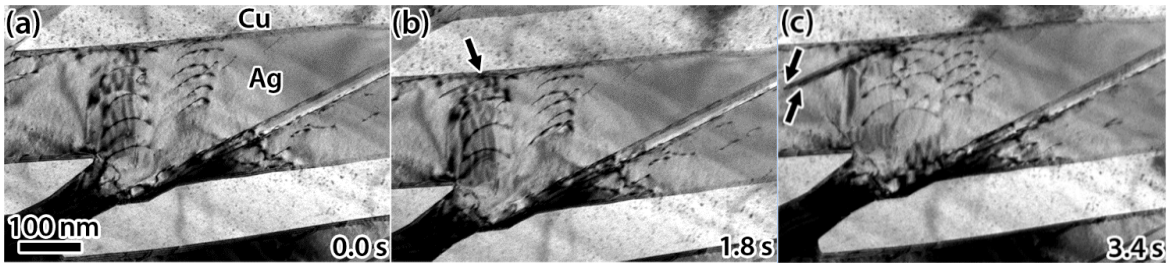

Figure 7.3.10 *(a), (b) and (c) Time resolved images of AgCu eutectic with 500 nm bi-layer thickness a incoherent twin interfaces between Ag and Cu. Arrows in (b) and (c) mark the back emission dislocations.*

When a source for dislocation pile-ups is not present, such as discontinuities of the lamellae, dislocations nucleate more uniformly along the incoherent twin interfaces in Ag. An example of this is shown in Fig. 7.3.11 with slip of both partial and perfect dislocations occurring on planes other than the shared slip plane. The $(\bar{1}\bar{1}1)_{\mathrm{Ag}}$ has active slip in addition to $(111)_{\mathrm{Ag}}$ and/or $(\bar{1}1\bar{1})_{\mathrm{Ag}}$ slip planes, see Fig. 7.3.12 for the arrangement of the slip planes. Dislocations in the Ag did not emit from a single location but instead at multiple locations along the interface, marked by arrowheads in

Fig. 7.3.11(a). The dislocations emitted in Ag_1 are predominantly partial dislocations which can be seen by the fringe contrast associated with the stacking faults trailing the dislocations. A few of the dislocations were, however, perfect dislocations. Though only the Ag is in contrast to properly observe dislocations, strain in Cu_1 is evident from the difference images and is marked by arrows in Figs. 7.3.11(d) and (e). Difference images Figs. 7.3.11(d) and (e) were formed by overlaying the inverse of (a) onto (b) and (c) respectively. Deformation is induced in the Ag_2 layer at the location of localized strain in the Cu layer, this is marked with an arrowhead in Figs. 7.3.11(e) and (f). If the strain was transferred plastically across Cu_1, dislocations in Cu_1 did not remain in the layer interiors, and were located in regions of high elastic strain which does not allow them to be observed or characterized experimentally. It is possible that elastic strain in Cu_1 was enough for emission of dislocations into Ag_2. In the course of the straining, deformation of the Ag layers is observed to occur to a greater extent than the Cu layers where deformation is more localized.

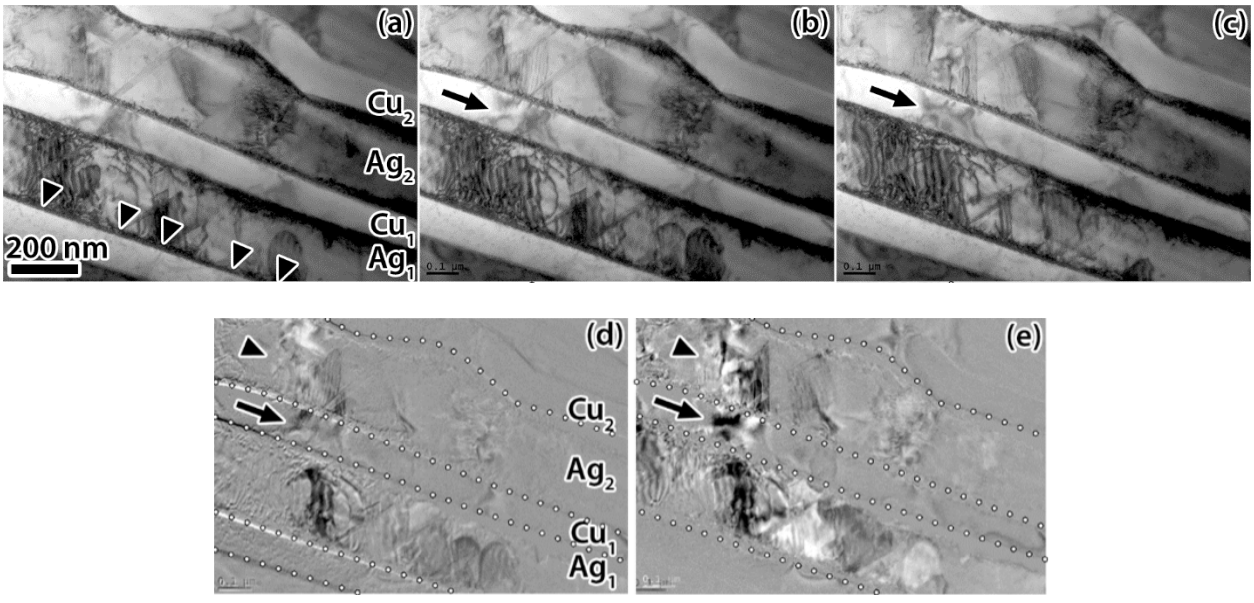

Figure 7.3.11 *(a), (b), and (c) Time resolved in situ straining of AgCu eutectic with 500 nm bi-layer thickness and incoherent twin interfaces between Ag and Cu, difference images (d) and (e). Arrowheads mark dislocation nucleation locations in Ag in (a). Arrows mark strain in Cu.*

Arrowheads in (d) and (e) mark strain in Ag. White dotted lines mark the interfaces in the difference images (d) and (e).

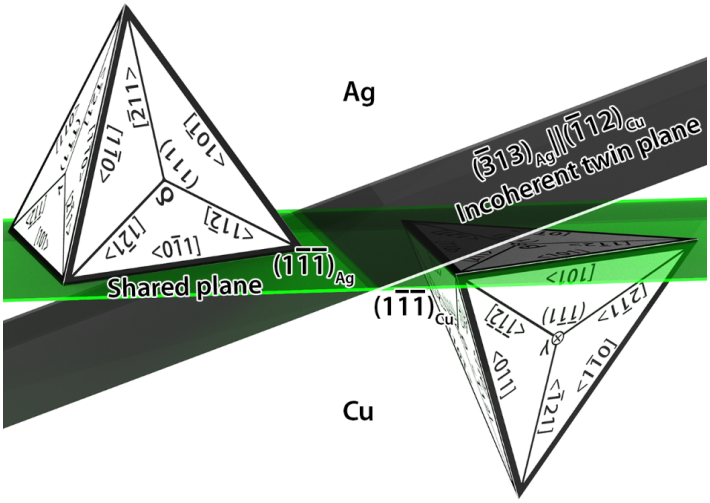

Figure 7.3.12 *Crystallographic alignment of Ag and Cu with incoherent twin interfaces as shown by the Thompson tetrahedra. The grey plane marks the interface. The green plane marks the twin plane.*

7.4 Discussion

Observations of dislocation interactions with the Ag/Cu interfaces were consistent with dislocation reactions across grain boundaries in single-phase FCC materials. The controlling factor is related to the magnitude of the Burgers vector of the residual dislocation generated in the grain boundary by the transmission event [15]. This controlling condition appears to be independent of dislocation type as well as grain boundary character in single phase materials [16]. The following discussion relates the experimental and simulation observations to the residual dislocation content left at the interfaces by the act of dislocation transmission through cube-on-cube and incoherent twin interfaces in a Ag/Cu eutectic alloy.

7.4.1 Cube-on-cube Interfaces

Previous studies conducted on AgCu eutectic compressed with SHPB revealed twinning in Cu in that system can be induced when the interfaces are cube-on-cube, at strains as low as 4 % and bilayer thicknesses ranging from 200 nm to 2200 nm [9, 17]. The deformation twins are continuous across the interfaces and cause an interfacial rotation. While twinning in the system was dependent on load orientation and bilayer thickness, when twinning occurred in Ag and was incident on the interfaces, twinning in Cu also occurred. That is to say, driving twinning in Cu was independent of layer thickness and load orientation. It had been proposed for AgCu alloys that deformation twinning in Ag is necessary to initiate deformation twinning in Cu [1]. This conclusion raises the important question about the interaction of twinning partial dislocations in Ag with the interface and causing deformation twinning in the Cu. One possible explanation is that the cube-on-cube interface is effectively transparent to the Ag twinning partial dislocations. This can be justified by the small residual dislocation left at the interface to transmit a twinning partial dislocation in Ag into Cu and vice versa, $|\mathrm{b}_{\mathrm{res}}| = \left|\frac{a}{6}\langle 112\rangle_{\mathrm{Ag}} - \frac{a}{6}\langle 112\rangle_{\mathrm{Cu}}\right| = 0.2$ Å. For the cube-on-cube interfaces the slip planes and slip directions between Ag and Cu are aligned which would mean the barriers to dislocations transmission would be coherency strains, image (Koehler) stresses, energy to create a step at the interface, and interactions with the interface misfit dislocations [4, 5, 18].

MD simulations of a $\{111\}_{\mathrm{Ag}}||\{111\}_{\mathrm{Cu}}$ interface with a cube-on-cube orientation relationship supports the mechanism of direct transfer of twinning partial dislocation across the interface [6]. In the simulations, two sets of twinning partial dislocations were considered to be able to form the twin in Ag and will be discussed here analogously but with crystallographic directions that are the same as in Figs. 7.3.1 and 7.3.2 of the results presented here. Partial dislocations on the $(\bar{1}\bar{1}1)$ slip plane with a Burgers vector of $\mathrm{b}_{\mathrm{Ag}} = \frac{a}{6}[\bar{1}21]$ or an equal combination of partial dislocations with Burgers vectors of $\mathrm{b}_{\mathrm{Ag}} = \frac{a}{6}[2\bar{1}1]$ and $\mathrm{b}_{\mathrm{Ag}} = \frac{a}{6}[\bar{1}\bar{1}\bar{2}]$. Interaction of either set of the partial dislocations

would result in the formation of intrinsic interfacial dislocations and two different rotations of the interface plane. The first set of partial dislocations, $b_{Ag} = \frac{a}{6}[\bar{1}21]$, will leave a residual dislocation with a Burgers vector of magnitude, $|b_{res}|$ = 0.20 Å for each partial dislocation transmitted, due to the difference in lattice parameters of Ag and Cu, and will rotate the interface from $(1\bar{1}\bar{1})_M$ to $(\bar{1}1\bar{1})_T$ where subscripts M and T denote matrix and twin. The second set, alternating partial dislocations with Burgers vectors of $b_{Ag} = \frac{a}{6}[2\bar{1}1]$ and $b_{Ag} = \frac{a}{6}[\bar{1}\bar{1}\bar{2}]$, would leave a residual dislocation with a Burgers vector of magnitude 0.20 Å for each pair of partial dislocations, that is two dislocations, and a rotation of the interface from $(1\bar{1}\bar{1})_M$ to $(200)_T$. Both types of rotations were observed experimentally and shown in Figs. 7.3.1 and 7.3.2.

Wang *et al*. proposed that the rotation of the interface to $(200)_T$ is more favorable because reactions involving a set of Ag twinning partial dislocations with different Burgers vectors transmit more easily than twinning partial dislocations of a single type [6]. This is from the smaller magnitude of the residual dislocations left at the interface [6]. For example, if one of $\frac{a}{6}[2\bar{1}1]$ and $\frac{a}{6}[\bar{1}\bar{1}\bar{2}]$ partial dislocations on the $(\bar{1}\bar{1}1)$ twin plane slip on neighboring planes, the combined Burgers vector for the two twinning partial dislocations is $\frac{a}{6}[2\bar{1}1] + \frac{a}{6}[\bar{1}\bar{1}\bar{2}] = \frac{a}{6}[1\bar{2}\bar{1}]$which is the same magnitude of one partial dislocation, transmitting the two will result in a $|b_{res}|$ of 0.20 Å by a transmission event. The study assumed an equal combination of two different partial dislocations and not one or the other. If the twining partial dislocations were exclusively one or the other the residual Burgers vector would be the same as the first case, which is 0.20 Å for each twinning partial dislocation. The study did not account for interfacial energy of the rotated region of interface, $\{111\}_{Ag}||\{111\}_{Cu}$ has an interfacial energy of 247 mJ/m^2 compared to $\{200\}_{Ag}||\{200\}_{Cu}$ with an energy of 395 mJ/m^2 [19], rotating to a higher interface energy would have an associated energy cost. Both interface rotations were observed in experimental results presented here. In the observations

made in this work the larger rotation was observed more frequently. Additionally, Wang *et al.* suggested that the total energy of the accumulated intrinsic interfacial dislocations could be reduced by the interface ejecting other dislocations in addition to the Cu twinning partial dislocations [6]. Such a response from an interface occurred during multiple *in situ* TEM straining experiments but not in relation to the transfer of twinning partial dislocations across the interface. It would appear that the process of deformation twin transfer across a cube-on-cube interface is controlled by, minimization of the accumulation of intrinsic interfacial dislocations, and not the preference of deformation mode for Cu which would otherwise not twin [6]. It also was found experimentally, see Fig. 7.3.1, that the deformation twins were transmitted from the Cu back into the Ag through a cube-on-cube interface. The rotation of the interface was of equal magnitude and direction as caused by the transfer of a twin from Ag to Cu. The independence of the rotation on the direction of twin transfer, Ag to Cu or Cu to Ag, can be accounted for by geometric arguments. However, blockage of the Ag deformation twins was common in the SHPB experiments [17]. Molecular dynamics of cube-on-cube interfaces, not shown, suggest that the periodic stress in the interface hinder the communication across it. The role of these stresses remains to be verified. However, in a cube-on-cube interface high stress locations are spaced every 18.76 Å, the same spacing as misfit dislocations. The interplanar spacing of {111} planes in Ag is 2.36 Å. Therefore, even a deformation twin of just eight layers would encounter this periodic stress.

7.4.2 Incoherent Twin Interfaces

Geometrically, incoherent twin interfaces are more complicated than the cube-on-cube interfaces. The barrier strength of incoherent twin boundaries to slip transmission is attributed to geometric factors of the boundary. The incoherent twin boundary can either be a strong or weak barrier to dislocations. A path for dislocations to encounter a weak barrier is for perfect dislocations on the plane, continuous across the interface. The interface geometry is visualized in Fig. 7.3.12 where the

incoherent twin plane between Ag and Cu is the grey plane, and the shared slip plane is the green plane. In this Figure, the Thompson tetrahedra are included for the Ag and Cu layers and are oriented with respect to each other to take into account the twin orientation relationship. To convert the Ag coordinates into the Cu coordinate system such that $[\mathrm{V}]_{\mathrm{Ag}} \cdot \mathrm{R} = [\mathrm{V}]_{\mathrm{Cu}}$ where $[\mathrm{V}]_{\mathrm{Ag}}$ is a one by three matrix of the desired vector to be transformed, the following rotation matrix, R, is used.

$$\mathrm{R} = \begin{bmatrix} 2/3 & 1/3 & -2/3 \\ -2/3 & 2/3 & -1/3 \\ 1/3 & 2/3 & 2/3 \end{bmatrix}$$

Perfect dislocations on the shared plane, $(1\bar{1}\bar{1})$, in the Ag and the Cu are well-aligned with each other and will leave minimal residual dislocation content at the interface if transmitted directly across. The three reactions of perfect dislocations on the shared plane are listed as the first three reactions in Table 7.4.1 along with the angle between the normal of the incoming and outgoing slip planes, the magnitude of Burgers vector of the residual dislocation left at the interface, and m'. The geometric criteria is defined by $\mathrm{m}' = \cos(\phi) \cdot \cos(\kappa)$ where ϕ is the angle between the slip plane normals and κ is the angle between Burgers vectors of the incoming and outgoing slip systems. After taking into account the 2° misorientation about the $[101]_{\mathrm{Ag}}$ and the difference in lattice parameters between Ag and Cu, the $|\mathrm{b}_{\mathrm{res}}|$ left for those reactions is 0.35 Å. The $|\mathrm{b}_{\mathrm{res}}|$ component due to the difference in lattice parameter only is 0.34 Å. The component due to the 2° misorientation is ignored through the rest of the analysis as it is small. From *in situ* TEM straining experiments and MD simulation, it was found that perfect dislocations on the twin plane absorb into the Ag/Cu interface and emit into the next lamellae on the same plane (the shared plane), for example in Figs. 7.3.7 and 7.3.8. All of the slip transfer criteria proposed previously for dislocation interactions with grain boundaries including the Livingston and Chalmers criterion, two different geometric criteria, and the LRB criteria rationalize this observation [20-23].

When considering partial dislocations, on the shared plane there is a deviation between the geometric criteria m' and the magnitude of the residual dislocation Burgers vector left at the interface due to the dislocation reaction as seen in the last three reactions of Table 7.4.1. The Burgers vectors of the three different leading partial dislocation on the twin plane in Ag are opposite in direction to the three in Cu when the Ag and Cu have a twin orientation relationship. As a result, the generation of a perfect or a partial dislocation in Cu due to the interaction of a partial dislocation in Ag interacting with an incoherent twin interface produces a Burgers vector with a minimum magnitude of 1.39 Å and 1.30 Å, respectively. No cases of partial dislocations on the twin plane impinging on the incoherent twin interfaces were observed to generate slip in the next lamellae in the *in situ* straining experiments, which is probably due to the large magnitude of the Burgers vector of the residual dislocation that would be required to be left at the interface. As a result, only perfect dislocations on the common plane are observed to transmit across the incoherent twin interfaces. Of the reactions provided in Table 7.4.1, the geometric criterion m' corresponds well to the minimization of $|b_{res}|$ for the first three cases, however, the last case results in an incorrect prediction. The discrepancy is due to the geometric criterion not differentiating perfect from partial dislocations. It is also unnecessary to combine the angle between the slip plane normals with the angles between the Burgers vectors, as the partial dislocations on the common plane do not transmit across the interfaces despite alignment of a slip plane across the interface. Alignment of the slip plane traces as is included in the LRB criteria is also unnecessary according to the last case in Table 7.4.1. The use of the geometric criteria, m', has been used to explain deformation mechanisms in metallic multilayer composites such as the Cu-Nb system. It has also been proposed that it should be modified such that the angle between the incoming and outgoing Burgers vectors or slip planes is not too large which allows the two components to be considered separately before being coupled. Even with the modification, the geometric criteria does not differentiate between perfect and partial

dislocation Burgers vector magnitudes and is not as well suited as $|b_{res}|$ for predicting dislocation reactions with interfaces.

Table 7.4.1 *Dislocation reactions from Ag into Cu and corresponding angle between the slip plane normals, $|b_{res}|$, and m' (geometric criterion) value. Interface type is incoherent twin.*

Dislocation reaction at interface	Angle between slip plane normals	Magnitude of Burgers vector of the residual dislocation left at the interface (Å)	m' (geometric criterion)
$\frac{a}{2}[0\bar{1}1](1\bar{1}\bar{1})_{Ag} \rightarrow \frac{a}{2}[101](1\bar{1}\bar{1})_{Cu}$	0.0	0.34	1.00
$\frac{a}{2}[101](1\bar{1}\bar{1})_{Ag} \rightarrow \frac{a}{2}[110](1\bar{1}\bar{1})_{Cu}$	0.0	0.34	1.00
$\frac{a}{2}[110](1\bar{1}\bar{1})_{Ag} \rightarrow \frac{a}{2}[01\bar{1}](1\bar{1}\bar{1})_{Cu}$	0.0	0.34	1.00
$\frac{a}{6}[12\bar{1}](1\bar{1}\bar{1})_{Ag} \rightarrow \frac{a}{6}[12\bar{1}](1\bar{1}\bar{1})_{Cu}$	0.0	1.58	0.50
$\frac{a}{6}[12\bar{1}](1\bar{1}\bar{1})_{Ag} \rightarrow \frac{a}{6}[11\bar{2}](111)_{Cu}$	70.5	1.30	0.22
$\frac{a}{6}[12\bar{1}](1\bar{1}\bar{1})_{Ag} \rightarrow \frac{a}{2}[\bar{1}0\bar{1}](1\bar{1}\bar{1})_{Cu}$	0.0	1.39	0.87

In summary, minimization of the residual Burgers vector at the interface corresponded well to predicting if strain transfers across an interface. When the reaction results in a small $|b_{res}| \leq 0.34$ Å, strain was observed to transfer across the interface even driving twinning in Cu when it otherwise would deform by dislocation slip only. With larger $|b_{res}|$, dislocation slip was effectively blocked by the interface.

7.5 Conclusions

Deformation twinning in Cu, in the AgCu eutectic, has been found at Cu layer thicknesses between 50 nm and several microns, and strains as low as 4% for bulk samples strained in compression at 10^3 s^{-1}. The determining factor to driving twinning in Cu is a source of twinning partial dislocations provided by Ag that are able to transmit across the Ag/Cu interfaces. This requires i) twinning partial dislocations in Ag and ii) cube-on-cube Ag/Cu interfaces. Transmission of twinning partial dislocations across the Ag/Cu interfaces proposed by Wang *et al.* was confirmed including the rotation of the interface by the event [6].

The mechanism of twinning in the Cu-phase is directly related to how dislocations interact with the Ag/Cu interfaces. For dislocations interacting with the different Ag/Cu interface types, the residual dislocation left at the interface had to be small for communication across the interface. This criterion was found to be determining to the point where deformation twinning could be driven in Cu under conditions it otherwise would not. With larger $|b_{res}|$, dislocation slip was effectively blocked by the interface. For example, partial dislocations in Ag on the common plane are blocked by the incoherent twin interfaces because to communicate across would require a $|b_{res}|$ = 1.30 Å, while perfect dislocations in Ag on the common plane communicate across with a $|b_{res}|$ = 0.34 Å. Even though both the partial and the perfect dislocations are on the slip plane that is continuous across the interface.

Reference

1. Beyerlein, I.J., et al., *Texture evolution via combined slip and deformation twinning in rolled silver-copper cast eutectic nanocomposite.* International Journal of Plasticity, 2011. **27**(1): p. 121-146.

2. Tian, Y.Z. and Z.F. Zhang, *Stability of interfaces in a multilayered Ag-Cu composite during cold rolling.* Scripta Materialia, 2013. **68**(7): p. 542-545.

3. Kingstedt, O.T., et al., *Quasi-static and dynamic compressive deformation of a bulk nanolayered Ag-Cu eutectic alloy: Macroscopic response and dominant deformation mechanisms.* Materials Science and Engineering a-Structural Materials Properties Microstructure and Processing, 2014. **595**: p. 54-63.

4. Hoagland, R.G., R.J. Kurtz, and C.H. Henager, *Slip resistance of interfaces and the strength of metallic multilayer composites.* Scripta Materialia, 2004. **50**(6): p. 775-779.

5. Cline, H.E. and D.F. Stein, *Strengthening by Interfaces in Ag-Cu Directionally Solidified Eutectic.* Transactions of the Metallurgical Society of AIME, 1969. **245**(4): p. 841-&.

6. Wang, J., et al., *Interface-facilitated deformation twinning in copper within submicron Ag-Cu multilayered composites.* Scripta Materialia, 2011. **64**(12): p. 1083-1086.

7. Shen, T.D., R.B. Schwarz, and X. Zhang, *Bulk nanostructured alloys prepared by flux melting and melt solidification.* Applied Physics Letters, 2005. **87**(14).

8. Eftink, B.P., et al., *Deformation response of cube-on-cube and incoherent twin interfaces in AgCu eutectic after dynamic loading.* In Preparation, 2016.

9. Kingstedt, O.T., et al., *Quasi-static and dynamic compressive deformation of a bulk nanolayered Ag–Cu eutectic alloy: Macroscopic response and dominant deformation mechanisms.* Materials Science and Engineering: A, 2014. **595**(0): p. 54-63.

10. Field, R.D., *Location specific in situ TEM straining specimens made using FIB.* Ultramicroscopy, 2004. **102**(1): p. 23-26.

11. Plimpton, S., *Fast parallel algorithms for short-range molecular dynamics.* Journal of Computational Physics, 1995. **117**(1): p. 1-19.

12. Williams, P.L., Y. Mishin, and J.C. Hamilton, *An embedded-atom potential for the Cu-Ag system.* Modelling and Simulation in Materials Science and Engineering, 2006. **14**(5): p. 817-833.

13. Stukowski, A., *Visualization and analysis of atomistic simulation data with OVITO-the Open Visualization Tool.* Modelling and Simulation in Materials Science and Engineering, 2010. **18**(1): p. 1-7.

14. Eftink, B.P., et al., *Interface mediated mechanisms of plastic strain recovery in a AgCu alloy.* Submitted, 2016.

15. Kacher, J., et al., *Dislocation interactions with grain boundary interactions.* Current Opinion in Solid State and Materials Science, 2014. **18** p. 227-243.

16. Kacher, J. and I.M. Robertson, *Quasi-four-dimensional analysis of dislocation interactions with grain boundaries in 304 stainless steel.* Acta Materialia, 2012. **60**(19): p. 6657-6672.

17. Eftink, B.P., et al., *Anomalous deformation twinning in coarse-grained Cu in Ag60Cu40 composites under high strain-rate compressive loading.* Materials Science and Engineering: A, 2014. **618**(0): p. 254-261.

18. Henager, C.H., R.J. Kurtz, and R.G. Hoagland, *Interactions of dislocations with disconnections in fcc metallic nanolayered materials.* Philosophical Magazine, 2004. **84**(22): p. 2277-2303.

19. Shao, S., Unpublished results, 2014.

20. Livingston, J.D. and B. Chalmers, *Multiple slip in bicrystal deformation.* Acta Metallurgica, 1957. **5**(6): p. 322-327.

21. Shen, Z., R.H. Wagoner, and W.A.T. Clark, *Dislocation and Grain-Boundary Interactions in Metals.* Acta Metallurgica, 1988. **36**(12): p. 3231-3242.

22. Morris, M.A. and J. Luster, *Effect of rotation relationship between gamma grains on compatability of deformation in Ti-Al alloys*, in *High-Temperature Ordered Intermetallic Alloys Vi, Pts 1 and 2*, J. Horton, et al., Editors. 1995, Materials Research Soc: Pittsburgh. p. 593-598.

23. Luster, J. and M.A. Morris, *Compatibility of deformation in two-phase Ti-Al alloys: Dependence on microstructure and orientation relationships.* Metallurgical and Materials Transactions A, 1995. **26**(7): p. 1745-1756.

Chapter 8 Future Directions

The thesis discusses how interfaces influence the surface mechanical properties such as friction and wear, and bulk mechanical properties such as flow stress. Three material systems were chosen for the studies, including silica, nanocrystalline (nc) Cu or Cu/Ag alloys, and Cu or Cu/Ag multilayered structures. The chemistry, energetics, structures, compositions and densities of the interfaces have been varied and their effects on the mechanical properties have been determined.

There are still many interesting areas that one may want to explore. For instance, based on the identified basic wear mechanisms at silica/silica interfaces, it is possible for us to estimate the activation barriers of unit wear processes and predict the wear volume using the thermal activation formula. One may also want to prepare Cu/Ag alloys with different morphologies, such as nc Cu/Ag structures with both Cu and Ag grains, or nc Cu/Ag structures with intragranular Ag precipitates. These morphologies are also observed in experimental samples when different sample-preparation methods are used. It will be interesting to know which morphology of Cu/Ag alloys demonstrates the best mechanical properties. It is also interesting to study the friction and wear on a substrate of Cu/Ag alloys with nc structures and multilayered structures. For instance, we can use different morphologies and concentrations of Cu/Ag alloys for friction and wear tests. We can also change the orientations between the Cu/Ag multilayered interfaces and frictional sliding. These studies will bring new insights to the design of metallic systems with superior friction and wear properties.